Die approbierte Originalversion dieser Dissertation ist in der Hauptbibliothek der Technischen Universität Wien aufgestellt und zugänglich.
http://www.ub.tuwien.ac.at

The approved original version of this thesis is available at the main library of the Vienna University of Technology.
http://www.ub.tuwien.ac.at/eng

TECHNISCHE
UNIVERSITÄT
WIEN
Vienna University of Technology

MEDIZINISCHE
UNIVERSITÄT
WIEN

DISSERTATION

Assessment of retinal perfusion in the rat via Fourier-Domain Optical Coherence Tomography

ausgeführt zum Zwecke der Erlangung des akademischen Grades eines
Doktors der technischen Wissenschaften
unter der Leitung von

Ao.Univ.-Prof. DI Dr. Martin Gröschl
E134 Institut für Angewandte Physik
Technische Universität Wien

und

Ao.Univ.-Prof. DI Dr. Leopold Schmetterer
Assoc.-Prof. DI(FH) René Werkmeister, PhD
Zentrum für med. Physik und biomed. Technik
Medizinische Universität Wien

eingereicht an der
Technischen Universität Wien
Fakultät für Physik

von

Dipl.-Ing. Martin Vietauer
e0425305
Beckmanngasse 32-34/2/13
A-1140 Wien

Wien, im September 2016

Abstract

Optical coherence tomography (OCT) is an interferometric non-invasive imaging technique that is capable of creating cross-sectional images of biological tissues. The resolution of those cross-sectional images is in the micrometer range.

Doppler OCT is an extension of the post-processing method used for regular OCT and allows the determination of the sample particles' velocities via the Doppler effect.

In this work, a measurement system for the determination of relative changes in the blood flow of large retinal vessels in rat eyes was developed. The system consists of a single beam Fourier-domain OCT (FDOCT) setup, capable of measuring blood flow velocities in large retinal vessels, and a commercially available dynamic vessel analyzer for rodents, which allows high precision measurements of retinal vessel diameters. Both systems are coupled, so that blood flow velocities and vessel diameters of retinal vessels can be detected simultaneously. Furthermore, a method to detect changes in the retinal microcirculation using the same measurement system was developed and tested.

The newly developed measurement system as well as the novel method for the assessment of the retinal microcirculation in rat eyes were both evaluated using in vitro tests before any in vivo experiments in test animals were conducted. Thereafter, oxygen breathing and flicker light induced blood flow changes were measured in large retinal vessels in the rat eye. The results of these experiments are in the range of the values presented in earlier human studies. Furthermore, the findings of the subsequent microcirculation hyperoxia experiments in this thesis are in excellent agreement with the hyperoxia data of large retinal vessel experiments.

The promising results of the presented measurement system and microcirculation assessment method show a high potential for the study of ocular diseases and their underlying mechanisms in animal models. Such studies may contribute to the further understanding of ocular diseases and thus help to develop possible treatment methods.

Kurzfassung

Optische Kohärenztomographie (OCT) ist ein nichtinvasives interferometrisches bildgebendes Verfahren, welches in der Lage ist, Querschnittbilder von biologischem Gewebe zu erstellen. Die Auflösung dieser Querschnittbilder bewegt sich im Mikrometerbereich. Eine Erweiterung der üblichen Datenauswertungsroutine von OCT Systemen ermöglicht es, die Geschwindigkeiten der untersuchten Probenteilchen basierend auf dem Dopplereffekt zu bestimmen; diese Erweiterung wird Doppler OCT genannt.

Im Rahmen der vorliegenden Arbeit wurde ein Messsystem zum Zwecke der Bestimmung von relativen Änderungen des Blutflusses in großen Netzhautgefäßen in Rattenaugen entwickelt. Das System besteht aus einem in der Fourier-Domäne arbeitenden einstrahligen OCT Aufbau, der in der Lage ist, die Blutflussgeschwindigkeiten in großen Netzhautgefäßen zu messen und einem kommerziell erhältlichen Gerät zur hochpräzisen Bestimmung von retinalen Gefäßdurchmessern in Rattenaugen. Beide Systeme sind miteinander gekoppelt, um die gleichzeitige Messung von Blutflussgeschwindigkeiten und Gefäßdurchmessern von Netzhautgefäßen zu ermöglichen. Weiters wurde unter Benutzung desselben Messsystems eine Methode zur Bestimmung von Änderungen in der retinalen Mikrozirkulation entwickelt und getestet.

Sowohl das entwickelte Messgerät als auch die neue Messmethode zur Erfassung von Änderungen in der retinalen Mikrozirkulation in Rattenaugen wurden durch in vitro Experimente getestet, bevor die ersten in vivo Versuche durchgeführt wurden. Anschließend wurden Blutflussänderungen in großen Netzhautgefäßen, bedingt durch das Einatmen von reinem Sauerstoff, sowie durch Lichtstimulation mittels eines Stroboskops im Rattenauge gemessen. Die gemessenen Gefäßdurchmesser- und Blutflussgeschwindigkeitsdaten bewegen sich in derselben Größenordnung wie in bereits publizierten Humanstudien. Weiters stimmen die Resultate der anschließend durchgeführten Hyperoxie Experimente in der Mikrozirkulation sehr gut mit den an großen Netzhautgefäßen ermittelten Hyperoxie Daten überein.

Die Ergebnisse der Messungen mit dem vorgestellten Messsystem und der Methode zur Erfassung der Mikrozirkulation sind vielversprechend und zeigen, dass beide Entwicklungen in hohem Maße geeignet erscheinen, diverse Augenkrankheiten und deren zugrundeliegende Mechanismen in Tiermodellen zu untersuchen. Solche Untersuchungen können in Zukunft dazu beitragen, Augenkrankheiten besser zu verstehen und dabei helfen, mögliche medizinische Behandlungsstrategien zu entwickeln.

Acknowledgments

I would like to express my greatest thanks to my supervisor Martin Gröschl, who introduced me into the research group of Leopold Schmetterer at the Center of Medical Physics and Biomedical Engineering, and thus made this thesis possible in the first place. He always supported me and my colleagues and helped us with his knowledge in scientific as well as organizational matters.

My honest gratitude goes to my second supervisor Leopold Schmetterer for offering me a position in his research group and for constantly sharing his scientific expertise and honest opinion on the progress of my projects.

I owe my deepest gratitude to my supervising colleague René Werkmeister, who was a constant source of knowledge and expertise; whenever there was a seemingly unsolvable problem, he was there to help. In spite of his own immense workload, he always took the time to explain things to us PhDs and to answer our questions.

I would like to offer my special thanks to my coworker Corinna Knopf for helping me conducting all my experiments and for preparing all the test animals. Without her, the experiments and thus the thesis at hand would not have been possible. Besides, she was always there to discuss problems and find possible solutions and last but not least, Corinna helped to evaluate a considerable part of the huge amount of measurement data, which was a lengthy and sometimes frustrating work.

I also wish to thank Robert Klaus for sharing the solitude of the AKH animal lab, assisting during difficult measurements, listening to my complaints about the slow progress of my thesis and for cheering me up with his “slightly” sarcastic comments.

I am particularly grateful for the assistance given by all the staff from the AKH animal lab; they were great colleagues and helped us whenever we encountered problems during our measurements.

I would like to express my sincere gratitude to Veronika Doblhoff-Dier, who gladly shared her knowledge in programming and of OCT setups. She was always ready to discuss physical problems and to help solving them. Furthermore, I am very grateful to Veronika for proofreading my whole thesis, which surely was a great deal of work. Thank you, Veronika, for being such a great person!

My thanks also go to my fellow PhDs Gerold Aschinger and Valentin Aranha dos Santos, who were always ready for fruitful scientific discussions and who gladly shared their knowledge and ideas.

At the Center of Medical Physics and Biomedical Engineering, I had the honor of working together with many great people and I want to thank them all; especially the scientists Bernhard Baumann, Michael Pircher, Rainer Leitgeb, Richard Haindl, Daniel Fechtig, Wolfgang Trasischker, Michael Bronhagl, Iris Schmidt, Jozsef Klaizer, Alina Messner, Thomas Blaschke; and especially the CMPBMT staff members Harald Sattmann, Andreas Hodul, Siegfried Gollubits, Bernhard Rosenauer, Angela Taubeck and Peter Stadlmaier.

Furthermore, I would like to thank my friends, who often helped me to remember that work is not everything in life and that life without fun is no life at all!

My special thanks go to my family, especially to my parents Renate and Reinhold Vietauer, as well as to my sisters Eva and Anita for supporting me always and in any possible way. Thank you! I am lucky to have such a great family!

Finally, I want to thank Ulrike Steiner for constantly supporting me during the whole thesis, even in times when I was completely demotivated and had no hope of ever finishing this work. Somehow she always found ways to help me. Whenever I was displeased with the progress of my thesis, Ulrike told me how much I have already had accomplished and that I should rather be proud of myself. I cannot thank you enough for your support and for just being at my side. Thank you!

Contents

List of figures 9

List of abbreviations 11

1 Introduction 14

2 Medical aspects 16
- 2.1 Anatomy of the rat eye 16
- 2.2 Retinal perfusion 18
- 2.3 Differences between rat eye and human eye 19
- 2.4 Ocular Diseases 20
  - 2.4.1 Age-related macula degeneration 20
  - 2.4.2 Diabetic retinopathy 21
  - 2.4.3 Glaucoma 21
  - 2.4.4 Venous obstructive disease of the retina 22
- 2.5 Techniques for measuring retinal blood flow 22
  - 2.5.1 Color Doppler imaging 22
  - 2.5.2 Angiography 23
  - 2.5.3 The blue field entoptic technique 23
  - 2.5.4 Laser Doppler velocimetry 24
  - 2.5.5 Laser speckle technique 24
  - 2.5.6 Retinal vessel diameter measurement 24
  - 2.5.7 Laser Doppler flowmetry 25
  - 2.5.8 Pulsatile ocular blood flow 25
  - 2.5.9 Retinal function imager 26
  - 2.5.10 Optical Doppler tomography 26

3 Fundamentals of optical coherence tomography 28
- 3.1 Interferometry in OCT 28
  - 3.1.1 The Michelson interferometer 28
  - 3.1.2 Interference and coherence 30
  - 3.1.3 Mathematical description of interferometry in OCT 32
- 3.2 Time domain OCT 37
- 3.3 Fourier domain OCT 38
  - 3.3.1 Mathematical description of FDOCT 39

3.4 Doppler-OCT 42
    3.4.1 Mathematical description of Doppler-OCT 42
    3.4.2 Limitations of Doppler-OCT 49

4 Measurement of large retinal vessels using Doppler OCT 52
4.1 Single beam OCT setup 52
    4.1.1 Light source 52
    4.1.2 Interferometer 54
    4.1.3 Integration of the DVA in the setup 57
    4.1.4 Spectrometer 59
    4.1.5 System parameters 62
4.2 In vitro measurements 68
    4.2.1 Rotating disk 68
    4.2.2 Glass capillary 70
4.3 Data handling 71
    4.3.1 Data acquisition 72
    4.3.2 Data evaluation 75
4.4 In vivo measurements in large retinal veins 82
    4.4.1 Animal preparation 83
    4.4.2 Vasoconstriction measurements 85
    4.4.3 Vasodilation measurements 88
    4.4.4 Discussion 91

5 Assessment of the retinal microcirculation using Doppler OCT 94
5.1 The dual beam OCT method 95
    5.1.1 Experimental dual beam OCT setup 95
    5.1.2 Why is the dual beam setup not usable in practice? 100
5.2 Segmented B-scan method to assess microcirculation 101
    5.2.1 Description of segmented scanning 101
5.3 In vitro experiments using the segmented B-scan method 104
    5.3.1 Artificial eye 104
    5.3.2 Rotating disk 105
    5.3.3 Glass capillary 107
5.4 New data evaluation 108
    5.4.1 Histogram based evaluation method 109
    5.4.2 Histogram simulation 111
5.5 In vivo measurements of the retinal microcirculation 112
    5.5.1 Animal preparation 113
    5.5.2 Experiment protocol 113
    5.5.3 Results 114
    5.5.4 Discussion 118

6 Conclusion 121

7 Outlook **123**

Appendix **125**

A.1 Coherence 125

A.1.1 Relation: coherence time and spectral width 125

A.1.2 Spectral width and relative spectral width 129

A.1.3 FWHM of a Gaussian function 130

A.2 Linear approximation of the wavelength to pixel correlation and rescaling of the spectra 131

A.2.1 Linear approximation of the relationship between λ_x and x . . 131

A.2.2 Rescaling of the spectra 132

Bibliography **136**

Curriculum vitæ **149**

List of figures

Fig. 2.1 Anatomy of the rat eye 17
Fig. 2.2 Anatomy of the retina 18
Fig. 2.3 Fundus image of the rat 19
Fig. 2.4 Anatomy of the human eye 20
Fig. 2.5 Angiographic methods 23

Fig. 3.1 Sketch of the Michelson interferometer 29
Fig. 3.2 Constructive and destructive interference 31
Fig. 3.3 Electrical fields in a Michelson interferometer 33
Fig. 3.4 Spectra of single and multiple reflectors 37
Fig. 3.5 Different sample layer depths 39
Fig. 3.6 Fourier transform of the detector current 41
Fig. 3.7 Doppler-principle: moving source and receiver 43
Fig. 3.8 Doppler angle and vectors in OCT 43

Fig. 4.1 Schematic drawing of the single beam OCT setup 53
Fig. 4.2 Schematic of the galvo-scanner 55
Fig. 4.3 Scanning sample beam 56
Fig. 4.4 DVA rodent setup 58
Fig. 4.5 Functionality of the dichroic mirror 59
Fig. 4.6 Photograph of the spectrometer 60
Fig. 4.7 Illustration of the diffraction grating 60
Fig. 4.8 Schematic drawing of the spectrometer 62
Fig. 4.9 Arbitrary and maximum path length difference detectable by the CCD camera 63
Fig. 4.10 Parameters of a Gaussian beam 65
Fig. 4.11 Schematic of the rotating disk experiment 68
Fig. 4.12 Results of the rotating disk experiment 69
Fig. 4.13 Photograph of the capillary experiment 70
Fig. 4.14 Results of the capillary measurements 71
Fig. 4.15 Saw-tooth function of the fast scanner 72
Fig. 4.16 Front panel of the data acquisition program 73
Fig. 4.17 Amplitude image of the artificial eye before and after subtraction of the reference spectrum 74
Fig. 4.18 Camera saturation 75

Fig. 4.19 Dispersion compensation 77
Fig. 4.20 Amplitude and phase tomogram of one B-scan 78
Fig. 4.21 Sample motion correction 79
Fig. 4.22 Blood vessel area determination 80
Fig. 4.23 Phase wrapping and unwrapping 81
Fig. 4.24 Fitting the vessel data 82
Fig. 4.25 Rat holder 84
Fig. 4.26 Experiment protocol of hyperoxia 85
Fig. 4.27 Oxygen induced vasoconstriction 86
Fig. 4.28 O_2 induced vasoconstriction: change brom baseline 87
Fig. 4.29 Experiment protocol for flicker measurements 89
Fig. 4.30 Flicker light induced vasodilation 90
Fig. 4.31 Flicker light induced vasodilation: change brom baseline 90

Fig. 5.1 Schematic of the dual beam method 96
Fig. 5.2 Schematic drawing of the dual beam OCT setup 97
Fig. 5.3 Photograph of the dual beam setup 98
Fig. 5.4 Scanning sample beams 99
Fig. 5.5 Scanner function of a segmented B-scan 102
Fig. 5.6 Phase difference tomogram obtained from a segmented B-scan . . 103
Fig. 5.7 Phase difference tomogram of an artificial eye 105
Fig. 5.8 Phase difference tomogram of an artificial eye without and with pneumatic dampening 105
Fig. 5.9 Rotating disk measured with segmented B-scan method 106
Fig. 5.10 Capillary measured with segmented B-scan method 107
Fig. 5.11 Results of the capillary measurements using the segmented B-scan method 108
Fig. 5.12 Screenshot of the phase image registration program 109
Fig. 5.13 Histogram of an in vivo measurement 110
Fig. 5.14 Simulated microcirculation data 112
Fig. 5.15 Hyperoxia effect in the microcirculation of one rat 114
Fig. 5.16 Oxygen induced change in the histogram width 115
Fig. 5.17 Microcirculation hyperoxia results of one animal 117
Fig. 5.18 Hyperoxia effect in microcirculation and large vessels, measured in eight animals 118

Fig. A.1 Intensity distribution 128
Fig. A.2 Gaussian power sectrum and spectral bandwidth 129
Fig. A.3 Graph of the rescaling process from λ-space to k-space 133

List of abbreviations

AMD	age-related macula degeneration
CCD	charge-coupled device
CDI	color Doppler imaging
CL	camera lens
CNV	choroidal neovascularisation
CRA	central retinal artery
CRV	central retinal vein
DC	dispersion compensation
DFT	discrete Fourier transform
DG	diffraction grating
DOF	depth of focus
DSPS	Doppler shift power spectrum
DM	dichroic mirror
DVA	dynamic vessel analyzer
FC	fiber collimator
FDOCT	Fourier-domain optical coherence tomography
FFT	fast Fourier transform
FT	Fourier transformation
FWHM	full width at half maximum
GCL	ganglion cell layer

HDD	hard disk drive
HL	halogen lamp
HM	hole mirror
ICG	indocyanine green
ICGA	indocyanine green angiography
ILM	inner limiting membrane
INL	inner nuclear layer
iNOS	inducible nitric oxide synthase
IOP	intraocular pressure
IPL	inner plexiform layer
LDF	laser Doppler flowmetry
LDV	laser Doppler velocimetry
NDF	neutral density filter
NFL	nerve fiber layer
NPDR	nonproliferative diabetic retinopathy
OCT	optical coherence tomography
ODT	optical Doppler tomography
OF	oversampling factor
OFDI	optical frequency-domain imaging
OI	optical isolator
OLM	outer limiting membrane
ONH	optic nerve head
ONL	outer nuclear layer
OPL	outer plexiform layer
PC	polarization controller
PDR	proliferative diabetic retinopathy

POBF	pulsatile ocular blood flow
PRL	photoreceptor layer
RFI	retinal function imager
ROI	region of interest
RPE	retinal pigment epithelium layer
RVA	retinal vessel analyzer
SD	standard deviation
SDOCT	spectral-domain optical coherence tomography
SLD	superluminescent diode
SNR	signal to noise ratio
SSOCT	swept-source optical coherence tomography
TDOCT	time-domain optical coherence tomography
VF	ventilator frequency

1 Introduction

Numerous ocular diseases such as age-related macula degeneration [1, 2], diabetic retinopathy [3–5] and glaucoma [6, 7] are related to abnormalities and disturbances in the retinal perfusion [8]. Thus, several non-invasive blood flow measurement techniques have been developed in the recent years, even though the quantification of the ocular blood flow is quite difficult. In spite of the fact that none of these techniques have found their way into clinical practice, they helped to improve the understanding of the ocular circulatory supply in the recent years [9]. A short overview of the most important methods to assess the ocular blood flow is given in section 2.5.

Using a dynamic vessel analyzer (DVA) and a laser Doppler velocimetry (LDV) system, Garhöfer et al. [10] showed that the interindividual variability of the ocular blood flow is high, which shows that the comparison of absolute retinal blood flow values between individuals is not useful for diagnostics. Therefore, it might be more interesting to study the relative changes in the retinal blood flow due to stimuli (e.g. 100 % oxygen breathing or flicker light) as it has been shown that the oxygen breathing induced vasoconstriction [11] and the vasodilative response to flicker light stimulation [12] of retinal vessels are disturbed in early diabetic retinopathy.

Optical coherence tomography (OCT) is a non-invasive high-resolution imaging technique which has become increasingly prominent in ophthalmology in the recent years. This technique is capable of creating cross-sectional images of tissue structures in real-time, with resolutions comparable to the ones of excisional biopsy and histopathology. Doppler OCT is a functional extension of OCT, which can acquire structural cross-sectional images of the tissue under study and the velocities of moving sample particles (e.g. red blood cells) simultaneously. Lately, this rapidly developing imaging technology has become a well established method for the measurement of the retinal blood flow [8, 13].

The aim of this work was the development of a Doppler OCT system that is capable of measuring relative blood flow changes in large retinal vessels, as well as in the retinal microcirculation of the rat. The system is combined with a DVA rodent for a high precision measurement of the retinal vessels' diameters. The second part of this work, namely the assessment of the retinal microcirculation, required a whole new data acquisition and a new post processing method to be developed. The measurement system's capability to determine changes in the retinal blood flow in large retinal vessels due to 100 % oxygen breathing as well as due to flicker light stimulation was demonstrated in vivo. Furthermore, oxygen breathing induced changes in the blood flow velocities of the retinal microcirculation were detected in the rat.

2 Medical aspects

The eye is the organ that gives us the sense of vision, which is probably the most important of our senses. Humans with healthy eyes rely on them for nearly every activity. Detecting the back-reflected or emitted light from the objects surrounding us and processing this information allows us to see these objects, their shape, dimension and color.

Since numerous ocular diseases can cause loss of vision or even blindness, it is of great interest to gain a better understanding of the mechanisms underlying these eye diseases. A good way to study such diseases under controlled conditions is to use animal models.

In the course of this work, rats were used as animal models for all *in vivo* measurements. A short overview of the anatomy and physiology of the rat eye will be given in the following, as it is of relevance for the understanding of the measurements.

2.1 Anatomy of the rat eye

The main structures which can be found in every mammalian eye [14, 15], thus of course also in the rat eye, are illustrated in Fig. 2.1.

The sclera is the outermost layer of the eye. It is of an opaque white color and has the muscles for the eye movement attached to it. The main functions of the sclera are to serve as protective layer and to maintain the shape of the eye ball since it is an extremely hard, dense and hence unyielding membrane. The front of the eye is formed by the cornea, which is also a very dense but transparent tissue that is connected to the sclera. The cornea does not contain any blood vessels; therefore it is nourished by diffusion from the tear film from the outside and the aqueous humor (the liquid in the anterior and the posterior chamber) from the inside. The choroid is a tissue layer that is directly attached to the inside of the sclera. It consists mainly of the choroidal arteries and veins branching to form a dense capillary meshwork which supplies the outer retinal layers. The innermost layer of the eye, the retina,

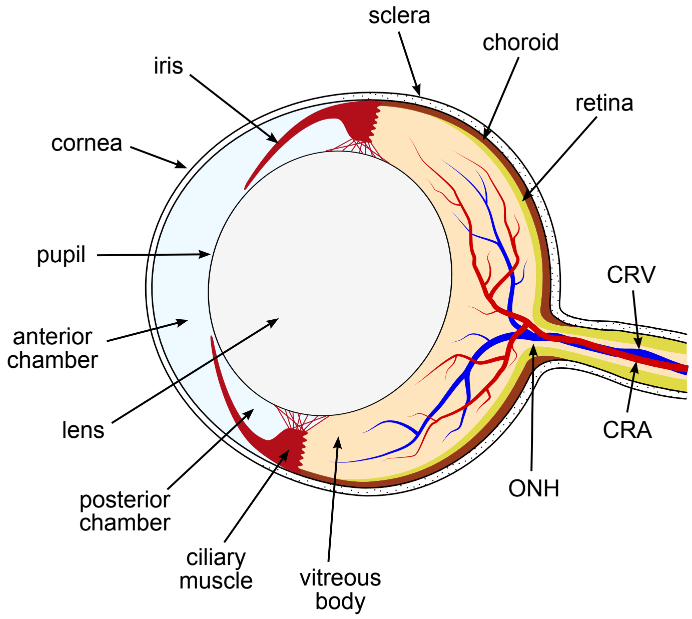

Figure 2.1: Simplified cross-sectional view of the rat eye with its main components (adapted from [16–18]).

is directly adjoined to the choroid and consists of several layers as illustrated in Fig. 2.2. Usually, one distinguishes between the inner retina, which includes all layers between the inner limiting membrane and the outer plexiform layer, and the outer retina, consisting of outer nuclear layer, outer limiting membrane, photoreceptor layer containing the rods (very sensitive low light photoreceptor cells for black-and-white vision) and the cones (photoreceptor cells for color vision), and retinal pigment epithelium layer [19, 20].

Since too high intensities of the incident light can damage the photoreceptors and the other cells in the retina needed for vision, mammalian eyes have an aperture, called the pupil to regulate the intensity of the light passing into the eye. The size of the pupil is determined by the iris which forms the border between anterior and posterior chamber and consists mainly of connective tissue and smooth muscle fibers.

For the brain to receive an image from the eye, light has to pass the refractive media of the eye, namely the cornea, the aqueous humor, the lens and the vitreous humor (the liquid filling the vitreous body). The cornea and the lens focus the incident light on the retina, where the photoreceptors convert captured photons in electrical signals that can be processed by the brain. The total refractive power of the rat eye is around 300 dpt [22].

The pupil can be temporarily dilated by administration of mydriatics such as e.g. atropine or tropicamide; this is necessary for some ophthalmologic examination methods such as, for instance, fundus photography.

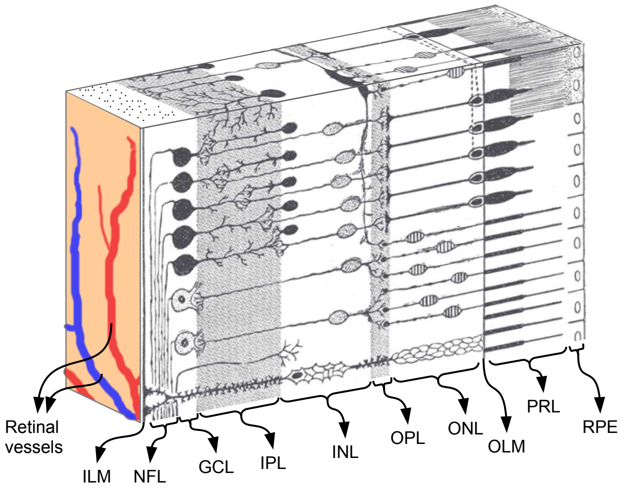

Figure 2.2: Cross-sectional view of the rat retina showing: inner limiting membrane (ILM), nerve fiber layer (NFL), ganglion cell layer (GCL), inner plexiform layer (IPL), inner nuclear layer (INL), outer plexiform layer (OPL), outer nuclear layer (ONL), outer limiting membrane (OLM), photoreceptor layer (PRL) and retinal pigment epithelium layer (RPE) [21].

2.2 Retinal perfusion

The inner retina is supplied with blood, via the central retinal artery (CRA) and drained by the central retinal vein (CRV). Fig. 2.3 shows the branches of the CRA emerging from the optic nerve head (ONH) as well as the big tributaries that form the CRV by their union, leaving the retina through the ONH. The larger retinal vessels are located in the nerve fiber layer (NFL)[i], the arterioles and the venules are distribute throughout the layers of the inner retina reaching as deep as the inner nuclear layer (INL) [23]. They form two capillary networks: the deeper one is located in the inner nuclear layer near the outer plexiform layer while the superficial capillary meshwork lies in the nerve fiber layer or the ganglion cell layer[ii] [24, 25]. The outer plexiform layer is believed to receive its nutrients from both retinal an choroidal vessels. The layers of the outer retina have no blood vessels of their own and are hence nourished from the choroidal capillaries by diffusion [25].

---

[i] The large retinal veins, measured in section 4.4, were located in the NFL.

[ii] The microvessels measured in section 5.5 are mostly capillaries of these two capillary networks, as well as the already mentioned arterioles and venules that are distributed throughout the layers of the inner retina.

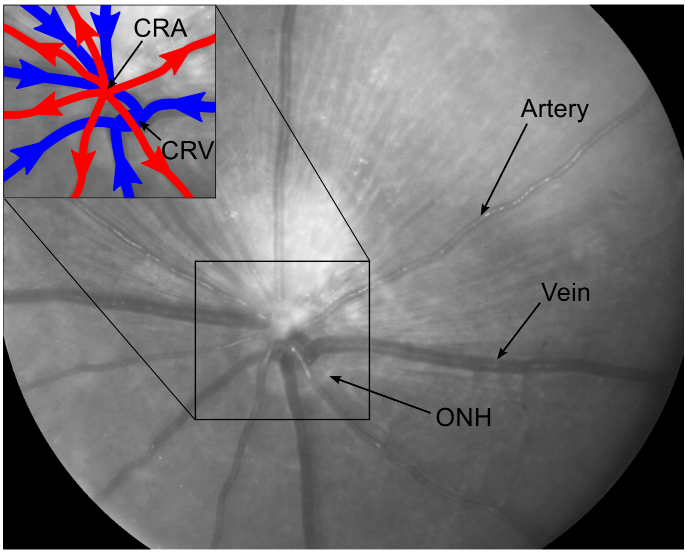

Figure 2.3: Fundus image of a pigmented rat eye; the CRA and the CRV emerge from the ONH and branch to the retinal vasculature network which supplies the whole inner retina.

2.3 Differences between rat eye and human eye

When studying optical diseases in animal models or more precisely in rat eyes, as done in this thesis, it has to be kept in mind that, even though humans and rats are both mammals, there are some major differences between the eyes of those two species. The most obvious difference is the size of the eye ball: while the human eye ball has a length of about 24 mm [19] the rat eye has a length of about 6 mm [22]. The rat eye has a total refractive power of 300 dpt. The lens contributes the main part, namely 80 % of this refraction [22]. The lens occupies approximately 2/3 of the rat eyes' intraocular cavity [26] which leaves less than 30 % for the vitreous body (see Fig. 2.1). In the human eye on the other hand, about 75 % of the refraction happens at the cornea; the total refractive power of the human eye amounts to 59 dpt for a relaxed eye [20]. As illustrated in Fig. 2.4, the vitreous humor fills about 80 % of the human eye ball [19]; consequently, the lens occupies less than 20 % of the eye bulb. Rats have no macula [26, 27] and hence no fovea[iii] which means they have no sharp central vision. Furthermore, rats seem to be unable to accommodate since they can not change the shape of their lenses due to their poorly developed ciliary muscle. Another interesting fact is that rats have photoreceptors for color vision but only for blue and green light [29].

In spite of the large differences between rat eye and human eye, the rat model is often used to study ocular diseases and their underlying mechanisms. There are

---

[iii] The fovea is a cavity in the retina with the highest photoreceptor density of the eye (mostly cones in the human eye), thus, it is responsible for the sharp central vision [28].

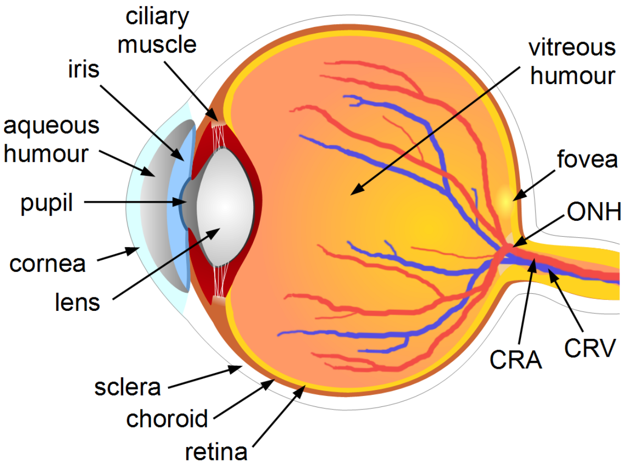

Figure 2.4: Simplified cross-sectional view of the human eye [21].

several reasons for this: rats are cheap, they grow fast and are easily bred, due to their small size, rats are easily handled and can be kept in narrow space, which makes the keeping and the experiments cheaper.

2.4 Ocular Diseases

One reason to perform ophthalmologic animal experiments, is to get proper animal models for human eye diseases or to test medications and hence be able to develop effective treatments for these diseases. Therefore, the most common eye diseases related to disturbed blood flow are described very briefly in this section.

2.4.1 Age-related macula degeneration

Age-related macula degeneration (AMD) is one of the primary reasons for central vision loss in people over 65 years of age in developed countries. This disease mainly affects the choriocapillaris, Bruch's membrane[iv] and the RPE, but the visual loss is due to the photoreceptor dysfunction caused by atrophy and choroidal neovascularisation (CNV). There are two different types of AMD, non-neovascular (dry) AMD which includes 80 % of all diagnosed cases and neovascular (wet) AMD, the more severe form that causes about 80 % of the significant visual disability associated with this disease. The main reason for visual loss from dry AMD is geographical atrophy in the foveal region while wet AMD is characterized by CNV from the choriocapillaris under the macular region. Unfortunately, until now, treatment is largely unsatisfactory and prevention is usually not possible. Furthermore, many of the causes of AMD and CNV are unknown [31].

[iv] Bruch's membrane is located between the RPE and the choroid; it functions as barrier to large molecules and is also known as outer blood-retinal barrier [30].

2.4.2 Diabetic retinopathy

Diabetic retinopathy is still one of the the leading causes for new blindness in most industrialized countries even though it is well treatable: less than 5 % of the patients receiving an early treatment suffer from severe visual loss. Hence, most cases of diabetic retinopathy leading to lost vision can be explained by the delay in seeking medical attention. The early stage of the disease is called nonproliferative diabetic retinopathy (NPDR) and it is characterized by microaneurysms, intraretinal hemorrhage as well as macula edema or retinal thickening where the intercellular fluid comes from diffuse capillary leakage or from leaking microaneurisms. Microvascular occlusions and leakage result in ischemia and nerve fiber infarcts. If the ischemia is severe enough it can lead to neovascular proliferation and vessels start growing at the optic disk or elsewhere in the retina. This stage of the disease is called proliferative diabetic retinopathy (PDR).

Macula edema, exudates and capillary occlusions in NPDR are the primary reasons for legal blindness in diabetics. Patients suffering from NPDR typically maintain at least ambulatory vision. The late stage of PDR is characterized by severe vitreous hemorrhage or retinal detachment, which may result in hand-movements vision or worse [32].

2.4.3 Glaucoma

Glaucoma in all its forms is one of the major causes of irreversible blindness in the world. This disease is a progressive optic neuropathy that is characterized by the loss of retinal ganglion cells and their axons as well as tissue remodeling in the ONH and in the retina. A visible cupping of the optic disc and a measurable thinning of the retinal nerve fiber layer are consequences thereof. Patients suffering from glaucoma experience progressive visual field defects and a decrease in contrast and color sensitivity. Intraocular pressure (IOP) is considered to be one of the major risk factors of glaucoma. The increased IOP is caused by poor drainage of the aqueous humor due to a change in the trabecular meshwork that leads to a higher resistance for the aqueous outflow through the canal of Schlemm (primary open angle glaucoma) or due to blockage of the trabecular meshwork because of a too narrow chamber angle (angle closure glaucoma).

There is increasing evidence that disturbances in the ocular blood flow play a role in the pathogenesis of glaucomatous optic neuropathy; fluctuations in the blood flow appear to be more harmful than a steady reduction of ocular blood flow [20, 33–36].

2.4.4 Venous obstructive disease of the retina

Venous obstructive disease of the retina is the second most common retinal vascular disorder after diabetic retinopathy (see section 2.4.2) and is mostly found in people over 50 years of age. Depending on the vessel that is obstructed it can be divided into central retinal vein obstruction and branch retinal vein obstruction, occurring three times as often as the former. Visual loss is usually caused by macular edema, macular ischemia and vitreous hemorrhage where macular edema is the most common reason for vision loss in retinal vein obstruction. Central retinal vein obstruction can be divided into nonischemic central retinal vein obstruction, $75-80\,\%$ of the patients have this milder form, and ischemic central retinal vein obstruction also known as severe, complete or total vein obstruction, and hemorrhagic retinopathy [37].

2.5 Techniques for measuring retinal blood flow

Since numerous ocular diseases leading to visual loss, including the ones described in section 2.4, are related to abnormal retinal perfusion, a short overview over the most important techniques used to investigate abnormalities in the retinal blood flow will be presented in this section.

2.5.1 Color Doppler imaging

Color Doppler imaging (CDI) is an ultrasound based method that combines cross-sectional tomograms (B-scans) with velocity information gained from the Doppler shift of the moving red blood cells. CDI was developed to monitor the blood flow in the heart and its branching vessels, but this technique can also be used for the blood flow measurement in retrobulbar vessels. CDI systems can measure the peak systolic velocity as well as the end diastolic velocity from which the mean flow velocity can be calculated. One major drawback of this method is the fact that no vessel diameters and hence no total blood flow can be measured [38–40].

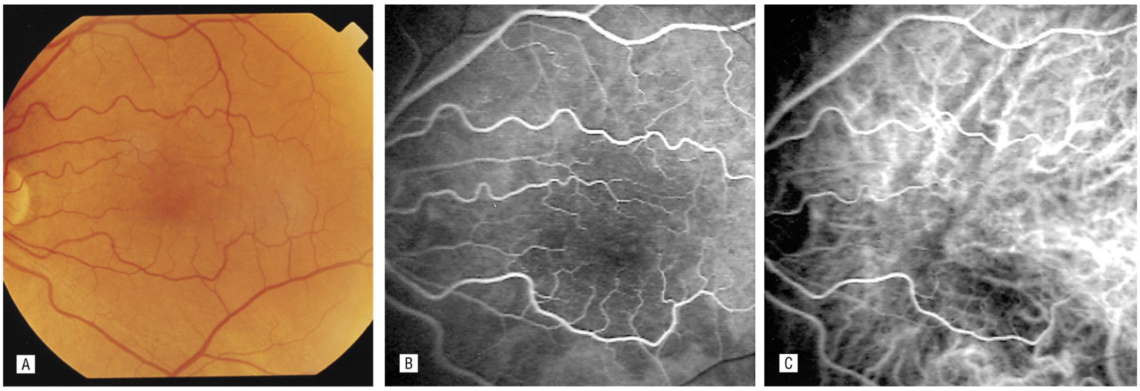

Figure 2.5: Color photograph (a), fluorescein angiography (b) and ICGA (c) of a 72 year-old patient with early AMD [41].

2.5.2 Angiography

Angiography uses a contrast agent, which is usually some kind of dye, that is injected intravenously. The contrast agent is excited with one wavelength and then emits another wavelength which will be detected by a photo camera or a video camera with high resolution. Fluorescein and indocyanine green (ICG) are two commonly used contrast agents in today's clinical practice. While fluorescein is excited with blue light and emits yellow-green light, ICG angiography (ICGA) uses near-infrared light for both excitation and detection. Since infrared light has a higher penetration depth than visible light, ICGA is used to visualize the choroidal vasculature whereas fluorescein angiography mainly shows the retinal vasculature (see Fig. 2.5). Angiographic techniques are usually used for visualization of anatomic structures of the organs under study. However, several attempts have been made to find a way to quantify the retinal blood flow using angiographic methods. Most of these approaches measure the time it takes the contrast agent to pass through a certain retinal or choroidal area. The measurement of blood velocities in retinal capillaries proves to be difficult since it is done by tracking of hyperfluorescent and hypofluorescent dots which requires excellent image quality. The major drawback of these methods is that they are based on the assumption that the blood from one specific retinal artery supplying a certain area is drained by the corresponding vein, which is not necessarily true [38–40].

2.5.3 The blue field entoptic technique

If the retina is illuminated with blue light with a center wavelength of approximately 430 nm and with a narrow bandwidth, the subject under study can observe its own white blood cells in the perifoveal vessels as tiny moving corpuscles. Due to different absorption properties red blood cells absorb the short wavelength light while the white blood cells do not. The effect that one can see ones own moving leukocytes when illuminated with blue light of 430 nm is called blue field entoptic phenomenon [42]. To get quantitative data using this technique, a simulated particle field is shown to the subjects under study, who have to adjust number and mean velocity of the simulated particle field to their own perception of their moving leukocytes. The perifoveal flux of the white blood cells can be estimated from the adjusted simulated particle field. Consequently, this is a very subjective method that needs sufficient cooperation of the subject. Furthermore, it is not clear if the retinal blood flow is directly proportional to the leukocyte flux under all clinical conditions [38–40].

2.5.4 Laser Doppler velocimetry

With laser Doppler velocimetry (LDV) relative blood flow velocities in retinal arterioles and venules can be determined. High coherent laser light is used to illuminate the desired vessel and the beat frequencies between the back reflected Doppler shifted light from the moving red blood cells and the reflected or scattered unshifted light from the vessel wall and the surrounding tissue are detected by a photodiode. These beat frequencies correspond to the Doppler frequency shifts and hence to the velocities in the vessel under study. The maximum frequency shift of the power spectrum is related to the maximum center velocity within the vessel. To measure absolute center blood velocities, a bidirectional LDV setup can be used [43]. The major limitation of the LDV technique is its inability to assess the diameter and hence the blood flow of the vessel under study [38–40].

2.5.5 Laser speckle technique

When coherent light is back scattered from the rough surface of the ocular fundus, an interference pattern that is called ‘speckle pattern’ can be observed. This laser speckle pattern changes rapidly due to the movement of the red blood cells. The rate of this variation gives an estimate of the blood cell velocity and can hence be used for the quantification of the retinal blood flow. Consequently, systems able to assess the retinal, the choroidal and the ONH blood flow velocities have been built. However this technique gives no vessel diameter information and is therefore unable to measure the retinal blood flow [39, 40].

2.5.6 Retinal vessel diameter measurement

To measure relative or absolute blood flow values, the blood flow velocity alone is not enough; it is necessary to know the vessel diameter as well. To obtain the exact vessel diameters, fundus camera based systems like the retinal vessel analyzer (RVA), designed by Imedos (Jena, Germany), have been developed. Adaptive algorithms allow the RVA to track and record the diameters of larger vessels in real-time. The system combines high spatial and temporal resolution with high reproducibility. Aside from the fact that the RVA can only assess diameters of larger vessels, however, the method may also suffer from blurring of the subjects' ocular medium. The combination of velocity and diameter measurements allows the assessment of the ocular blood flow as done e.g. in the Canon Laser Doppler blood flowmeter (Canon; Tokyo, Japan) [39, 40].

2.5.7 Laser Doppler flowmetry

Using the laser Doppler flowmetry (LDF) technique, it is possible to determine the relative blood flow in retinal and choroidal capillary beds: laser light is directed towards vascularized tissue not containing any larger vessels. There, the incident light is scattered by the red blood cells. According to the scattering theory of light in tissue that was formulated by Bonner and Nossal [44], a complete randomization of light directions after scattering on the erythrocytes is assumed. The relative mean velocity data is obtained from the measured Doppler shift power spectrum (DSPS) of the back scattered light. The relative blood volume can be calculated by integrating the DSPS curve and the product of mean velocity and blood volume yields the relative blood flow. Interindividual comparisons of data measured using an LDF system are difficult and generally not recommended since LDF values vary considerably between subjects because they are strongly dependent on the individual vascular density and vessel orientation. Nevertheless, LDF can be used to study the reaction of the ocular vasculature to different physiological and pharmacological stimuli, since it has a high intraindividual reproducibility [38–40].

2.5.8 Pulsatile ocular blood flow

The volume of and the pressure inside the eye change due to the systole and diastole of the cardiac cycle. This is called ocular pulsation. The highest ocular volume and pressure occur during the systole, when the inflow through the ocular arteries exceeds the outflow through the ocular veins. This correlation between volume, pressure and blood flow can be used to estimate the pulsatile ocular blood flow (POBF). Basically, there are two methods to do that. The first approach (the pneumotonometric method) observes the IOP during a cardiac circle; based on a theoretical model, the POBF is calculated from the maximum IOP change during a heart cycle (pulse amplitude). In the second approach (the interferometric method) the change of the distance between cornea and retina due to the varying ocular volume and pressure (ocular fundus pulsation) is measured. Since the interferometric method uses a collimated laser beam that is focused on the retina, no total but only the local POBF can be measured. The major limitation of this technique is the lacking information about the non-pulsatile component of the ocular blood flow [38–40].

2.5.9 Retinal function imager

The retinal function imager (RFI) was originally a brain imaging technique that has been adapted for the retina. It measures intrinsic reflective differences. The technique is able to assess quantitative and qualitative hemodynamic parameters such as retinal blood flow velocity, blood oximetry, metabolic responses to photic stimulation, and to generate capillary perfusion maps that provide retinal vasculature detail similar to fluorescein angiography. The RFI method combines fundus imaging with functional optical imaging: the system is basically a fundus camera with additional imaging and illumination components. The blood flow velocity of secondary and tertiary vessels of the microvasculature is determined by tracking erythrocytes. Hence, the technique is well suited for the measurement of the retinal blood flow in small arterioles, venules and capillaries since they have lower flow velocities. However, the RFI can not track red blood cells with blood flow velocities higher than 20 mm/s. Hence, blood flow velocities in the largest retinal vessels may be to high to be measured using this method. Another drawback of the RFI technique is the lack of vessel diameter information due to resolution limitations of the system. Consequently, the blood flow can not be measured [40, 45].

2.5.10 Optical Doppler tomography

Optical Doppler tomography (ODT) is the method that has been used in this thesis, and will therefore be described in the chapters 3 and 4 in more detail. ODT combines the laser Doppler technique and optical coherence tomography (OCT). In contrast to conventional structural OCT, where only the intensity data is used to visualize the structures of the sample, ODT also uses the phase component of the detected OCT signal to measure the blood flow velocities of the red blood cells in the tissue under study. In addition to the velocity information, this technique is able to obtain velocity profiles in larger vessels as well as to image the retinal and choroidal vasculature of the eye [39, 40].

Furthermore, ODT is capable of vessel diameter measurements, even if, according to Doblhoff-Dier [46] the diameter is underestimated, due to the low velocities at the vessel border[v]. To measure absolute blood flow velocity values a bidirectional

---

[v] The blood flow velocity close to the vessel border is about zero, hence it is difficult to distinguish the regions close the the vessel border from static tissue, which may lead to an underestimation of the vessel diameter.

Doppler OCT setup as introduced by Werkmeister [47] can be used. The combination of a bidirectional Doppler OCT setup with an RVA, to gain more precise vessel diameter values, as done by Doblhoff-Dier [46], makes absolute retinal blood flow measurements possible.

3 Fundamentals of optical coherence tomography

OCT is an optical imaging technique – similar to conventional ultrasound imaging – that can visualize cross-sectional structures in biological tissue. The measurements of the sample, e.g. the subject's eye is contactless and hence non-invasive. Basically, in OCT the 'echo' time[i] delay of the backscattered light beam is measured, as done when using the ultrasound technique. Since the structures in biological tissue have different reflection and scattering properties, one can determine the dimensions of these structures via the echo time. Typical resolutions of OCT systems range from $1-15\,\mu\text{m}$, which is one or two orders of magnitude finer than conventional ultrasound. Due to attenuation from scattering in organic tissue, the penetration depth of OCT is limited to $\sim$2 mm [48].

3.1 Interferometry in OCT

The speed of light is approximately $3 \times 10^8\,\text{m/s}$. Thus, the direct measurement of the echo time delay of light with a resolution of $10\,\mu\text{m}$, which is typical for OCT, is very difficult, as it would require a time resolution of about $30 \times 10^{-15}\,\text{s}$. Therefore, other methods such as e.g. interferometry have to be used. Interferometry is an excellent method to measure the magnitude and the echo time delay of backscattered light with high sensitivity [48].

3.1.1 The Michelson interferometer

OCT is an interferometric imaging technique that uses a broadband light source and a simple Michelson interferometer (Fig. 3.1) to acquire the echo time delay of the light beam illuminating the sample. In the Michelson interferometer, a beam from a light source is split in two beams by a semi-transparent mirror or a beam

---

[i] Echo time is the time it takes the light or sound to return from different axial distances [48].

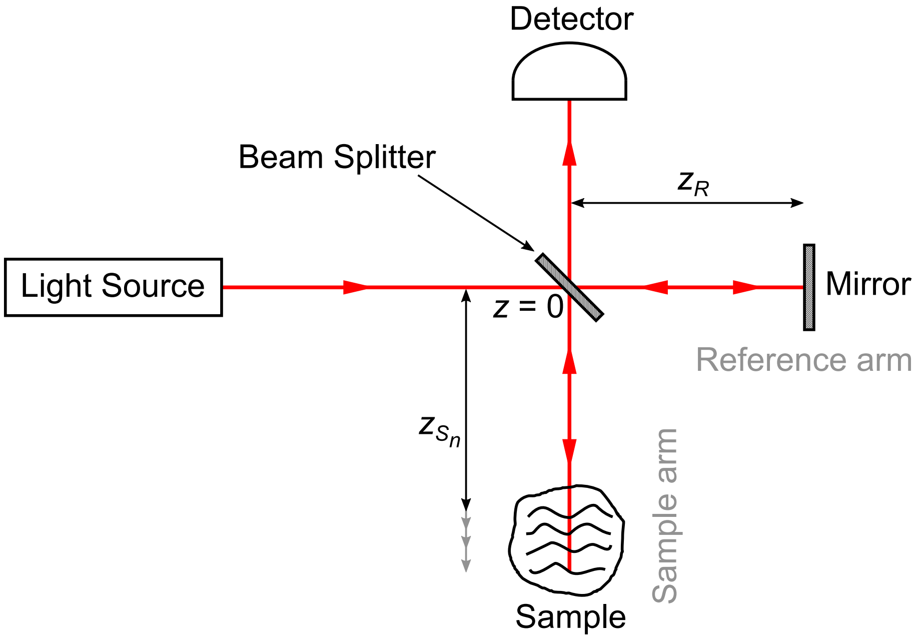

Figure 3.1: Sketch showing the basic principle of a Michelson interferometer (adapted from [49] and [21]).

splitter crystal. One of the beams is referred to as 'reference' beam, the other as 'sample' beam. The reference beam is directed to a mirror at a distance z_R, and backreflected from the mirror to the beam splitter. This part of the interferometer is called 'reference arm'. In the 'sample arm' the sample beam is reflected from one or several layers of the sample at the distances z_{S_n}. The two reflected beams interfere with each other and are then measured with a detector.

Interference will only occur if the optical path length difference ΔL between the two beams is lower than the coherence length (see section 3.1.2) of the light beam. The intensity I_D of the interfering beams at the detector can be written as:

$$I_D \propto |E_R|^2 + |E_S|^2 + 2E_R E_S \cos(2k\Delta L). \tag{3.1}$$

The squared field amplitudes $|E_R|^2$ and $|E_S|^2$ are the intensities of reference and sample beam, respectively, without any interference terms. The last term describes the interference of the two beams, which is dependent on the path length difference $\Delta L = z_R - z_{S_n}$. The double pass of the light through both interferometer arms explains the factor 2 in the argument of the cosine of the interference term. The measurement of the interference and the knowledge of the reference arm length allows the calculation of the distances to the different reflecting layers in the sample.

A more detailed mathematical description of interferometry in OCT will be given in section 3.1.3.

3.1.2 Interference and coherence

To understand interference and coherence one has to look into the wave character of light. Due to the linearity of the wave equation

$$\triangle \boldsymbol{E} = \frac{1}{c^2}\frac{\partial^2 \boldsymbol{E}}{\partial t^2}, \tag{3.2}$$

any linear combination $\boldsymbol{E} = a\boldsymbol{E}_1 + b\boldsymbol{E}_2$ of the arbitrary solutions $\boldsymbol{E}_1$ and $\boldsymbol{E}_2$ is also a solution of the wave equation (3.2). To get the total wave field $\boldsymbol{E}(\boldsymbol{r}, t)$ at a certain point P at the time t, all partial waves $\boldsymbol{E}_m(\boldsymbol{r}, t)$ that overlay each other at P have to be superposed. The total field strength of the wave field

$$\boldsymbol{E}(\boldsymbol{r}, t) = \sum_m \boldsymbol{E}_m(\boldsymbol{r}, t) = \sum_m \boldsymbol{A}_m(\boldsymbol{r}, t)\mathrm{e}^{i\varphi_m} \tag{3.3}$$

depends on the amplitudes $\boldsymbol{A}_m(\boldsymbol{r}, t)$ and the phases φ_m of the superposed partial waves, and is generally location- and time-dependent. This superposition of partial waves is called interference. The location-dependent total intensity $I(\boldsymbol{r}, t) \propto |\boldsymbol{E}(\boldsymbol{r}, t)|^2$ determines the spatial structure of the interference field, i.e. the entire spatial area in which the partial waves interfere.

A temporally stationary interference structure is only possible if the two or more involved partial waves are coherent. If the frequency of two or more harmonic waves is the same but for a constant phase shift $\Delta\varphi = \varphi_i - \varphi_j$, these waves are coherent. Depending on $\Delta\varphi$, their amplitudes will amplify or attenuate each other when superposed: if $\Delta\varphi$ equals zero or a whole-number multiple of 2π, the arriving waves are in phase and interfere constructively (see Fig. 3.2(a)). This means that the resulting amplitude is the sum of the arriving waves' amplitudes. A $\Delta\varphi$ of an uneven multiple of π, on the other hand, results in destructive interference. Hence, the arriving waves are in paraphase, and the resulting amplitude is the difference of their amplitudes (see Fig. 3.2(b)).

Given that light from a hot body is spontaneously emitted by single atoms independent of each other, it is very unlikely that two different light sources 'accidentally' have the same atomic oscillations, and hence emit coherent wave trains. Therefore, to do interferometry with two (or more) light beams, the light of one source has to be split, as done e.g. in the Michelson interferometer (see section 3.1.1). Even though the wave trains in both interferometer arms are from the same light source, they might have gained an optical path length difference ΔL by the time they interfere with each other. This ΔL can be caused by different lengths of the interferometer arms, as well as by reflection, refraction, scattering or diffraction of the light beams.

Even if one splits a single wave train to let it interfere with itself, ΔL must not exceed the coherence length Δl_c, if one wants to see interference effects. The coherence length can be specified as the distance over which a propagating coherent wave

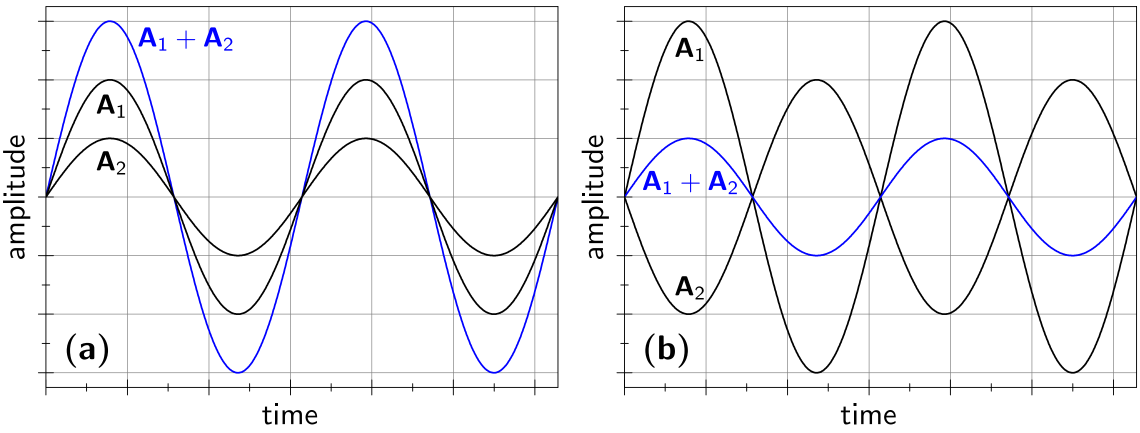

Figure 3.2: (a) Constructive interference, (b) destructive interference of two sine waves with the amplitudes A_1 and A_2 (adapted from Werkmeister [40]).

preserves a defined degree of coherence. The time it takes the light to cover the coherence length is called coherence time Δt_c, thus one can write $\Delta l_c = c \cdot \Delta t_c$. A path length difference ΔL larger than Δl_c, i.e. a time difference between the arriving wave trains larger than Δt_c, implies that these wave trains are not coherent since they have no fixed phase relationship and therefore cannot interfere with each other.

A damped wave train with the decay time Δt_c that is emitted by an atom cannot correspond to an entirely sharp spectral line, but will have a width

$$\Delta\nu \sim \frac{1}{\Delta t_c}. \tag{3.4}$$

A mathematical derivation of this relation between spectral width and coherence time can be found in section A.1.1 or in [50]. As shown in section A.1.2, the relative spectral width is the same in all notations

$$\left|\frac{\delta\lambda}{\lambda}\right| = \left|\frac{\delta\nu}{\nu}\right| = \left|\frac{\delta\omega}{\omega}\right|. \tag{3.5}$$

Using equations (3.4) and (3.5), one can write the longitudinal coherence length as follows:

$$l_c = c \cdot \Delta t_c \sim \frac{c}{\Delta\nu} = \frac{\lambda^2}{\Delta\lambda}. \tag{3.6}$$

In OCT, it is very common to use a light source with a Gaussian shaped spectrum. The Fourier transformation of a Gaussian function yields another Gaussian function, this is also the case for the coherence function of a Gaussian beam: the coherence function of light beam in a Michelson interferometer at the point P is defined as

$$\Gamma(\tau) = \langle E(P, t+\tau) E^*(P, t) \rangle, \tag{3.7}$$

where $\langle\ \rangle$ stands for the time average. $\Gamma(\tau)$ can also be calculated by Fourier transforming the light source spectrum $S(P,\omega)$, with ω being the angular frequency:

$$\Gamma(\tau) = \int_{-\infty}^{\infty} S(P,\omega)\mathrm{e}^{-i\omega\tau} d\omega. \tag{3.8}$$

The light source spectrum is defined as the time-averaged squared amplitudes

$$S(P,\omega) = \langle |E(P,\omega)|^2 \rangle. \tag{3.9}$$

According to Fercher and Hitzenberger [51], the Gaussian coherence function can be written as

$$|\Gamma(\tau)| \propto \exp\left[-\left(\frac{\pi\Delta\nu}{2\sqrt{\ln 2}}\tau\right)^2\right]. \tag{3.10}$$

The full width at half maximum (FWHM) of the coherence function can be defined as the coherence time, which can be calculated to be

$$\Delta t_c = \frac{4\ln 2}{\pi\Delta\nu}, \tag{3.11}$$

as done in section A.1.3. Analogously to equation (3.6), one gets the corresponding Gaussian coherence length

$$l_{c,Gauss} = \frac{4\ln 2}{\pi}\frac{\lambda_0^2}{\Delta\lambda}, \tag{3.12}$$

where λ_0 represents the central wave length and $\Delta\lambda$ the bandwidth (FWHM) of the spectrum emitted by the light source.

3.1.3 Mathematical description of interferometry in OCT

A comprehensive mathematical description of OCT is given by Izatt and Choma [49]. The basic mathematical concept is formulated very precise, and comprehensibly by Doblhoff-Dier [21]. Nevertheless, it will also be given in this section, for the sake of completeness.

The electrical field E_i of the incident beam of a Michelson interferometer (see Fig. 3.3) is defined as

$$E_i = s(k,\omega)\mathrm{e}^{i(kz-\omega t)}. \tag{3.13}$$

The electrical field amplitude $s(k,\omega)$ is dependent on the wave vector k and the angular frequency ω, while the phase term $(kz-\omega t)$ is also dependent on the spatial coordinate z and the time t. As already mentioned in section 3.1.2, the intensity can be written as

$$I(k,\omega) = |E_i|^2. \tag{3.14}$$

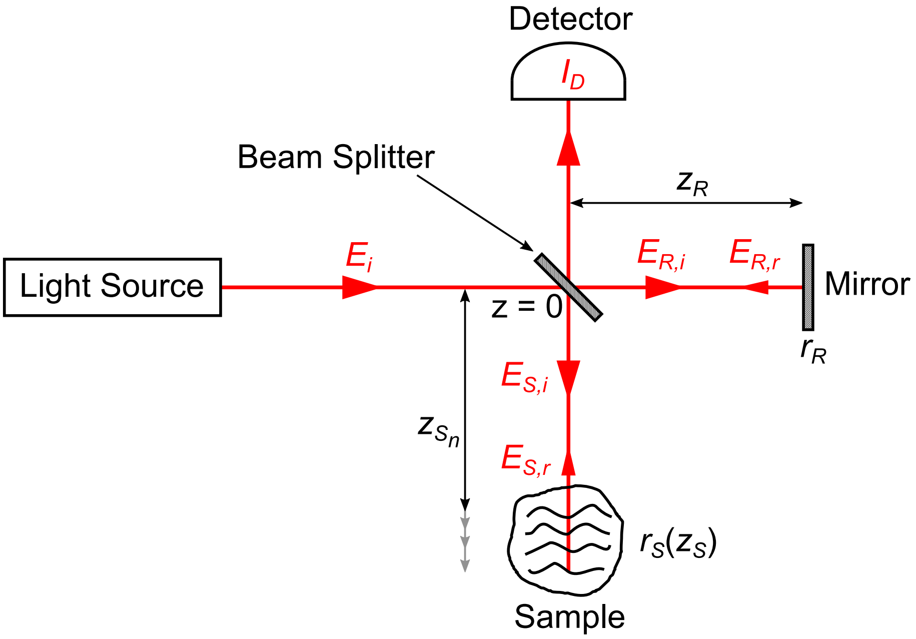

Figure 3.3: Schematic drawing of a Michelson interferometer showing the electrical fields of the different light beams (adapted from [21, 49]).

We assume that the incident beam is split into two beams with identical intensities of $I(k,\omega)/2 = \left|E_i/\sqrt{2}\right|^2$. Hence, we define the electrical fields of the beams entering the reference arm and the sample arm of the interferometer to be

$$E_{R,i} = E_{S,i} = \frac{s(k,\omega)}{\sqrt{2}} \mathrm{e}^{i(kz-\omega t)}, \tag{3.15}$$

respectively. The reference beam is reflected from the reference mirror, having the reflectivity r_R, at the distance z_R from the beam splitter. The electric field of the reflected beam $E_{R,r}$ moves in the opposite direction than the incident beam, which is indicated by the negative sign of kz in the phase term. The additional phase term ϕ_R is due to the beam's way through the reference arm and its reflection on the reference mirror

$$E_{R,r} = \frac{s(k,\omega)}{\sqrt{2}} \cdot r_R \cdot \mathrm{e}^{i(-kz-\omega t+\phi_R)}. \tag{3.16}$$

Since the incident beam and the reflected beam have to be identical at the position of the mirror but for an additional phase term π (due to the reflection at a fixed boundary) and the reflectivity of the mirror r_R, which lowers the amplitude of the reflected beam, one can write

$$\begin{aligned} E_{R,i}(z_R) &= \frac{E_{R,r}(z_R) \cdot \mathrm{e}^{i\pi}}{r_R} \\ \mathrm{e}^{i(kz_R-\omega t)} &= \mathrm{e}^{i(-kz_R-\omega t+\phi_R+\pi)} \\ \phi_R &= 2kz_R - \pi. \end{aligned} \tag{3.17}$$

Inserting this in Eq. (3.16) yields

$$E_{R,r} = \frac{s(k,\omega)}{\sqrt{2}} \cdot r_R \cdot \mathrm{e}^{i(-kz-\omega t+2kz_R-\pi)}. \tag{3.18}$$

Assuming the sample consists of several discrete reflecting layers at the depths z_{S_n}, with insignificant scattering and absorption properties, one can expect the electrical field of the incident beam $E_{S,i}$ to be the same for every sample layer. The reflectivity of all sample layers can be written as $r_S(z_S) = \sum_n r_{S_n} \delta(z_S - z_{S_n})$. Consequently, the electrical field of the reflected sample beam is similar to Eq. (3.18):

$$\begin{aligned} E_{S,r} &= \frac{s(k,\omega)}{\sqrt{2}} \int r_S(z_S) \cdot \mathrm{e}^{i(-kz-\omega t+2kz_S-\pi)} dz_S \\ &= \frac{s(k,\omega)}{\sqrt{2}} \sum_n r_{S_n} \cdot \mathrm{e}^{i(-kz-\omega t+2kz_{S_n}-\pi)}. \end{aligned} \tag{3.19}$$

Both the reflected reference and sample beam are reunited at the beam splitter and half of their intensity is transmitted to the detector. The detection rate of any real detector is much smaller than the oscillation frequency of the light ω[ii]. Therefore, the detector measures a time-average, indicated by $\langle\ \rangle$, of the lights' intensity

$$I_D(k,\omega) = \frac{\rho}{2} \langle |E_{R,r} + E_{S,r}|^2 \rangle, \tag{3.20}$$

where ρ represents the detector responsivity. Inserting Eq. (3.18) and Eq. (3.19) in Eq. (3.20) gives

$$\begin{aligned} I_D(k) = \frac{\rho}{2} \Bigg\langle \Bigg| &\frac{s(k,\omega)}{\sqrt{2}} r_R \mathrm{e}^{i(-kz-\omega t+2kz_R-\pi)} + \\ &+ \frac{s(k,\omega)}{\sqrt{2}} \sum_n r_{S_n} \mathrm{e}^{i(-kz-\omega t+2kz_{S_n}-\pi)} \Bigg|^2 \Bigg\rangle. \end{aligned} \tag{3.21}$$

Rearranging this equation,

$$I_D(k) = \frac{\rho}{2} \left\langle \left| \frac{s(k,\omega)}{\sqrt{2}} \right|^2 \cdot \left| \mathrm{e}^{i(-kz-\omega t-\pi)} \right|^2 \cdot \left| r_R \mathrm{e}^{2ikz_R} + \sum_n r_{S_n} \mathrm{e}^{2ikz_{S_n}} \right|^2 \right\rangle, \tag{3.22}$$

and using the relation $|\mathrm{e}^{ix}|^2 = \mathrm{e}^{ix} \cdot \mathrm{e}^{-ix} = 1$ yields

$$I_D(k) = \frac{\rho}{2} \left\langle \left| \frac{s(k,\omega)}{\sqrt{2}} \right|^2 \cdot \left| r_R \mathrm{e}^{2ikz_R} + \sum_n r_{S_n} \mathrm{e}^{2ikz_{S_n}} \right|^2 \right\rangle. \tag{3.23}$$

[ii] The detection rate used in this work was around 50 µs, while the oscillation frequency of the used light was in the range of a few fs.

Due to its time-independence, the last term can be excluded from the time average. Knowing that the light source spectrum $S(k) = \langle |s(k,\omega)|^2 \rangle$ is the time-averaged squared amplitude, one can rewrite Eq. (3.23) to

$$I_D(k) = \frac{\rho}{4} S(k) \cdot \left| r_R \mathrm{e}^{2ikz_R} + \sum_n r_{S_n} \mathrm{e}^{2ikz_{S_n}} \right|^2 . \tag{3.24}$$

This is the same as

$$\begin{aligned} I_D(k) = \frac{\rho}{4} S(k) \cdot \Bigg[\Bigg(& r_R \mathrm{e}^{2ikz_R} + \sum_n r_{S_n} \mathrm{e}^{2ikz_{S_n}} \Bigg) \cdot \\ & \cdot \Bigg(r_R \mathrm{e}^{-2ikz_R} + \sum_n r_{S_n} \mathrm{e}^{-2ikz_{S_n}} \Bigg) \Bigg] . \end{aligned} \tag{3.25}$$

Expanding the multiplication results in

$$\begin{aligned} I_D(k) = \frac{\rho}{4} S(k) \cdot \Bigg[& r_R^2 + \sum_n r_R r_{S_n} \mathrm{e}^{2ik(z_R - z_{S_n})} + \sum_n z_R z_{S_n} \mathrm{e}^{2ik(z_{S_n} - z_R)} + \\ & + \sum_n \sum_m r_{S_n} r_{S_m} \mathrm{e}^{2ik(z_{S_n} - z_{S_m})} \Bigg] . \end{aligned} \tag{3.26}$$

The double sum can be split in three parts for $n = m$, $n < m$ and $n > m$:

$$\begin{aligned} I_D(k) = \frac{\rho}{4} S(k) \cdot \Bigg[& {r_R}^2 + \sum_n r_R r_{S_n} \mathrm{e}^{2ik(z_R - z_{S_n})} + \sum_n z_R z_{S_n} \mathrm{e}^{-2ik(z_R - z_{S_n})} + \\ & + \sum_n {r_{S_n}}^2 + \sum_{n<m} r_{S_n} r_{S_m} \mathrm{e}^{2ik(z_{S_n} - z_{S_m})} + \sum_{n>m} r_{S_n} r_{S_m} \mathrm{e}^{2ik(z_{S_n} - z_{S_m})} \Bigg] . \end{aligned} \tag{3.27}$$

Using the fact that

$$\sum_{n>m} \mathrm{e}^{2ik(z_{S_n} - z_{S_m})} = \sum_{n<m} \mathrm{e}^{-2ik(z_{S_n} - z_{S_m})} \quad \forall n, m, \tag{3.28}$$

along with the power reflectivity $R = |r|^2$, Eq. (3.27) results in

$$\begin{aligned} I_D(k) = \frac{\rho}{4} S(k) \cdot \Bigg[& R_R + \sum_n R_{S_n} + \\ & + \sum_n \sqrt{R_R R_{S_n}} \left(\mathrm{e}^{2ik(z_R - z_{S_n})} + \mathrm{e}^{-2ik(z_R - z_{S_n})} \right) + \\ & + \sum_{n<m} \sqrt{R_{S_n} R_{S_m}} \left(\mathrm{e}^{2ik(z_{S_n} - z_{S_m})} + \mathrm{e}^{-2ik(z_{S_n} - z_{S_m})} \right) \Bigg] . \end{aligned} \tag{3.29}$$

Making use of the relations

$$\begin{aligned} \sum_{n<m} A_{nm} &= \frac{1}{2}\sum_{n\neq m} A_{nm} \quad \forall n, m && (3.30) \\ \cos x &= \frac{\mathrm{e}^{ix} + \mathrm{e}^{-ix}}{2}, && (3.31) \end{aligned}$$

finally yields

$$\begin{aligned} I_D(k) = {} & \frac{\rho}{4} S(k) \cdot \left(R_R + \sum_n R_{S_n} \right) + \\ & + \frac{\rho}{2} S(k) \cdot \sum_n \sqrt{R_R R_{S_n}} \cos\left(2k(z_R - z_{S_n})\right) + \\ & + \frac{\rho}{4} S(k) \cdot \sum_{n\neq m} \sqrt{R_{S_n} R_{S_m}} \cos\left(2k(z_{S_n} - z_{S_m})\right). \end{aligned} \tag{3.32}$$

The three lines of Eq. (3.32) are referred to as follows, starting at the first line:

1. The *DC-term* is a pathlength-independent offset to the detector current that is scaled by the light source spectrum $S(k)$; it is the largest of the three terms, if the reference reflectivity is higher than the sample reflectivity. The amplitude of the DC-term is proportional to the power reflectivity of the reference mirror plus the sum of the sample reflectivities.
2. The *Cross-correlation terms* are the desired components of the detector current for OCT imaging. Since, they include one term for each sample reflector layer, which depends upon the light source wavenumber as well as the pathlength difference between reference mirror and sample reflectors. Usually, the sum of these components is smaller than the DC-term, given that the components are proportional to the square root of the sample reflectivities.
3. The *Auto-correlation terms* describe the interference of the light reflected from the different sample layers. In typical OCT systems[iii], these terms appear as artifacts. However, the auto-correlation terms can be kept small compared to the cross-correlation terms by the selection of a proper reference reflectivity, due to the fact that the auto-correlations terms are linearly dependent upon the power reflectivity of the sample reflectors [49].

A schematic of the detector current $I_D(k)$ of a single reflector as well as of multiple reflectors is shown in Fig. 3.4. $I_D(k)$ of a sample with a single reflecting layer has no auto-correlation terms, since there can only be auto-correlation between the backreflected light of more than one sample layer. The DC-term of the single reflector in Fig. 3.4 has a height proportional to $\frac{R_R+R_{S_1}}{2}$ and is modulated by the

---

[iii] Common path OCT systems use the auto-correlation terms as desired detector current component [49].

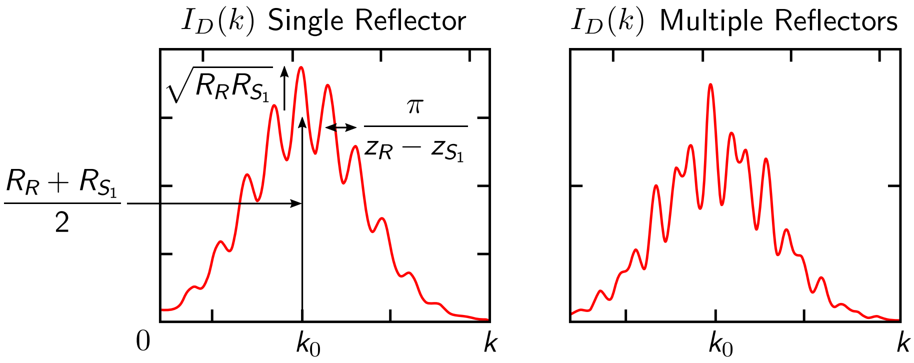

Figure 3.4: Detector current $I_D(k)$ of a single reflector as well as of multiple reflectors. $(R_R + R_{S_1})/2$ is the amplitude of the DC-term, $\sqrt{R_R R_{S_1}}$ represents the amplitude of the cross-correlation component and the cosine of the cross-correlation component has its maximum at $k = \pi/(z_R - z_{S_1})$ (facsimile [49]).

cosinusoidal cross-correlation term that has an amplitude proportional to $\sqrt{R_R R_{S_1}}$. The cosine of the cross-correlation term has its maxima at $k = \pi/(z_R - z_{S_1})$.

The DC-term of a sample consisting of multiple reflecting layers[iv], as shown in Fig. 3.4 (right), is modulated by several cosinusoidal cross-correlation and auto-correlation terms with amplitudes proportional to $\sqrt{R_R R_{S_n}}$ and $\sqrt{R_{S_n} R_{S_m}}$ respectively. The undesired auto-correlation terms are typically small compared to the cross-correlation terms, as the sample reflectivities are much smaller than the reflectivity of the reference mirror. Additionally, the auto-correlation modulation frequencies are smaller than the cross-correlation modulation frequencies, if the distances between the reflecting sample layers are small compared to the distance between reference and sample reflector.

3.2 Time domain OCT

Using the knowledge from section 3.1, time-domain optical coherence tomography (TDOCT) becomes obvious. This method uses an interferometer as shown in Fig. 3.3. To get a depth profile (also known as “A-scan”), the length of the reference arm is varied over time by moving the reference mirror in axial direction, mechanically. Simultaneously, the intensity I_D is recorded by a single-channel photoreceiver. Whenever the reference arm length z_R matches the distance to a reflecting sample layer z_{S_n}, the backreflected light of reference and sample arm interferes constructively. Knowing the positions of the reference mirror and hence the reference arm lengths, it is possible to calculate the sample layer positions from the recorded intensity functions. Due to the mechanical scanning of the reference mirror, this method is very slow and consequently very sensitive to sample motions. Therefore, TDOCT is not usable to acquire in vivo 2D or even 3D data sets. This lack of imaging speed can be overcome by Fourier-domain optical coherence tomography (FDOCT), which is described in the following section.

[iv] Any real tissue sample (e.g. the rat retina) can be considered as a sample consisting of multiple reflecting layers.

3.3 Fourier domain OCT

Basically, there are two types of FDOCT systems: spectral-domain optical coherence tomography (SDOCT) systems, which are spectrometer based, and swept-source optical coherence tomography (SSOCT) (also known as optical frequency-domain imaging (OFDI)), where the light source has a narrow linewidth that is rapidly swept over a broad wavelength range. Since SDOCT was used in this thesis, this method will be described further in the following.

SDOCT uses a broadband light source. The reference mirror of the interferometer is fixed at a position, located such that the reference arm length approximately matches the sample arm length. The interference beam, containing the light returning from the reference arm and from all the depths in the sample, is transmitted through the diffraction grating of a spectrometer. The light beam is dispersed according to its wavelengths, by the diffraction grating. Since, the wavelength is inversely proportional to the frequency $\lambda = \frac{c}{f}$, one can also say that the light beam is dispersed according to its frequency components, which are then detected by a CCD line camera. A closer inspection of the cosine term of Eq. (3.1) or of the cross-correlation terms of Eq. (3.32) reveals that longer pathlength differences $\Delta L = z_R - z_{S_n}$ lead to higher oscillation frequencies in the intensity function. Consequently, reflecting sample layers in different depths yield different interference frequencies in the intensity function as shown in Fig. 3.5(a)-(c). As the line camera detects all dispersed frequency components simultaneously, the whole depth information in one point (one A-scan) is recorded at the same time, while the reference mirror stays at a fixed position. This makes FDOCT much faster than TDOCT.

In a next step, the recorded spectrum is Fourier transformed (FT). The real part of the Fourier transform gives a peak at every contained interference frequency as shown in Fig. 3.5(e). Hence, it is possible to determine the sample layer positions from the frequency components in the spectrum. Therefore, FDOCT is capable of recording a complete depth profile of the sample (A-scan) at an instant. The recording speed of a FDOCT system is only limited by the detection rate of the CCD camera.

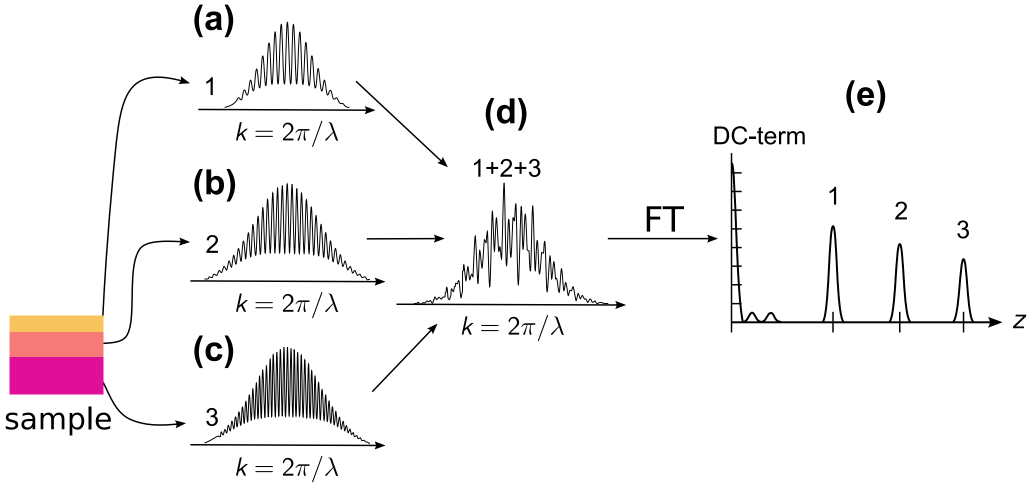

Figure 3.5: The overlay of all interference functions from the reflecting sample layers at different depths (a)-(c), yields the spectrum (d) that is detected by the camera. Larger depths of the sample layers result in interference functions with higher oscillation frequencies. The peaks of the real part of the Fourier transformed spectrum (e) correspond to the sample layer depths (adapted from [52]).

3.3.1 Mathematical description of FDOCT

As in section 3.1.3, a mathematical description of FDOCT is given by Izatt and Choma [49] and is formulated very comprehensibly by Doblhoff-Dier [21]. For a better understanding of the post-processing of the recorded OCT data that was used in this thesis, the same mathematical description will also be given in the following.

To get the depth information of the sample layers, the intensity measured by the detector $I_D(k)$[v] has to be Fourier transformed:

$$i_D(z) = \mathcal{F}\big(I_D(k)\big). \tag{3.33}$$

The Fourier transformation of a function $f(k)$ can be defined as

$$\mathcal{F}(z) = \int_{-\infty}^{\infty} f(k)\mathrm{e}^{-ikz}dk. \tag{3.34}$$

In the following, the Fourier transform of $S(k)$ will be named $\gamma(z)$:

$$S(k) \quad \overset{\mathcal{F}}{\longleftrightarrow} \quad \gamma(z). \tag{3.35}$$

---

[v] As mentioned at the beginning of this section, the diffraction grating of the spectrometer disperses the interference beam according to its different wavelengths and therefore to its different wavenumbers, since $\lambda = \frac{2\pi}{k}$.

In order to calculate the Fourier transform of Eq. (3.32), one has to know the following relations:

$$\begin{aligned} \cos(kz_0) \quad &\overset{\mathcal{F}}{\longleftrightarrow} \quad \frac{1}{2}\left[\delta(z+z_0)+\delta(z-z_0)\right] \qquad (3.36) \\ X(k)\cdot Y(k) \quad &\overset{\mathcal{F}}{\longleftrightarrow} \quad x(z)\otimes y(z), \qquad (3.37) \end{aligned}$$

where $\otimes$ represents the convolution integral

$$(f\otimes g)(z)=\int_{-\infty}^{\infty} f(\tilde{z})g(z-\tilde{z})d\tilde{z}. \qquad (3.38)$$

Thus, the spatial-resolved intensity $i_D(z)$ can be calculated by Fourier transforming Eq. (3.32), which is the intensity $I_D(k)$ measured by the detector:

$$\begin{aligned} i_D(z) = &\frac{\rho}{4}\gamma(z)\cdot\left(R_R+\sum_n R_{S_n}\right)+ \\ &+\frac{\rho}{4}\gamma(z)\otimes\sum_n\sqrt{R_R R_{S_n}}\left[\delta\big(z+2(z_R-z_{S_n})\big)+\delta\big(z-2(z_R-z_{S_n})\big)\right]+ \\ &+\frac{\rho}{8}\gamma(z)\otimes\sum_{n\neq m}\sqrt{R_{S_n}R_{S_m}}\left[\delta\big(z+2(z_{S_n}-z_{S_m})\big)+\delta\big(z-2(z_{S_n}-z_{S_m})\big)\right]. \end{aligned} \qquad (3.39)$$

Knowing that $\delta(x)=\delta(-x)$, one gets the following relation

$$\begin{aligned} f(t)\otimes\delta(t-T) &= \int_{-\infty}^{\infty} f(\tau)\delta(t-T-\tau)d\tau \\ &= \int_{-\infty}^{\infty} f(\tau)\delta(\tau-(t-T))d\tau \\ &= f(t-T), \end{aligned} \qquad (3.40)$$

for the convolution defined in Eq. (3.38).

Using Eq. (3.40) on Eq. (3.39) results in

$$\begin{aligned} i_D(z) = &\frac{\rho}{4}\gamma(z)\cdot\left(R_R+\sum_n R_{S_n}\right)+ \\ &+\frac{\rho}{4}\sum_n\sqrt{R_R R_{S_n}}\left[\gamma\big(z+2(z_R-z_{S_n})\big)+\gamma\big(z-2(z_R-z_{S_n})\big)\right]+ \\ &+\frac{\rho}{8}\sum_{n\neq m}\sqrt{R_{S_n}R_{S_m}}\left[\gamma\big(z+2(z_{S_n}-z_{S_m})\big)+\gamma\big(z-2(z_{S_n}-z_{S_m})\big)\right]. \end{aligned} \qquad (3.41)$$

As in Eq. (3.32), the first line denotes the DC-term, the second line the cross-correlation terms and the third line the auto-correlation terms.

The spatially resolved intensity $i_D(z)$ of a sample with two reflecting layers is shown in Fig. 3.6. The cross-correlation terms of both sample layers and the auto-correlation terms are on one side of the DC-term, while their mirror terms are on the opposite side. The mirror terms of cross-correlation and auto-correlation terms originate from the Fourier transformation of their cosine functions (see Eq. (3.36)), and are therefore identical with their corresponding cross-correlation or auto-correlation terms, except for a sign. As can be seen in Fig. 3.6, the desired positions of the sample layers z_{S_n} can be calculated from $i_D(z)$, as the position of the reference mirror z_R is known. Obviously, this becomes more difficult, if the DC-term is not centered anymore, and cross-correlation terms, auto-correlation terms and their mirror terms start to mix. In that case is not possible to distinguish between the desired peaks of the sample layers and the mirror terms of other sample layers.

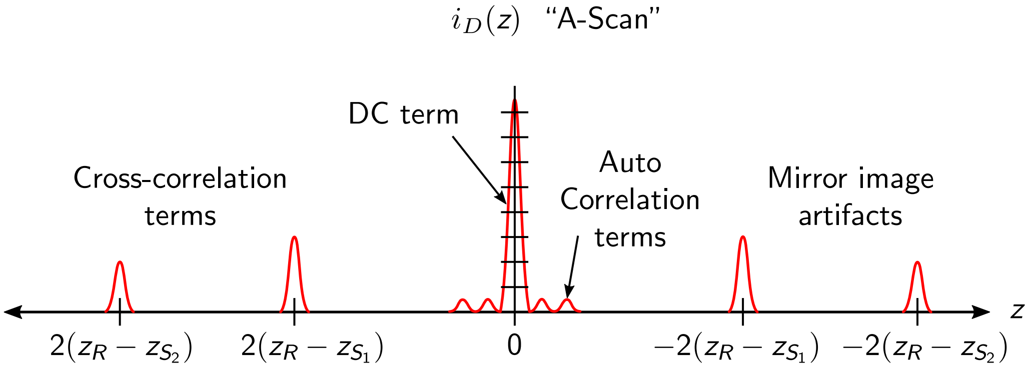

Figure 3.6: Fourier transform $i_D(z)$ of of the detector current $I_D(k)$ with cross-correlation terms of two sample layers, auto-correlation terms and their mirror artifacts, as well as with the DC-term (facsimile [49]).

The easiest way to keep the DC-term centered and thus all sample layer peaks on the same side, is to position the reference mirror at a distance corresponding to the edge of the sample[vi]. Hence, the sample layer distances z_{S_n} are all either smaller or larger than the reference arm length z_R. The disadvantage of this approach is that it can only use half of the available imaging depth, which proves to be no problem for imaging the retina of the eye. However, this method might not be applicable in case of imaging objects with larger depth dimensions.

A large range of literature describes other techniques designed to eliminate the DC-term, the auto-correlation terms or the mirror terms in order to use the full depth range of FDOCT, Wojtkowski et al. [53], Leitgeb et al. [54], Götzinger et al. [55], Baumann et al. [56], to name just a few.

[vi] This method was used in the work at hand, to avoid the overlapping of mirror image artifacts with the desired sample peaks.

However, the best method to eliminate the auto-correlation terms is the usage of a sufficiently high reference reflectivity, so that the amplitude of the auto-correlation terms is very small in comparison to the cross-correlation terms and they can be neglected.

3.4 Doppler-OCT

Doppler-OCT is capable of measuring the velocity of moving particles, e.g. red blood cells in a blood vessel, as is combines the Doppler-principle with the afore described OCT imaging technique. Thus, using Doppler-OCT enables acquiring particle velocity data and structural tissue data simultaneously, as was already mentioned in section 2.5.10.

3.4.1 Mathematical description of Doppler-OCT

A mathematical derivation of the principle of Doppler-OCT can be found in Cheng and Zhang [8], Werkmeister [40] and Doblhoff-Dier [21]. A similar description will also be given in this section.

In the case of sound waves, the Doppler-effect is well-known, describing the change of the sound frequency of a moving sound source. This phenomenon can be observed in everyday life in the change in pitch of the sound of a passing vehicle's horn. The same principle also applies to light waves: if a light beam with the frequency f_0 is emitted by a source moving with the velocity v_S, or if the light receiver moves with the velocity v_R, f_0 is Doppler shifted to the frequency

$$f_D = f_0 \cdot \frac{c - \hat{k} \cdot \vec{v}_R}{c - \hat{k} \cdot \vec{v}_S}, \tag{3.42}$$

where c represents the speed of light and $\hat{k} = \vec{k}/|\vec{k}|$ the unit vector of the light beam. The example in Fig. 3.7 shows a light source and a receiver moving towards each other. Inserting the axial velocity components into Eq. (3.42) changes the sign in the numerator, as $\vec{v}_{R,L}$ points in negative x-direction:

$$f_D = f_0 \cdot \frac{c + v_{R,L}}{c - v_{S,L}}, \tag{3.43}$$

i.e. the Doppler-shifted frequency of the emitted light is higher than the original frequency f_0. If source and receiver moved away from each other, f_0 would be shifted to a lower frequency.

In the case of Doppler-OCT, the incident sample beam with the wave vector $\vec{k}_i$ is emitted by a stationary light source ($\vec{v}_S = 0$) and received by a moving sample

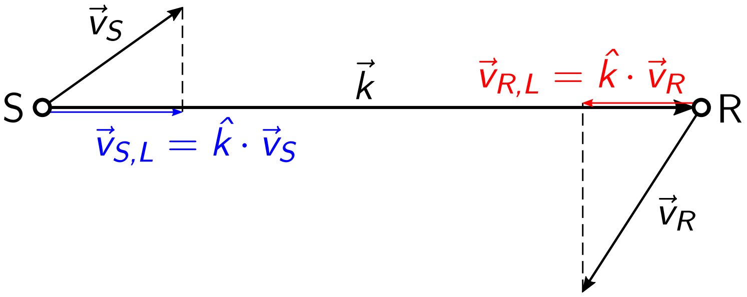
$\vec{v}_S$
S
$\vec{k}$
$\vec{v}_{R,L} = \hat{k} \cdot \vec{v}_R$
R
$\vec{v}_{S,L} = \hat{k} \cdot \vec{v}_S$
$\vec{v}_R$

Figure 3.7: This sketch shows a moving light source S with the velocity $\vec{v}_S$, a moving receiver R with the velocity $\vec{v}_R$ and the wave vector $\vec{k}$ of the light emitted by S.

particle (e.g. red blood cell) with the velocity $\vec{v}_R = \vec{v}$, as depicted in Fig. 3.8. This reduces Eq. (3.42) to

$$f_{D_1} = f_0 \cdot \frac{c - \hat{k}_i \cdot \vec{v}}{c}. \tag{3.44}$$

The back-scattered sample beam $\vec{k}_s$ can be described as another light emission process; where the sample particle is assumed to be a light source moving with the velocity $\vec{v}_S = \vec{v}$ and the detector being the stationary receiver, which yields

$$f_{D_2} = f_{D_1} \cdot \frac{c}{c - \hat{k}_s \cdot \vec{v}} = f_0 \cdot \frac{c - \hat{k}_i \cdot \vec{v}}{c - \hat{k}_s \cdot \vec{v}}. \tag{3.45}$$

The Doppler-shift between incident and scattered beam can now be calculated to be

$$\Delta f_D = f_0 - f_{D_2} = f_0 \cdot \left(1 - \frac{c - \hat{k}_i \cdot \vec{v}}{c - \hat{k}_s \cdot \vec{v}}\right) = f_0 \cdot \frac{(\hat{k}_i - \hat{k}_s) \cdot \vec{v}}{c - \hat{k}_s \cdot \vec{v}}. \tag{3.46}$$

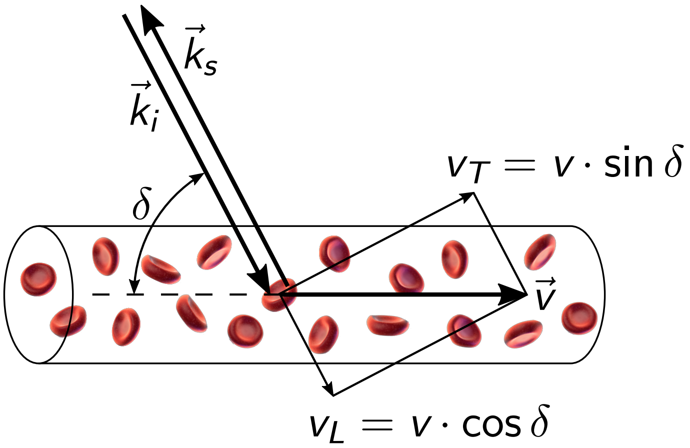

Figure 3.8: Schematic of a blood vessel, showing the velocity vector $\vec{v}$ of a red blood cell, the wave vectors of the incident probe beam $\vec{k}_i$ and the back scattered light $\vec{k}_s$, as well as the Doppler angle δ between probe beam and $\vec{v}$ (adapted from [8, 21, 57]).

Since $|\vec{v}| \ll c$, the term $\hat{k}_s \cdot \vec{v}$ in the denominator can be neglected and $|\vec{k}_i| = |\vec{k}_s| = |\vec{k}|$, which means in this case that $\vec{k}_i = -\vec{k}_s = \vec{k}$. Integrating this and the relation $\hat{k} = \vec{k}/|\vec{k}|$ into Eq. (3.46) yields:

$$\Delta f_D = f_0 \cdot \frac{2\vec{k} \cdot \vec{v}}{|\vec{k}| \cdot c} = f_0 \cdot \frac{2|\vec{k}||\vec{v}| \cdot \cos\delta}{|\vec{k}| \cdot c} = f_0 \cdot \frac{2 \cdot v \cdot \cos\delta}{c}. \tag{3.47}$$

As $f = c/\lambda$, the Doppler-shift can be written as

$$\Delta f_D = v \cdot \frac{2\cos\delta}{\lambda}, \tag{3.48}$$

which indicates that the Doppler frequency shift is proportional to the velocity of the observed particles. If moving particles are measured using an OCT system, the electrical fields of the sample beam (cf. Eq. (3.15), (3.19)) will be changed by the Doppler-shift due to the sample particle's movement.

To describe the Doppler-OCT technique, it is necessary to extend the mathematical descriptions of OCT (see section 3.1.3) and of FDOCT (see section 3.3.1). The electrical fields of the incident reference beam $E_{R,i}$ and the reflected reference beam $E_{R,r}$ were given in section 3.1.3:

$$E_{R,i} = \frac{s(k,\omega)}{\sqrt{2}} \mathrm{e}^{i(kz-\omega t)} \tag{3.49}$$

$$E_{R,r} = \frac{s(k,\omega)}{\sqrt{2}} \cdot r_R \cdot \mathrm{e}^{i(-kz-\omega t+2kz_R-\pi)}. \tag{3.50}$$

Moving sample particles in the n-th layer will Doppler-shift the sample beam by an angular frequency of $\Delta\omega_n$ and by a wave vector of Δk_n. Since there can only be interference between reflected reference beam and reflected sample beam, if both have the same wave vector k and angular frequency ω, we make the ansatz of an incident sample beam with the wave vector $(k + \Delta k_n)$ and the angular frequency $(\omega + \Delta\omega_n)$

$$E_{S,i} = \frac{s(k,\omega)}{\sqrt{2}} \mathrm{e}^{i[(k+\Delta k_n)z-(\omega+\Delta\omega_n)t]}. \tag{3.51}$$

Due to the reflection at a moving sample particle in the n-th layer, $E_{S,i}$ is Doppler-shifted and wave vector as well as angular frequency of the reflected sample beam

$$E_{S_n,r} = \frac{s(k,\omega)}{\sqrt{2}} \cdot r_{S_n} \cdot \mathrm{e}^{i(-kz-\omega t+\phi_S)} \tag{3.52}$$

match the ones of the reflected reference beam $E_{R,r}$. As in Eq. (3.17) in section 3.1.3, the additional phase term ϕ_S can be calculated by using the fact that the incident and reflected beam have to be identical at the position z_{S_n} of the reflecting sample particle, but for the reflectivity r_{S_n} and an additional phase term π due to the reflection:

$$\begin{aligned} E_{S,i}(z_{S_n}) &= \frac{E_{S_n,r}(z_{S_n}) \cdot \mathrm{e}^{i\pi}}{r_{S_n}} \\ \mathrm{e}^{i[(k+\Delta k_n)z_{S_n}-(\omega+\Delta\omega_n)t]} &= \mathrm{e}^{i(-kz_{S_n}-\omega t+\phi_S+\pi)} \\ \phi_S &= 2kz_{S_n} + \Delta k_n z_{S_n} - \Delta\omega_n t - \pi. \end{aligned} \tag{3.53}$$

This yields the electric field of the sample beam reflected at the n-th sample layer:

$$E_{S_n,r} = \frac{s(k,\omega)}{\sqrt{2}} \cdot r_{S_n} \cdot \mathrm{e}^{i(-kz-\omega t+2kz_{S_n}+\Delta k_n z_{S_n}-\Delta\omega_n t-\pi)} \tag{3.54}$$

and consequently the total electrical field exiting the sample arm:

$$E_{S_n,r} = \frac{s(k,\omega)}{\sqrt{2}} \cdot \sum_n r_{S_n} \cdot \mathrm{e}^{i(-kz-\omega t+2kz_{S_n}+\Delta k_n z_{S_n}-\Delta\omega_n t-\pi)}. \tag{3.55}$$

Inserting this in Eq. (3.20) gives

$$\begin{aligned} I_D(k) = \frac{\rho}{2}\Bigg\langle\Bigg| &\frac{s(k,\omega)}{\sqrt{2}} r_R \cdot \mathrm{e}^{i(-kz-\omega t+2kz_R-\pi)} + \\ &+ \frac{s(k,\omega)}{\sqrt{2}} \cdot \sum_n r_{S_n} \cdot \mathrm{e}^{i(-kz-\omega t+2kz_{S_n}+\Delta k_n z_{S_n}-\Delta\omega_n t-\pi)}\Bigg|^2\Bigg\rangle. \end{aligned} \tag{3.56}$$

After performing the steps in Eq. (3.22)-(3.32) one arrives at:

$$\begin{aligned} I_D(k) = &\frac{\rho}{4} S(k) \cdot \left(R_R + \sum_n R_{S_n} \right) + \\ &+ \frac{\rho}{2} S(k) \cdot \sum_n \sqrt{R_R R_{S_n}} \cdot \Big\langle \cos\big(2k(z_R - z_{S_n}) - \Delta k_n z_{s_n} + \Delta\omega_n t\big)\Big\rangle + \\ &+ \frac{\rho}{4} S(k) \cdot \sum_{n\neq m} \sqrt{R_{S_n} R_{S_m}} \cdot \\ &\cdot \Big\langle \cos\big(2k(z_{S_n} - z_{S_m}) + \Delta k_n z_{S_n} - \Delta k_m z_{S_m} + (\Delta\omega_m - \Delta\omega_n)t\big)\Big\rangle. \end{aligned} \tag{3.57}$$

This equation looks similar to Eq. (3.32) except for additional phase terms in the cosine functions. As in section 3.1.3, the first line is the DC-term, the second line are the cross-correlation terms, which are relevant for OCT, and the remaining terms are the auto-correlation terms. The additional phase terms in the cross-correlation terms of Eq. (3.57) describe the Doppler-shift of the sample beam; they are composed of a constant phase offset, dependent on the wave vector shift Δk_n and the sample layer depth z_{S_n}, as well as a term, which changes with time and is dependent on the shift of the angular frequency $\Delta\omega_n$.

As the cosine functions in Eq. (3.57) are time-dependent, they cannot be excluded from the time average as done in section 3.1.3, i.e. the time average of the cross-correlation and the auto-correlation terms still needs to be carried out. In Doppler OCT, the duration of the data acquisition is defined by the exposure time τ of the CCD camera. Thus, the interval of the time average starts at the time t_0 and ends at τ. Since, the cosine arguments of Eq. (3.57) are of the form $(a + bt)$, their time average can be written as

$$\begin{aligned}\frac{1}{\tau}\int\limits_{t_0}^{t_0+\tau} \cos\left(a+bt\right)\,dt &= \left.\frac{\sin\left(a+bt\right)}{b\tau}\right|_{t_0}^{t_0+\tau} \\ &= \frac{\sin\left(a+bt_0+b\tau\right)-\sin\left(a+bt_0\right)}{b\tau} \\ &= \frac{\sin\left[\left(a+bt_0+\frac{b\tau}{2}\right)+\frac{b\tau}{2}\right]-\sin\left[\left(a+bt_0+\frac{b\tau}{2}\right)-\frac{b\tau}{2}\right]}{b\tau}\end{aligned} \tag{3.58}$$

The last step was done to get a function of the form $\sin(c + d) - \sin(c - d)$, so that the following relation can be used:

$$\sin(c \pm d) = \sin c \cdot \cos d \pm \cos c \cdot \sin d. \tag{3.59}$$

Using this relation with Eq. (3.58) yields:

$$\begin{aligned}\frac{1}{\tau}\int\limits_{t_0}^{t_0+\tau} \cos\left(a+bt\right)\,dt = \frac{1}{b\tau}\Bigg[&\sin\left(a+bt_0+\frac{b\tau}{2}\right)\cdot\cos\left(\frac{b\tau}{2}\right)+ \\ &+\cos\left(a+bt_0+\frac{b\tau}{2}\right)\cdot\sin\left(\frac{b\tau}{2}\right)- \\ &-\sin\left(a+bt_0+\frac{b\tau}{2}\right)\cdot\cos\left(\frac{b\tau}{2}\right)+ \\ &+\cos\left(a+bt_0+\frac{b\tau}{2}\right)\cdot\sin\left(\frac{b\tau}{2}\right)\Bigg].\end{aligned} \tag{3.60}$$

The sine terms cancel each other out and the time average becomes

$$\frac{1}{\tau}\int\limits_{t_0}^{t_0+\tau} \cos\left(a+bt\right)\,dt = \frac{2}{b\tau}\cdot\cos\left(a+bt_0+\frac{b\tau}{2}\right)\cdot\sin\left(\frac{b\tau}{2}\right) \tag{3.61}$$

Applying this result to Eq. (3.57) gives the time averaged intensity, recorded by the camera, starting at the time t_0, during the exposure time τ:

$$\begin{aligned}I_D(k,t_0) = \frac{\rho}{4}S(k)\cdot\left(R_R+\sum_n R_{S_n}\right)+&\\+\frac{\rho}{2}S(k)\cdot\sum_n\sqrt{R_R R_{S_n}}\cdot\frac{2}{\Delta\omega_n\tau}\cdot\sin\left(\frac{\Delta\omega_n\tau}{2}\right)\cdot&\\\cdot\cos\left(2k(z_R-z_{S_n})-\Delta k_n z_{S_n}+\Delta\omega_n t_0+\frac{\Delta\omega_n\tau}{2}\right)+&\\+\frac{\rho}{4}S(k)\cdot\sum_{n\neq m}\sqrt{R_{S_n}R_{S_m}}\cdot\frac{2}{(\Delta\omega_m-\Delta\omega_n)\tau}\cdot\sin\left(\frac{(\Delta\omega_m-\Delta\omega_n)\tau}{2}\right)\cdot&\\\cdot\cos\Bigg(2k(z_{S_n}-z_{S_m})+\Delta k_n z_{S_n}-\Delta k_m z_{S_m}+&\\+(\Delta\omega_m-\Delta\omega_n)t_0+\frac{(\Delta\omega_m-\Delta\omega_n)\tau}{2}\Bigg).&\end{aligned}\tag{3.62}$$

This intensity function describes the interference between a reference beam and a Doppler-shifted sample beam. Except for additional phase terms in the cosine functions as well as additional amplitude factors of the form $\frac{2}{x}\cdot\sin\left(\frac{x}{2}\right)$, the equations (3.62) and (3.32) are equal.

For small sample velocities and thus small Doppler-shifts $\Delta\omega_n$, the terms $\sin\left(\frac{\Delta\omega_n\tau}{2}\right)\approx\left(\frac{\Delta\omega_n\tau}{2}\right)$ and $\sin\left(\frac{(\Delta\omega_m-\Delta\omega_n)\tau}{2}\right)\approx\frac{(\Delta\omega_m-\Delta\omega_n)\tau}{2}$ cancel out with $\frac{2}{\Delta\omega_n\tau}$ and $\frac{2}{(\Delta\omega_m-\Delta\omega_n)\tau}$ respectively. Hence, Eq. (3.62) becomes identical with the not Doppler-shifted intensity function in Eq. (3.32), in the limit of vanishing Doppler-shifts.

In case of Doppler-FDOCT, Eq. (3.62) has to be Fourier transformed to obtain the depth information of the sample layers. Using the relation

$$\cos(kz_0+\psi)\quad\overset{\mathcal{F}}{\longleftrightarrow}\quad\frac{1}{2}\left[\mathrm{e}^{-i\psi}\delta(z+z_0)+\mathrm{e}^{i\psi}\delta(z-z_0)\right],\tag{3.63}$$

along with the steps from section 3.3.1 in Eq. (3.62) yields the spatially resolved detector current $i_D(z,t_0)$, which is the Fourier transform of $I_D(k,t_0)$:

$$\begin{aligned}
i_D(z,t_0) = {} & \frac{\rho}{4}\cdot\gamma(z)\cdot\left(R_R+\sum_n R_{S_n}\right)+\\
&+\frac{\rho}{4}\cdot\sum_n\sqrt{R_R R_{S_n}}\cdot\frac{2}{\Delta\omega_n\tau}\cdot\sin\left(\frac{\Delta\omega_n\tau}{2}\right)\cdot\\
&\quad\cdot\Big[\gamma\big(z+2(z_R-z_{S_n})\big)\cdot\mathrm{e}^{-i\left(-\Delta k_n z_{S_n}+\Delta\omega_n t_0+\frac{\Delta\omega_n\tau}{2}\right)}+\\
&\quad+\gamma\big(z-2(z_R-z_{S_n})\big)\cdot\mathrm{e}^{i\left(-\Delta k_n z_{S_n}+\Delta\omega_n t_0+\frac{\Delta\omega_n\tau}{2}\right)}\Big]+\\
&+\frac{\rho}{8}\cdot\sum_{n\neq m}\sqrt{R_{S_n}R_{S_m}}\cdot\frac{2}{(\Delta\omega_m-\Delta\omega_n)\tau}\cdot\sin\left(\frac{(\Delta\omega_m-\Delta\omega_n)\tau}{2}\right)\cdot\\
&\quad\cdot\Big[\gamma\big(z+2(z_{S_n}-z_{S_m})\big)\cdot\mathrm{e}^{-i\left(\Delta k_n z_{S_n}-\Delta k_m z_{S_m}+(\Delta\omega_m-\Delta\omega_n)t_0+\frac{(\Delta\omega_m-\Delta\omega_n)\tau}{2}\right)}+\\
&\quad+\gamma\big(z-2(z_{S_n}-z_{S_m})\big)\cdot\mathrm{e}^{i\left(\Delta k_n z_{S_n}-\Delta k_m z_{S_m}+(\Delta\omega_m-\Delta\omega_n)t_0+\frac{(\Delta\omega_m-\Delta\omega_n)\tau}{2}\right)}\Big].
\end{aligned}\tag{3.64}$$

The depth information of the sample layers, as well as the Doppler-shift or the sample velocity information, are encoded in the cross-correlation terms. The DC-term, the auto-correlation terms and the cross-correlation terms' mirror terms can be disregarded, as their overlapping was avoided in the course of this work by positioning the reference mirror at a distance corresponding the the edge of the sample (see section 3.3.1 for explanation). This leaves the cross-correlation terms without their mirror terms

$$\begin{aligned}
i^{cross}(z,t_0) = {} & \frac{\rho}{4}\cdot\sum_n\sqrt{R_R R_{S_n}}\cdot\frac{2}{\Delta\omega_n\tau}\cdot\sin\left(\frac{\Delta\omega_n\tau}{2}\right)\cdot\\
&\cdot\gamma\big(z-2(z_R-z_{S_n})\big)\cdot\mathrm{e}^{i\left(-\Delta k_n z_{S_n}+\Delta\omega_n t_0+\frac{\Delta\omega_n\tau}{2}\right)}.
\end{aligned}\tag{3.65}$$

The cross-correlation term of a particle in the n-th sample layer, measured at the starting time t_0, can be selected by setting $z = 2(z_R - z_{S_n})$[vii], as illustrated in Fig. 3.6:

$$i_n^{cross}(t_0)=\frac{\rho}{4}\cdot\sqrt{R_R R_{S_n}}\cdot\frac{2}{\Delta\omega_n\tau}\cdot\sin\left(\frac{\Delta\omega_n\tau}{2}\right)\cdot\gamma(0)\cdot\mathrm{e}^{i\left(-\Delta k_n z_{S_n}+\Delta\omega_n t_0+\frac{\Delta\omega_n\tau}{2}\right)}.\tag{3.66}$$

A consecutive scan, which is recorded at the same position at a different starting time point $t_0 + \tau$ can be written as

$$\begin{aligned}
i_n^{cross}(t_0+\tau) = {} & \frac{\rho}{4}\cdot\sqrt{R_R R_{S_n}}\cdot\frac{2}{\Delta\omega_n\tau}\cdot\sin\left(\frac{\Delta\omega_n\tau}{2}\right)\cdot\\
&\cdot\gamma(0)\cdot\mathrm{e}^{i\left(-\Delta k_n z_{S_n}+\Delta\omega_n(t_0+\tau)+\frac{\Delta\omega_n\tau}{2}\right)}.
\end{aligned}\tag{3.67}$$

[vii] This is only possible if the coherence function $\gamma(z)$ is narrow enough to distinguish different sample layers.

To get the phase difference of the two measurements, their quotient has to be calculated:

$$\mathrm{e}^{i\Delta\phi_D} = \frac{i_n^{cross}(t_0+\tau)}{i_n^{cross}(t_0)} = \mathrm{e}^{i\Delta\omega_n\tau}. \tag{3.68}$$

The resulting phase difference depends on the Doppler-shift of the angular frequency $\Delta\omega_n$ and on the time span τ between the recording of the two consecutive measurements:

$$\Delta\phi_D = \Delta\omega_n \cdot \tau = 2\pi\Delta f_D \cdot \tau. \tag{3.69}$$

Inserting Eq. (3.48) for the Doppler-shift Δf_D yields

$$\Delta\phi_D = 2\pi v \cdot \frac{2\cos\delta}{\lambda} \cdot \tau. \tag{3.70}$$

Therefore, the velocity of a moving sample particle can be written as

$$v = \Delta\phi_D \cdot \frac{\lambda}{4\pi\tau \cdot \cos\delta}. \tag{3.71}$$

This equation only holds true if the sample particle is measured in vacuum. As this is not the case in a blood vessel, one has to consider that the phase velocity of light in a medium

$$v_{ph} = \frac{c}{n} \tag{3.72}$$

is slower than the speed of light in vacuum c, where n represents the refractive index of the medium. The equation $\lambda_0 = c/f$, describing the relation between wavelength and frequency in vacuum, has to be changed to $\lambda = v_{ph}/f$ for a light wave propagating inside a medium, with a constant frequency. Consequently, the wavelength of a light wave in a medium can be written as

$$\lambda = \frac{\lambda_0}{n}. \tag{3.73}$$

This changes the velocity of a sample particle (e.g. red blood cell) to

$$v = \Delta\phi_D \cdot \frac{\lambda_0}{4\pi\tau n \cdot \cos\delta}, \tag{3.74}$$

with λ_0 being the center wavelength of the measurement beam and n being the refractive index of the sample.

3.4.2 Limitations of Doppler-OCT

The measurement of flow velocities via the phase difference of two adjacent A-scans, which is described above, may prove problematic in the case of high velocities, since all phase values $\phi + 2m\pi$, $m \in \mathbb{Z}$ describe the same physical state. Thus, a measured velocity value proportional to the phase difference $\Delta\phi_D$ cannot be distinguished from

a velocity value proportional to $\Delta\phi_D + 2m\pi$; this behavior is called "phase wrapping". If the phase shift exceeds $\pm\pi$, phase wrapping will be encountered and the phase values cannot be obtained unambiguously anymore. If so, the phase data has to be unwrapped as explained with the blood vessel evaluation in section 4.3.2. The closer the Doppler angle comes to 90°, however, the larger the velocities which can be measured unambiguously: this is due to the fact that Doppler OCT uses only the longitudinal velocity component, which decreases when δ approaches 90° (see Fig. 3.8). Thus, the phase shift also decreases, as it is proportional to the longitudinal velocity component.
Regarding high velocities at Doppler angles close to 90°, another issue arises, however, as explained by Koch et al. [58]: for high velocity components transversal to the measurement beam, the phase shift is no longer proportional and can even become independent of the velocity of the sample particle. This effect could be neglected for the measurements conducted in this work, due to the fact that all vessels were measured at a distance of about one optic disk diameter from the ONH, thus the blood flow velocities did not exceed 25 mm/s [59, 60]. In this range, the phase shift is still proportional to the sample velocity [58]. However, if considering measurements of vessels with higher blood flow velocities than in the retinal vessels, this effect cannot be disregarded.

As mentioned above, Doppler-OCT is only capable of measuring the longitudinal component of a sample particle's velocity (see Fig. 3.8). Thus, it is obvious that this method cannot gain velocity information of vessels perpendicular to the sample beam, given that the longitudinal velocity component would equal zero in this case[viii]. Also, Eq. (3.74) is not defined in case of $\delta = 90°$, since it would contain a division by zero.

A major drawback of the single beam Doppler-OCT technique, described in the previous section, is the missing knowledge of the Doppler angle. Consequently, no absolute velocity data is available. Nevertheless, this method was used in the course of the work at hand, as relative velocity measurements were sufficient to show the discussed effects. Besides, it is questionable if absolute ocular blood flow values of rats would prove useful, as they cannot be compared to human blood flow data due to the differences between human eyes and rat eyes (see section 2.3). Furthermore, anesthesia was used on the animals during the experiments, which is not the case when performing OCT measurements in human eyes.

However, there are several approaches to measure absolute blood flow velocity data, using Doppler-OCT. Some of them are applicable to single beam systems [61–63], while other methods require more sophisticated experimental setups, using two [21, 40, 43] or even three measurement beams [64].

[viii] If this problem was encountered during the measurements conducted in the course of this thesis, it was simply avoided by changing the Doppler angle; this was achieved by a slight change of the animal's position as well as a constant offset to the sample beam, if needed.

4 Measurement of large retinal vessels using Doppler OCT

This chapter will explain the setup, as well as the mode of operation of the single beam Doppler OCT system that was built in the course of the work at hand. Furthermore, in vitro experiments conducted to test the system's performance as well as in vivo measurements in large retinal veins will be described.

4.1 Single beam OCT setup

The experimental single beam OCT setup basically consists of a Michelson interferometer as described in section 3.1 and a spectrometer, which will be specified in section 4.1.4. Furthermore, a fundus camera based RVA system (DVA rodent, Imedos, Jena, Germany) is combined with the setup: it provides continuous high precision measurements of the vessel diameters. A schematic drawing of the experimental setup can be found in Fig. 4.1.

4.1.1 Light source

The light source that was used for the single beam OCT setup is a superluminescent diode (SLD), which is a very common light source type in OCT imaging. An SLD is basically a pn-junction that is biased in forward direction, which leads to population inversion and spontaneous recombination of electrons and holes. Given that the pn-junction is made of e.g. GaAs[i], the energy of the spontaneous recombinations is emitted as photons and heat. This amplified spontaneous emission of light is also known as superluminescence. SLDs are designed such that the charge carriers can have numerous different energy states, which results in photons with different wavelengths. Thus, the light spectra emitted by SLDs are typically very broadband.

---

[i] In diodes made of some other semiconductors as e.g. silicon, the recombination energy is only released in the form of heat.

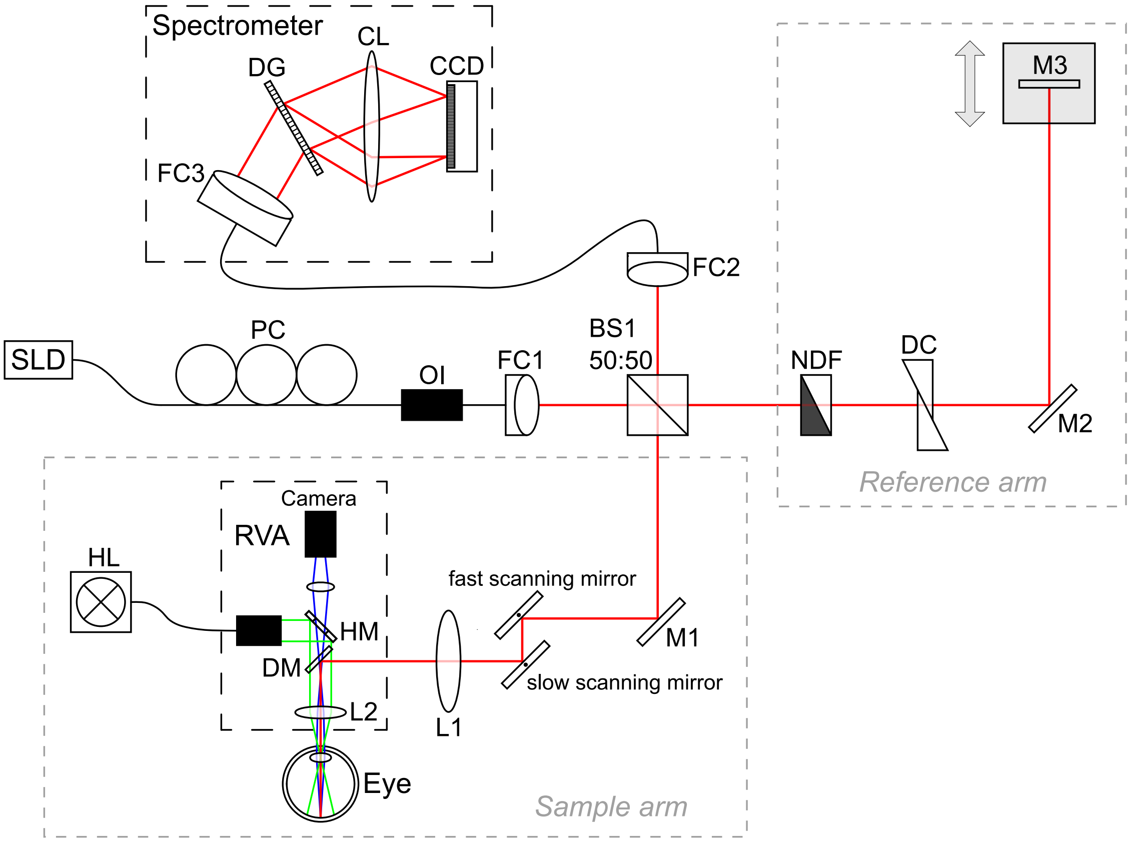
Spectrometer
CL
DG
CCD
FC3
M3
FC2
PC
BS1
50:50
SLD
OI
FC1
NDF
DC
M2
Reference arm
Camera
RVA
HL
fast scanning mirror
HM
M1
DM
slow scanning mirror
L2
L1
Eye
Sample arm

Figure 4.1: Schematic drawing of the experimental single beam OCT setup combined with the RVA. SLD = superluminescent diode, PC = polarization controller, OI = optical isolator, FC = fiber collimator, BS = beam splitter, M = mirror, NDF = neutral density filter, DC = dispersion compensation, L = lens, HM = hole mirror, DM = dichroic mirror, HL = halogen lamp, DG = diffraction grating, CL = camera lens (derived from a figure, already published by the author [65]).

The light emitted by SLDs is no laser light, since SLDs lack a resonator, and hence no amplified stimulated emission of light can occur.

The SLD used in this work (Superlum, SLD-371-HP2-DBUT-SM-PD), has a central wavelength of 841 nm and a spectral bandwidth of 49.6 nm. It is fiber pigtailed, which means the light emitted by the SLD is coupled directly into a single mode fiber. To prevent the light source from any damage due to backreflected light from the interferometer, an optical isolator (OI, Thorlabs Germany, IO-F-SLD100-840APC) is placed between the SLD and the first fiber collimator (FC1, see Fig. 4.1). A description of how an OI blocks the back-reflected light by rotating the polarization of the light can be found in [21].

Even though the OI should be polarization independent, this is not the case in reality. Therefore, a polarization controller (PC) is added before the OI to maximize the power of the light passing through the optical isolator. The PC (Thorlabs, FPC030) uses stress induced birefringence to change the polarization of the light that is propagated through the single mode fiber in the PC. This is done by looping the fiber into the three manually tiltable spools, which creates three fractional fiber retarders. The birefringence is dependent on the fiber cladding diameter, the loop diameter, the number of loops per spool and the wavelength of the light propagating through the fiber. The fast axis of the fiber lies in the plane of the spool, and can thus be aligned with respect to the transmitted polarization vector. With the first and the third spool acting as quarter wave plates and the middle spool acting as half wave plate[ii], complete control of the output polarization is possible. The three spools are manipulated until the power of the light exiting the OI is at maximum.

The fiber leaving the OI is connected to the first fiber collimator (FC1, Te Lintelo Systems BV, HPUCO-23-840-S-6.2AS), which collimates the SLD's light and guides it to the Michelson interferometer. The $1/e^2$-diameter DA of the collimated gaussian beam can be calculated as follows:

$$DA = 2f \cdot NA. \tag{4.1}$$

f represents the focal length of the collimator lens, and NA stands for the numerical aperture of the fiber attached to the collimator. For $f = 6.2\,\text{mm}$ and $NA = 0.096$, equation (4.1) yields a beam diameter of 1.2 mm that enters the interferometer.

4.1.2 Interferometer

The Michelson interferometer of the experimental setup (see Fig. 4.1) is, in principle, the same as in section 3.1, but for some additional optical elements in reference and sample arm.

Reference arm

Since there was not sufficient space for a straight setup, the reference arm has a 90° bend. The reference mirror (M3) is mounted on a translation stage, so that the reference arm length can be matched to the length of the sample arm. To compensate for the dispersion due to the lenses and the rat eye in the sample arm, a dispersion compensation (DC) in form of a glass block is in the reference arm. The refractive index (or rather the material) and the thickness of the glass block have to be chosen in such a way that its optical length equals the optical length of all dispersive media in the sample arm (all lenses and the ocular media). Furthermore, a neutral density filter (NDF) is used to attenuate the reference beam, so as not

---

[ii] The first and the third spool contain one fiber loop, respectively, while the spool in the middle contains two fiber loops.

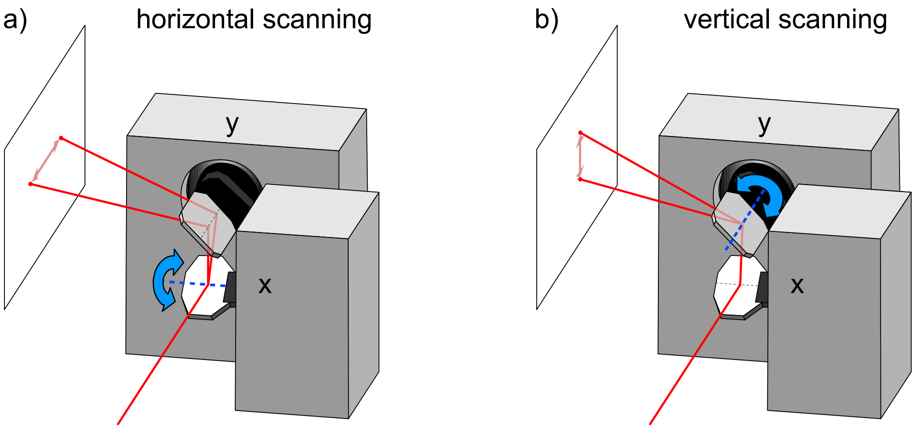

Figure 4.2: Schematic drawing of the galvo-scanner, showing horizontal scanning by turning the x-scanner as well as vertical scanning by turning the y-scanner (adapted from [21]).

to overdrive the camera. Since the reflectivity of the sample is usually much lower than the reference reflectivity, there is no need for an NDF in the sample arm.

Sample arm

The sample arm includes a galvo-scanner (shown in Fig. 4.1 as *fast scanning mirror* and as *slow scanning mirror*), a lens system and the sample, e.g. the rat eye.

The galvo-scanner consists of two galvanometer motors (Galvoline, G1222HS), with a mirror that is optimized for infrared light attached to each of their rotors. The two scanning mirrors are mounted orthogonal to each other, as shown in Fig. 4.2. Since, the sample beam is deflected by both scanning mirrors, it is moved over the sample horizontally by turning the x-scanner (see Fig. 4.2(a)), or vertically by turning the y-scanner (see Fig. 4.2(b)). To acquire a cross-sectional image (a B-scan consisting of several adjacent A-scans), the x-scanner is turned in one direction, while the y-scanner remains static[iii]. 3D data-sets can be recorded by turning the y-scanner slightly in one direction after each recorded B-scan, therefore it is also referred to as slow axis scanner. The movement of the fast axis scanner can induce unwanted Doppler shifts in the sample beam that will overlay the desired Doppler shifts of the moving sample particles. This can be avoided by directing the sample beam exactly onto the pivot point of the fast scanning mirror (as indicated in Fig. 4.2 by the dashed lines).

To actually scan the sample beam over the retina of the rat eye, the pivot point of the tilting beam has to be in the pupil of the eye, or else the beam can only pass the

---

[iii] The x-scanner is not necessarily the fast axis scanner. In the case of vertical scanning, the y-scanner performs the fast movement, while the x-scanner remains static.

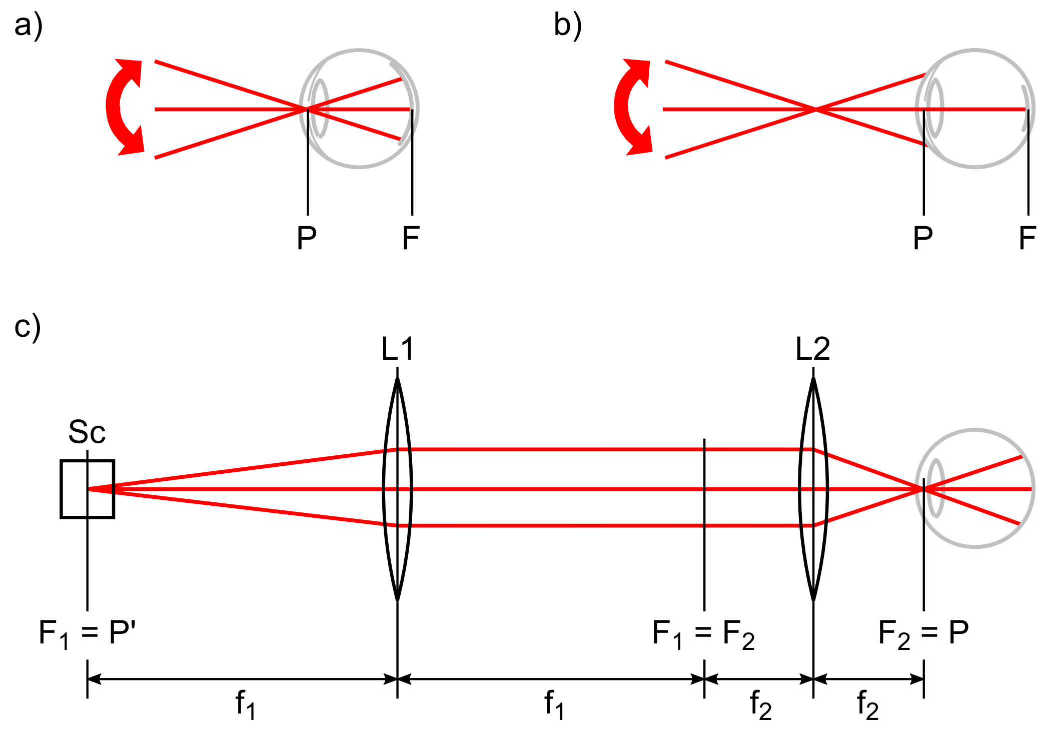

Figure 4.3: (a) Scanning sample beam pivoting at the pupil plane of the eye; (b) sample beam pivoting before pupil plane, thus the beam can only pass the pupil at central scanning positions; (c) sketch of the scanner in the second pupil plane P' that coincides with the focal plane F_1 of L1, the lens system, and the scanning sample beam (adapted from [21]).

pupil in central scanner positions, as shown in Fig. 4.3(a),(b). The necessary setup is achieved by placing the fast scanning mirror in the focal point of the first lens L1, as illustrated in Fig. 4.3(c). Another purpose of the lens system is the reduction of the sample beam's diameter, as the rat eye's fully dilated pupil has a diameter of about 2 mm at most. Even though the central sample beam fits through the dilated pupil, as it has a diameter of 1.2 mm, this may not be the case if scanning is performed, since the pivot point of the scanning beam will most likely be not exactly in the pupil plane, in reality. Therefore the beam entering the eye should have a diameter in the range of 0.3 mm. The lens system consists of two achromatic lenses (see Fig. 4.1). The lens L2 is also part of the RVA, and can therefore not be chosen arbitrarily. It has a focal length of $f_2 = 19.7\,\mathrm{mm}$ and is mounted at a fixed position. As shown in Fig. 4.3(c), the focal point of L2 should coincide with the pupil plane of the rat eye, thus, f_2 determines the distance between eye and L2. Using the magnification relation for two biconvex lenses

$$DA_{\mathrm{sample}} = \frac{f_2}{f_1} \cdot DA, \tag{4.2}$$

together with $DA = 1.2\,\mathrm{mm}$, the beam diameter after the lens system $DA_{\mathrm{sample}} = 0.3\,\mathrm{mm}$ and $f_2 = 19.7\,\mathrm{mm}$, yields the focal length $f_1 = 78.8\,\mathrm{mm}$. Consequently a lens with the focal length of $f_1 = 75\,\mathrm{mm}$ was chosen for L1. Thus, the actual beam diameter entering the eye can be calculated to be $DA_{\mathrm{sample}} \approx 0.315\,\mathrm{mm}$. L1 is mounted on a translation stage, which allows focusing the beam onto the sample to compensate for the eye being not exactly at the focal point F_2, as well as for varying eye lengths.

4.1.3 Integration of the DVA in the setup

The measurement of blood flow changes in a retinal vessel requires the knowledge of the blood flow velocity as well as the vessel's diameter, since the blood flow Q is calculated by the following relation:

$$Q = v \cdot A = v \cdot \frac{D^2\pi}{4}, \tag{4.3}$$

where v represents the velocity, A stands for the vessel's cross-sectional area and D for the vessel diameter. As already mentioned in section 2.5.10, Doppler OCT is not only capable of measuring the velocity of blood inside a vessel, but also of determining the vessel's diameter. However, the assessment of vessel diameters from OCT images has several limitations: the length in µm of one image pixel in depth direction is given by the image resolution, which is limited by the axial resolution of the OCT system (image resolution and axial resolution will be explained in section 4.1.5). Thus, the accuracy of the vessel diameter determination from OCT images is also limited by the axial resolution[iv]. Furthermore, the rear vessel wall is obscured as a result of absorption and multiple scattering of the sample beam by the red blood cells, which can result in an underestimation of the vessel diameter. If the phase tomograms are used to extract the vessel diameter, another problem, related to the parabolic flow-profile in the vessel arises. Since the parabolic flow profile equals zero at the vessel wall, and its maximum lies in the center of the blood vessel, the velocities decrease rapidly close to the vessel wall. If the velocities decrease so much that the OCT phase values are in the range of the system's phase noise, the red blood cells corresponding to these slow velocities cannot be distinguished from static tissue anymore, which results in underestimation of the vessel diameter [21, 46]. In the work at hand, the limitations of the vessel diameter determination via OCT were avoided by using an RVA (DVA rodent, Imedos, Jena, Germany)[v], which is coupled to the OCT system, to measure the vessel diameters; the same approach was followed in the human dual beam Doppler OCT system by Doblhoff-Dier [21, 46].

[iv] Using the transversal vessel diameter would be even less accurate than the axial diameter, since it is limited by the oversampling factor as well as the lateral resolution (see section 4.1.5).

[v] The fundus camera setup of an RVA and a dynamic vessel analyzer (DVA) is the same, but for the camera. The RVA uses a high resolution camera that can capture static fundus photos, from which the vessel diameters can be extracted. The DVA, on the other hand, uses a video camera, and its software is capable of tracking the vessels of interest during small eye movements, while continuously recording the vessel diameters.

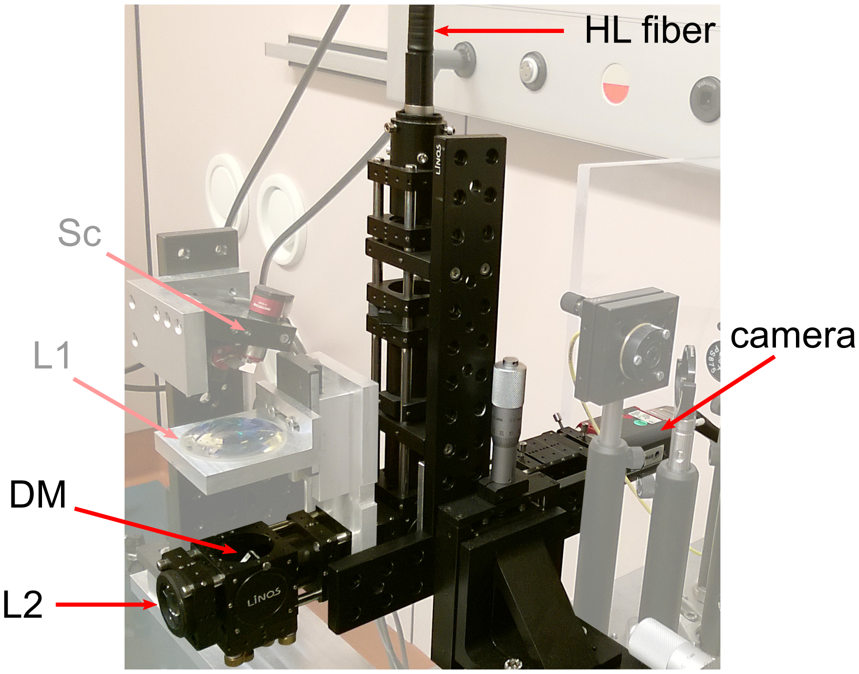

Figure 4.4: Experimental DVA rodent setup, showing the fiber to the halogen lamp (HL fiber), the video camera, the dichroic mirror (DM) and the ocular lens L2. Furthermore, the picture shows the scanner of the OCT system (Sc) and the first lens L1.

The DVA rodent consists of a fundus camera that is optimized for rats (see Fig. 4.4), and a computer with the retinal vessel analyzer software RVA4.16 by Imedos. The software was created for the assessment of human retinal vessel diameters, based on the Gullstrand eye model [66]. Since rat eyes and human eyes have different sizes and refraction powers (see section 2.3), the imaging path as well as the magnification of the RVA differs from the human system, which has to be considered when using the RVA4.16 software. The DVA rodent system is capable of continuous vessel diameter measurements of retinal vessels with excellent reproducibility. Furthermore, it has a higher magnification than the human system, which gives, in combination with the complex algorithms for vessel boundary detection, a measurement resolution of up to 0.1 µm. Therefore, vessel diameters as low as 30 µm can be measured in albino as well as in pigmented rats [65].

The OCT system and the RVA are coupled by a dichroic mirror (DM, hot mirror 45°, Edmund Optics, 64-468), as shown in Fig. 4.5. The DM is positioned between the hole mirror (HM) and the ophthalmic lens L2. More than 85 % of the visible light used by the RVA is transmitted through the DM, while more than 95 % of the OCT system's sample beam, which is in the near infrared range of light, is reflected by the DM. This coupling of OCT and RVA via a DM, along with the fact that the video camera of the DVA rodent is equipped with an infrared filter, enables simultaneous OCT and vessel diameter measurements.

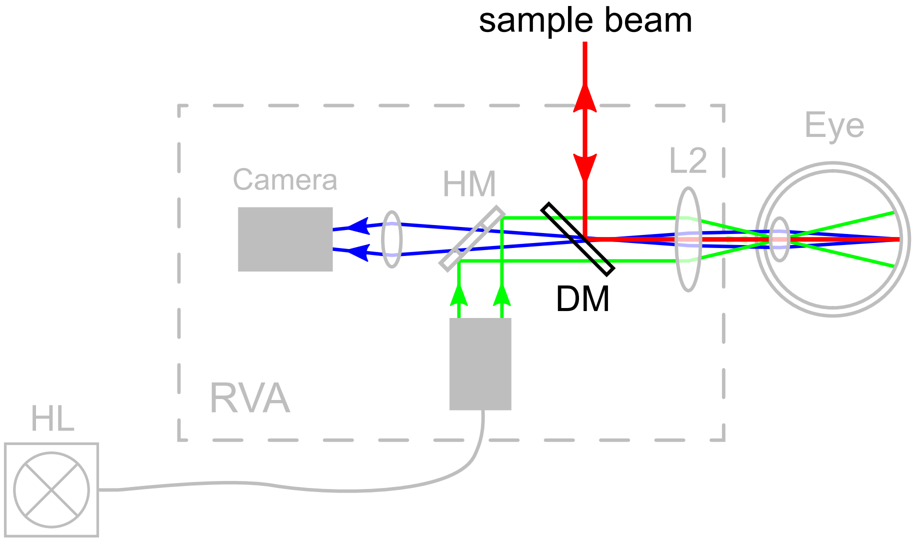

Figure 4.5: Schematic drawing of the RVA. The visible light that is used by the RVA passes through the dichroic mirror (DM), while the infrared light of the OCT sample beam is reflected.

4.1.4 Spectrometer

In FDOCT, the interference beam from the reference and sample arm is measured by a spectrometer before the intensity function is Fourier transformed, as already mentioned in section 3.3. A photograph showing the spectrometer and its components can be found in Fig. 4.6. The interference beam from the OCT system's interferometer enters the spectrometer via a fiber collimator (FC3, Te Lintelo Systems BV, HPUCO-23-800/1000-S-100AC-SP), and is then directed onto a diffraction grating (DG, Wasatch Photonics, 1200 lines/mm at 830 nm). The light is diffracted by the grating according to its wavelength components and then focused onto the CCD camera (Atmel, AViiVA M2 CL 2014) by an achromatic camera lens (CL, Thorlabs, AC508-100-B).

The diffracted light beams emerging from the grating lines interfere with each other and form an intensity distribution. The maxima of this distribution are given by the grating equation

$$m\lambda = g \cdot (\sin\phi \pm \sin\psi_m)\,, \tag{4.4}$$

where $m = 0, 1, 2, ...$ stands for the order of the interference maxima, λ denotes the wavelength of the incident light, g represents the grating constant (the distance between two grating lines), ϕ is the angle of the incident light beam and ψ_m is the angle of diffraction. Both angles are measured from the grating normal, as shown in Fig. 4.7, along with the other parameters of Eq. (4.4).

The first order of diffraction is commonly used for spectrometers in OCT systems. Consequently, the angle of diffraction ψ_1 of the first order of diffraction can be

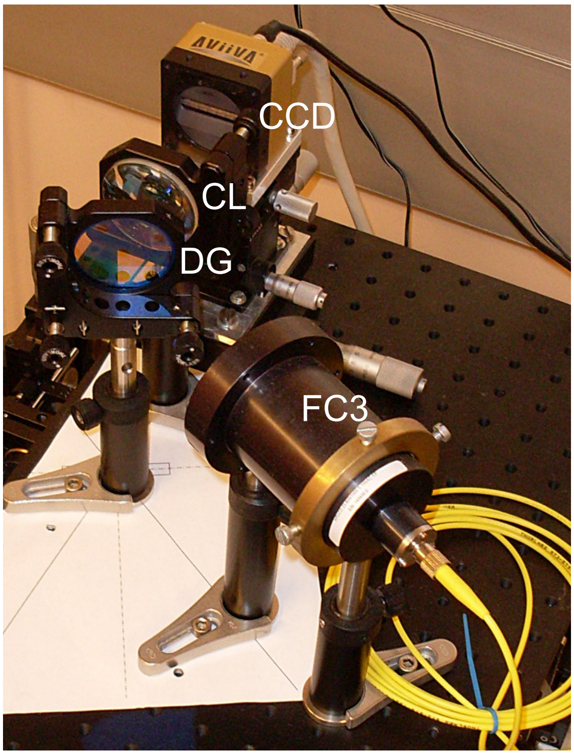
CCD
CL
DG
FC3

Figure 4.6: Photograph of the spectrometer used in the single beam OCT system in the work at hand. FC = fiber collimator, DG = diffraction grating, CL = camera lens, CCD = charge-coupled device (line camera).

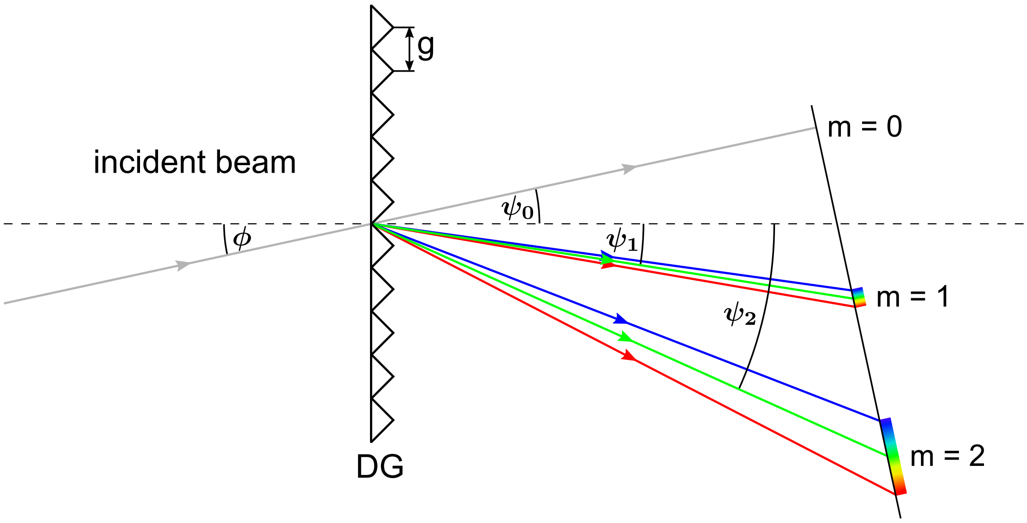
g
incident beam
m = 0
ψ_0
ϕ
ψ_1
m = 1
ψ_2
m = 2
DG

Figure 4.7: Illustration of an incident light beam being dispersed by a diffraction grating (DG) (adapted from [21]).

calculated from Eq. (4.4):

$$\psi_1 = \arcsin\left(\frac{\lambda}{g} - \sin\phi\right). \tag{4.5}$$

Inserting the central wavelength of the SLD (841 nm), the grating constant $g = \frac{1}{1200}$ mm (as the grating has 1200 lines/mm), along with the angle of the incident beam $\phi = 30°$, into Eq. (4.5), yields the angle of diffraction $\psi_1 = 30.6°$. The camera lens and the CCD were placed so that their surface normals are parallel to the beams diffracted by ψ_1.

Before performing any post-processing steps (e.g. the Fourier transformation described in section 3.3.1) after recording the OCT spectra, one needs to know the relation between the wavelength λ_x of the diffracted light and the corresponding position x on the CCD array of the camera. The derivation of this relation can be found in Park et al. [67] and Doblhoff-Dier [21] and will also be described in the following.

As shown in Fig. 4.8, the incident light of the central wavelength λ_c is diffracted by the angle ψ_c, following Eq. (4.4). The spectrometer is adjusted in such a way that diffracted light with the wavelength λ_c is focused onto the center of the CCD array. The green beams in Fig. 4.8 indicate the light with the wavelength λ_c. Therefore, analogous to Eq. (4.4) and Eq. (4.5), it can be written:

$$\begin{aligned} \lambda_c &= g \cdot (\sin\phi + \sin\psi_c) \\ \psi_c &= \arcsin\left(\frac{\lambda_c}{g} - \sin\phi\right). \end{aligned} \tag{4.6}$$

This relation can also be formulated for light beams of other wavelengths λ_x, represented by the red beams in Fig. 4.8, and their corresponding angles of diffraction ψ_x:

$$\lambda_x = g \cdot (\sin\phi + \sin\psi_x). \tag{4.7}$$

Depending on ψ_x, these light beams are focused onto the CCD array at different positions with distances x to the center of the CCD array. Fig. 4.8 shows that the relation between the angle of diffraction and the distance x can be described by the following equation:

$$\begin{aligned} \tan(\Delta\psi) = \tan(\psi_x - \psi_c) &= \frac{x}{f} \\ \psi_x = \psi_c + \arctan&\left(\frac{x}{f}\right), \end{aligned} \tag{4.8}$$

where f represents the focal length of CL, as well as the distance between camera and CL. Inserting ψ_x from Eq. (4.8) into Eq. (4.7) results in

$$\lambda_x = g \cdot \left(\sin\phi + \sin\left[\psi_c + \arctan\left(\frac{x}{f}\right)\right]\right). \tag{4.9}$$

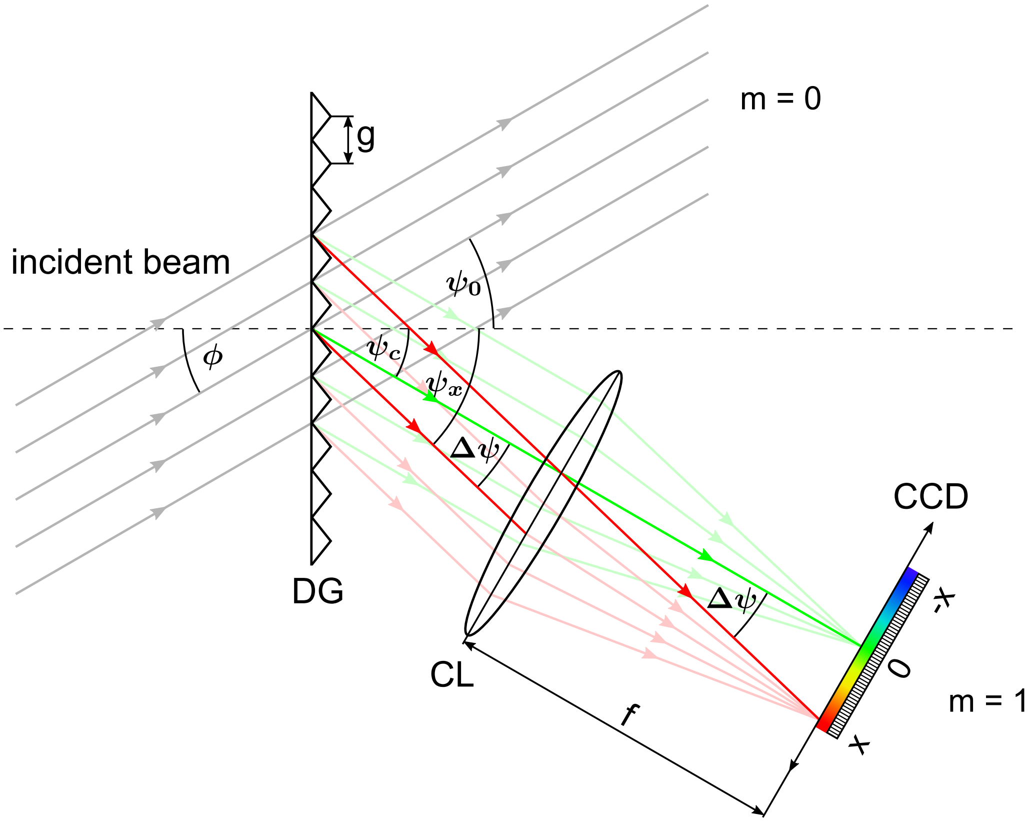

Figure 4.8: Schematic drawing of the spectrometer (adapted from [40] and [21]).

As can be seen in Eq. (4.9), the relation between λ_x and x is non-linear, i.e. the wavelength distribution that is imaged on the CCD array of the line camera is not entirely equidistant. Therefore a linear approximation of this relation (see section A.2) is used for the post-processing of the data. The deviation of the linear approximation from the exact relation is very small and can be compensated in the rescaling, which will be described in section A.2.

4.1.5 System parameters

In this section, the most important system parameters of the single beam OCT setup will be described.

Image resolution

FDOCT measures the path length differences Δz between the interferometer's sample and reference arm via the oscillation frequencies of the detected interference signal (see section 3.3). The detected signal is proportional to the cosine of the path

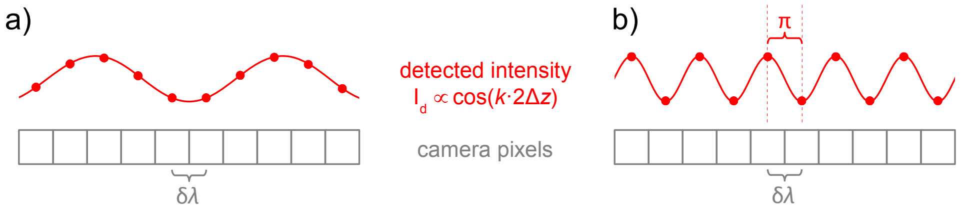

Figure 4.9: Interference intensity signal I_D recorded by the spectrometer's line camera. a) shows an I_D corresponding to an arbitrarily chosen Δz, while b) illustrates the I_D of the maximum recordable path length difference Δz_{max} [21].

length difference (cf. Eq. (3.1) and Eq. (3.32)):

$$I_D \propto \cos(2k\Delta z), \tag{4.10}$$

which yields higher oscillation frequencies of I_D for larger path length differences Δz. The maximum frequency and thus the largest Δz the line camera of the OCT system can detect, is limited by the pixel size of the camera's CCD array. The highest frequency that will not just yet be undersampled is reached if half the oscillation's wavelength coincides with the distance between two adjacent CCD pixels as illustrated in Fig. 4.9; higher frequencies would be undesampled. Knowing this, it can be seen from Eq. (4.10) that the largest path length difference Δz_{max} (or the highest frequency) that can be recorded by the OCT system's line camera is defined by the smallest detectable wave vector δk:

$$2 \cdot \delta k \cdot \Delta z_{\text{max}} = \pi. \tag{4.11}$$

δk can be calculated by differentiating the relation $k = \frac{2\pi}{\lambda}$:

$$\begin{aligned} \delta k &= -2\pi \frac{\delta\lambda}{\lambda_0^2} \\ |\delta k| &= 2\pi \frac{\delta\lambda}{\lambda_0^2}, \end{aligned} \tag{4.12}$$

where $\delta\lambda$ represents the smallest detectable wavelength difference and λ_0 stands for the central wavelength of the systems light source. After inserting Eq. (4.12) in Eq. (4.11), one arrives at the same relation as Lee et al. [68]:

$$\Delta z_{\text{max}} = \frac{\pi}{2 \cdot \delta k} = \frac{\lambda_0^2}{4 \cdot \delta\lambda}. \tag{4.13}$$

Since OCT measurements are usually performed in a medium and the speed of light in a medium is reduced by the factor $\frac{1}{n}$, where n represents the medium's refractive index (cf. (3.72)), Eq. (4.13) has to be changed into:

$$\Delta z_{\text{max}}^{\text{medium}} = \frac{\lambda_0^2}{4 \cdot n \cdot \delta\lambda}. \tag{4.14}$$

In order to calculate the wavelength difference $\delta\lambda$ between two pixels, one needs to know the range of wavelengths $\Delta\lambda = \lambda_{\text{max}} - \lambda_{\text{min}}$ focused on the CCD array, as well as the number of CCD pixels $N_{\text{CCD-pixel}}$:

$$\delta\lambda = \frac{\lambda_{\text{max}} - \lambda_{\text{min}}}{N_{\text{CCD-pixel}}}. \tag{4.15}$$

The line camera of the OCT setup has 2048 pixels. The maximum wavelength that can be recorded by the system's spectrometer can be calculated using Eq. (4.9), as done in section A.2.1, which yields $\lambda_{\text{max}} = 938.39\,\text{nm}$. The minimum wavelength $\lambda_{\text{min}} = 734.76\,\text{nm}$ can be calculated analogously, with the difference that one has to insert the negative half of the CCD array's length (see Fig. 4.8) $x_{\text{min}} = -14.34\,\text{mm}$. Thus, Eq. (4.15) yields $\delta\lambda = 0.0994\,\text{nm}$.

Inserting $\delta\lambda$, the central wavelength of the system $\lambda_0 = 841\,\text{nm}$ and the refractive index for blood $n = 1.37$ into Eq. (4.14) gives the maximal depth range in blood that can be recorded by the OCT system: $\Delta z_{\text{max}}^{\text{blood}} = 1.3\,\text{mm}$.

Dividing the maximum depth range by the number of pixels contained in an A-scan gives the correspondence between A-scan pixels and µm in axial sample beam direction. Since the Fourier transform is symmetric around zero and thus only half of the CCD array's pixels, i.e. in this case 1024, are used, the correspondence between A-scan pixels and actual distance, which is also known as the *image resolution*, results in:

$$1\,\text{px} \mathrel{\widehat{=}} 1.27\,\mu\text{m}. \tag{4.16}$$

It should be mentioned that the image resolution in axial beam direction is limited by the physical axial resolution, which will be explained in the following.

Axial resolution

Using OCT, it is possible to achieve high axial resolutions independently of beam focusing and spot size of the focused beam, i.e. in OCT lateral and axial resolution are decoupled, in contrast to e.g. standard microscopy.

The axial resolution of an OCT system is given by half of the the light source's coherence length. The factor $\frac{1}{2}$ comes from the double pass of the light through the interferometer arms.

Since the light source of the OCT system, used in the course of this work, has a Gaussian shaped spectrum, the axial resolution δz is calculated from the Gaussian coherence length $l_{c,Gauss}$ (see Eq. (3.12)):

$$\delta z = \frac{l_{c,Gauss}}{2} = \frac{2\ln 2}{\pi}\frac{\lambda_0^2}{\Delta\lambda}. \tag{4.17}$$

Inserting the central wavelength $\lambda_0 = 841\,\mathrm{nm}$ and the bandwidth $\Delta\lambda = 49.6\,\mathrm{nm}$ of the SLD into Eq. (4.17), yields the OCT system's axial resolution $\delta z = 6.3\,\mu\mathrm{m}$.

As can be seen in Eq. (4.17), the axial resolution of an OCT application depends only on the central wavelength and on the bandwidth of the light source. Therefore, broad band light sources are needed in order to achieve high axial resolutions.

It should be mentioned that the axial resolution improves further for optical media with refraction indices $n > 1$, due to the fact that

$$\delta z_{\mathrm{med}} = \frac{\delta z}{n}. \tag{4.18}$$

In case of a blood vessel, the refractive index of blood $n_{\mathrm{blood}} = 1.37$ has to be inserted into Eq. (4.18), which yields the axial resolution in blood $\delta z_{\mathrm{blood}} = 4.6\,\mu\mathrm{m}$.

Lateral resolution

The radius of a Gaussian beam $w(z)$ is defined as the distance from the beam's center to the point at which the beam intensity drops to $\frac{1}{e^2}$ of its maximum (see the red curves in Fig. 4.10). The spot size of the focused beam of an OCT system defines the lateral resolution δx, which is two times the beam's waist radius w_0, in the case of a Gaussian beam (see Fig. 4.10). Thus, together with the beam divergence $\theta = \frac{\lambda_0}{\pi w_0}$ [69], one arrives at:

$$\delta x = 2w_0 = \frac{2\lambda_0}{\pi\theta}. \tag{4.19}$$

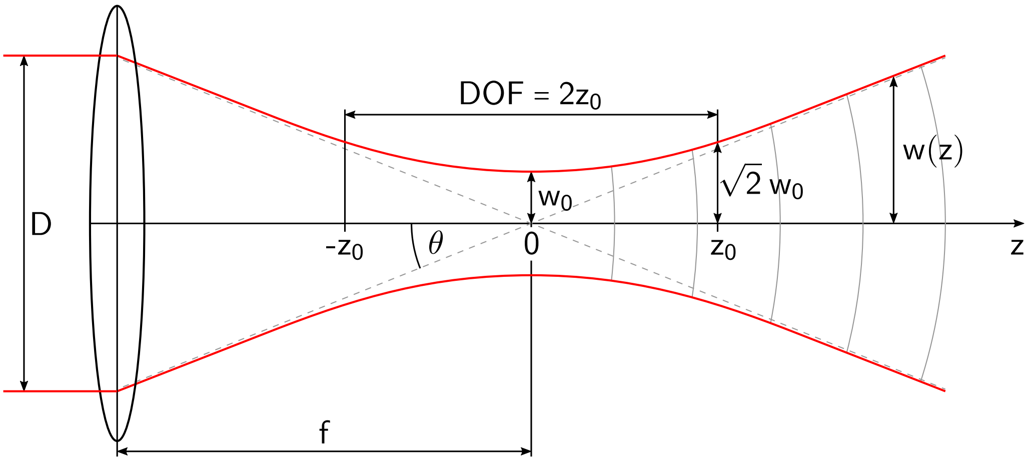

Figure 4.10: Schematic drawing of a collimated Gaussian beam being focused by a lens, with the following parameters: the incident beam's diameter D, the focal length of the lens f, the beam divergence θ, the beam radius $w(z)$ at a distance z from the focus point, the Rayleigh length z_0 and the radius of the beam's waist w_0.

For a Gaussian beam that is focused by a lens, one can write $\tan\theta = \frac{D}{2f}$, as can be seen in Fig. 4.10, where D is the beam diameter before the lens and f is the focal length of the lens. $\theta \approx \frac{D}{2f}$ in case of small beam divergence angles: thus, the lateral resolution can be rewritten to:

$$\delta x = \frac{4\lambda_0 f}{\pi D}. \tag{4.20}$$

With $f = \frac{1}{300}\,\mathrm{m}$ (since the total refraction power of the rat eye equals 300 dpt [22]) and $D = DA_{\text{sample}} = 0.32\,\mathrm{mm}$ (see section 4.1.2), the lateral resolution of the OCT system in the rat eye results in $\delta x = 11.3\,\mu\mathrm{m}$.

Depth of focus

The depth of focus (DOF) is defined as twice the Rayleigh length

$$z_0 = \frac{k}{2} \cdot \omega_0^2 = \frac{\pi \omega_0^2}{\lambda_0}. \tag{4.21}$$

As can be seen in Fig. 4.10, z_0 is the distance in which the Gaussian beam widens from w_0 to $\sqrt{2}w_0$. Using Eq.(4.21) together with Eq. (4.19), one can calculate the DOF to be:

$$\mathrm{DOF} = 2 \cdot z_0 = \frac{2\pi \cdot \omega_0^2}{\lambda_0} = \frac{2\pi \cdot \left(\frac{\delta x}{2}\right)^2}{\lambda_0} = \frac{\pi \cdot \delta x^2}{2\lambda_0} \tag{4.22}$$

Inserting the lateral resolution of $\delta x = 11.3\,\mu\mathrm{m}$ and the setup's central wavelength gives a DOF of 238.5 µm. This is sufficient for the measurement of retinal vessels in the rat eye, as the rat retina has a thickness of about 170 µm [22].

Oversampling factor

The measurement of a sample particle's velocity using the Doppler OCT technique, which is described in section 3.4.1, is based on the assumption that two adjacent A-scans are taken at the exact same position at different times. However, as mentioned in section 4.1.2, to acquire a cross-sectional image (also known as B-scan), the probe beam has to be scanned across the sample continuously, i.e. the adjacent A-scans are not recorded exactly at the same position. Too large distances between two adjacent A-scan positions will result in decorrelation of the two A-scan signals. The further the adjacent A-scans are apart, the stronger the decorrelation noise (random phase variations) will get, until it completely overlays the phase differences that are induced by moving sample particles. Hence, when performing Doppler FDOCT measurements, it is necessary to use a sufficient degree of oversampling [9]. However, high oversampling prolongs the data acquisition time of the measurements, thus making them more susceptible to sample motions. Therefore, one has to find a reasonable compromise between signal decorrelation and measurement time.

A definition for the degree of oversampling of a phase tomogram was introduced by Singh et al. [70], in form of the oversampling factor (OF):

$$\mathrm{OF} = \frac{\delta x \cdot N}{d}, \tag{4.23}$$

with δx being the spot size (or the lateral resolution), N being the number of sample points and d being the geometrical width of the tomogram. Inserting the system's lateral resolution $\delta x = 11.3\,\mu\mathrm{m}$, as well as the number of A-scans $N = 1000$ and the tomogram width $d = 1.1\,\mathrm{mm}$, which were used in all measurements conducted in section 4.4, into Eq. (4.23) yields an oversampling factor of $\mathrm{OF} \approx 10$.

This value indicates that the distance between the sampling points of two adjacent A-scans is $\frac{1}{10}$ of the sample beam's spot size. The standard deviation of the phase values that are obtained at this sampling point distance and beam diameter ratio is below 0.35 rad according to Park et al. [67], which is sufficiently low to be disregarded.

Velocity range of the OCT system

The single beam system's maximum velocity v_{max} without any phase wrapping artifacts can be calculated by inserting $\Delta\phi_{\mathrm{max}} = \pi$ into Eq. (3.74). With the other parameters, namely the Doppler angle $\delta = 0°$, the system's central wavelength $\lambda_0 = 841\,\mathrm{nm}$, the refractive index of blood $n_{\mathrm{blood}} = 1.37$ and the CCD camera's exposure time $\tau_{\mathrm{min}} = 57\,\mu\mathrm{s}$, Eq. (3.74) yields $v_{\mathrm{max}} = 2.7\,\mathrm{mm/s}$. However, since the in-vivo measurements were performed in the posterior pole of the rat eyes about one optic disk diameter from the ONH, much higher Doppler angles in the range of 90° were most likely. Thus, the real v_{max} was in the range of 15 mm to 25 mm, depending on the Doppler angle. It is possible to assess even higher velocities by unwrapping the phase data (see section 4.3.2, blood vessel evaluation), in case of single phase wrapping. Multiple phase wrapping cannot be compensated as easily, since the exact number of phase wraps needs to be determined.

The lowest velocity v_{min} the OCT setup can detect is defined by the system's phase noise[vi] $\Delta\phi_{\mathrm{err}}$. The phase noise of a single B-scan $\Delta\phi_{\mathrm{err}} = 0.55\,\mathrm{rad}$ was determined by measuring a static retinal tissue region and taking the FWHM of this region's phase distribution, as suggested by Schmoll et al. [72]. However, since the phase data of 140 B-scans were averaged for every flow measurement conducted in the sections 4.2 and 4.4, the phase noise was also calculated for 140 averaged B-scans, which yielded $\Delta\phi_{\mathrm{err}}^{\mathrm{avg}} = 0.18\,\mathrm{rad}$. Inserting $\Delta\phi_{\mathrm{err}}^{\mathrm{avg}}$ and the parameters described in the previous paragraph into Eq. (3.74) yields a minimum detectable velocity as low as $v_{\mathrm{min}} = 1.8\,\mathrm{mm/s}$, for a Doppler angle of $\delta = 85°$. This Doppler angle was used for the capillary measurements described in section 4.2.2; smaller δ will, of course, result in lower v_{min}.

[vi] $\Delta\phi_{\mathrm{err}}$ of the measured data is composed of the noise coming from the CCD camera (fixed pattern and pixel noise; see Werkmeister [40] and Leitgeb et al. [71] for more details), phase deviations arising from the scanning process (in reality, the sample beam will never be adjusted perfectly on the pivot-point of the fast axis scanner), and phase deviations due to sample movements.

4.2 In vitro measurements

Before the previously described single beam OCT system was used to measure living animals, its functionality had to be tested by conducting ex vivo experiments.

4.2.1 Rotating disk

The first experiment to verify the system's capability of measuring relative velocities simply was a tilted rotating cardboard disk (see Fig. 4.11). Since the sample beam exits the OCT setup as collimated beam, an additional lens needs to be placed after the RVA lens to focus the sample beam onto the rotating disk. No scanning was performed during the measurement and the sample beam was focused on a position with a distance of $r = 5\,\mathrm{mm}$ from the disk's center. As mentioned in section 3.4.2, Doppler OCT can only measure the longitudinal velocity component of a moving sample. Consequently, the measured velocity equals zero for Doppler angles $\delta = 90°$. Hence, the cardboard disk has to be tilted, so that $\delta \neq 0°$, as shown in Fig. 4.11 b). Thus, the OCT system measures the longitudinal component $v_{\mathrm{disk,L}}$ of the tangential velocity v_{disk} at the focus point.

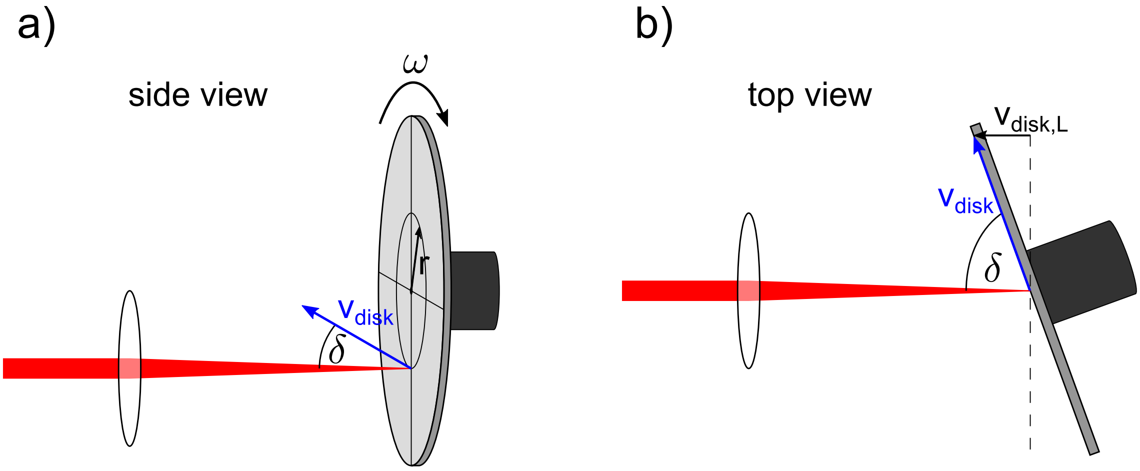

Figure 4.11: Schematic of the sample beam being focused on a disk rotating with the angular velocity ω to measure the tangential velocity v_{disk} at the illuminated position (adapted from [21]).

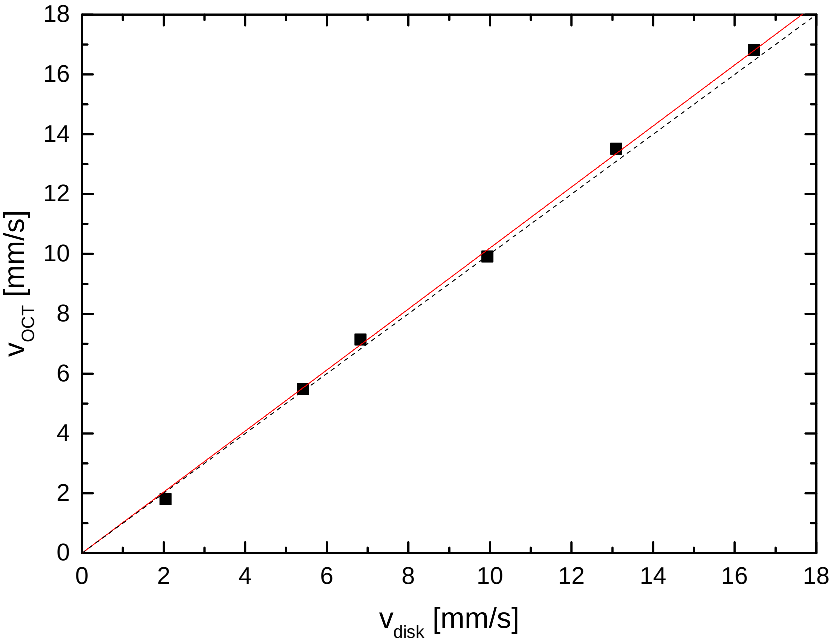

Figure 4.12: Linear relation between the tangential velocity of the rotating disk v_{disk} and the velocity calculated from the phase shift measured by the OCT system v_{OCT}. The red line represents the linear fit of the measured datapoints, and the dashed black line is the unity slope.

The rotational speed of the disk was regulated via the voltage applied to the disk's motor, and the number of rotations per second n_{rot} was determined by means of a stop watch. Since the angular velocity is defined as $\omega = 2\pi n_{\mathrm{rot}}$, the tangential velocity can be written as follows:

$$v_{\mathrm{disk}} = \omega \cdot r = 2\pi n_{\mathrm{rot}} \cdot r. \tag{4.24}$$

Due to the fact that the Doppler angle is known in this experiment, it is possible to calculate the disk velocities v_{OCT} from the phase values that are measured by the OCT system. In order to do so, Eq. (3.74) has to be used; however, n can be omitted, as the refraction index of air is one.

The results of six different disk velocities at a Doppler angle of $\delta = 81°$ are shown in Fig. 4.12. The phase values of several hundred A-scans were averaged for each datapoint. As can be seen in Fig. 4.12, the measured velocities v_{OCT} are in very good agreement with the set disk velocities v_{disk}, and their correlation is highly linear (the calculated correlation coefficient equals 0.99985).

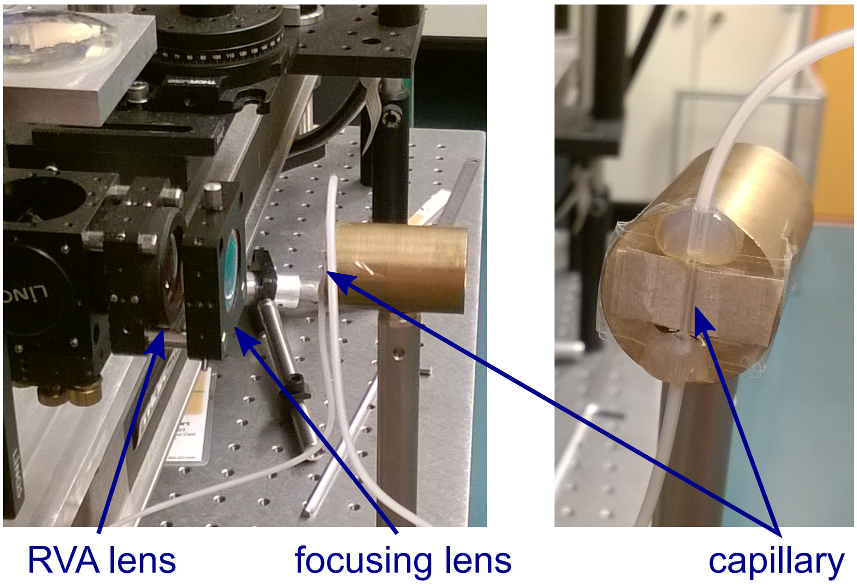

Figure 4.13: Photograph showing the RVA lens (L2 of the OCT system), the additional focusing lens and the glass capillary.

4.2.2 Glass capillary

The second experiment was designed to test the OCT system's capability to measure the velocity of a liquid flowing through a small glass tube, which is a simple in vitro simulation of a blood vessel in a living animal. The glass capillary has an inner diameter of 0.3 mm and is glued to the slanted end of a brazen tube, so that the Doppler angle between sample beam and capillary is not 90° (see Fig. 4.13). A sheet of paper is mounted behind the capillary, making it easier to find the right position of the reference mirror, as the paper gives a stronger structural OCT signal than the surface of the glass capillary. As already done in the experiment with the rotating disk (see section 4.2.1), an additional lens has to be mounted after the RVA lens to focus the sample beam onto the glass capillary.

Since the average red blood cell size of rats is about 7 µm [73], a dilution consisting of $\frac{1}{3}$ milk and $\frac{2}{3}$ water was used as sample liquid for the capillary measurements, as the fat globules in milk have diameters ranging from $0.1 - 15\,\mu\mathrm{m}$, with an average diameter of about 4 µm [74, 75]. As can be seen in Fig. 4.13, a flexible tube is attached to each end of the glass capillary. One of those flexible tubes is connected to a syringe, which is filled with the sample fluid and mounted in a syringe pump. Using this pump, one can apply a continuous flow and hence a constant velocity of the sample fluid in the capillary. To calculate the fluid's velocity in the capillary, the flow set at the syringe pump has to be divided by the capillary's cross-sectional area:

$$v_{\mathrm{cap.}} = \frac{Q_{\mathrm{pump}}}{A_{\mathrm{cap.}}} = \frac{Q_{\mathrm{pump}}}{r_{\mathrm{cap.}}^2 \pi}. \tag{4.25}$$

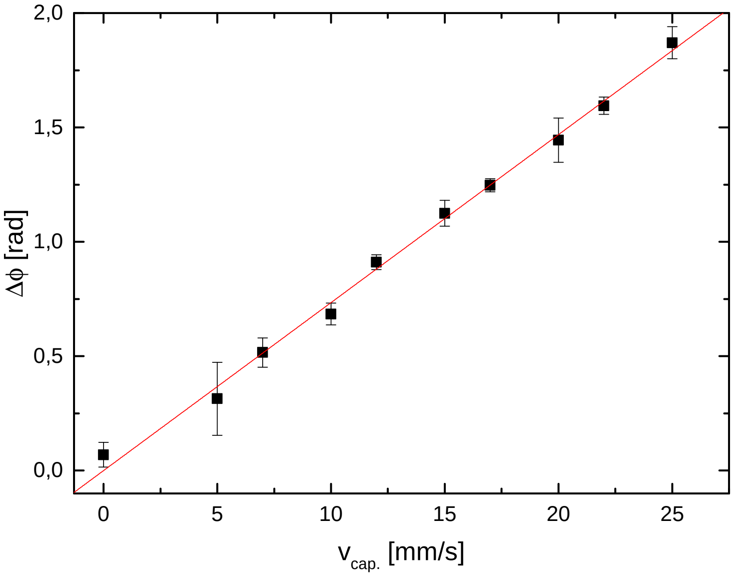

Figure 4.14: Mean phase difference values of three capillary measurements over the velocity in the capillary.

Using this relation, three measurement sets, each consisting of ten different velocities $v_{\text{cap.}}$ ranging from $0-25\,\text{mm/s}$, were conducted. After each flow change, ten minutes passed before an OCT measurement was recorded, to assure that the velocity in the capillary was constant, as the velocity may over, or under-shoot the set value shortly after starting the pump. To compensate for inconsistencies of the sample fluid's flow that are induced by the syringe pump, a single OCT measurement consists of 140 B-scans, which are averaged to calculate one datapoint.

The averaged results of the three measurement sets are shown in Fig. 4.14, which reveals that the phase difference values $\Delta\phi$ have a highly linear relation to the actual velocity $v_{\text{cap.}}$ inside the capillary (the correlation coefficient was calculated to be 0.99964).

This confirms the system's capability of measuring the relative velocity of a liquid[vii] in a glass capillary, and hence implies its capability of measuring the relative blood flow velocities of retinal vessels in living animals.

4.3 Data handling

All hardware control, data acquisition, data processing and data evaluation programs used in the course of this thesis were written in LabVIEW (National Instruments), the platform of the graphical programming language G.

[vii] The system can only measure velocities of liquids that contain sufficient particles, which reflect the light of the SLD (in case of this OCT system, light in the range of 841 nm).

4.3.1 Data acquisition

The waveforms for the galvo scanners and the camera trigger signals are generated in the LabVIEW program “3D-Scanner.vi”. The scanner waveforms are sent via the analog outputs of the acquisition board’s (NI PCIe-6251) connector block (BNC-2110), while the camera trigger signals are sent via the connector block’s digital outputs. A CCD line camera (Atmel, AViiVA M2 CL 2014) records the spectral data of the OCT system via a frame grabber board (NI PCIe-1430). The camera trigger signals are fed into the frame grabber board via an extension board (NI Camera Link I/O Extension Board).

Before starting the data acquisition software, the scanner control LabVIEW program needs to be started; as mentioned above, this program generates the scanner functions and the camera trigger signals. Fig. 4.15 shows the saw-tooth function for the motion the fast scanner performs during one B-scan, i.e. all A-scans that are contained in a single B-scan are recorded during the rising ramp of the fast axis scanner’s saw-tooth signal. Since B-scans consisting of 1000 A-scans were recorded for all measurements described in this chapter, and the camera’s exposure time was set to 57 µs, the fast scanner trigger frequency (also referred to as linerate or A-scan frequency) was set to 17.543 kHz. Although 1000 A-scans could thus have been recorded within 57 ms, the B-scan frequency (also known as framerate) was only set to 16 Hz, as the scanner needs sufficient time return to its starting position. Thus, a single saw-tooth motion performed by the fast axis scanner (see Fig. 4.15) took 62.5 ms.

The data acquisition program initializes the line camera and reserves two buffers with the size of a whole B-scan[viii], respectively. During the recording process, the

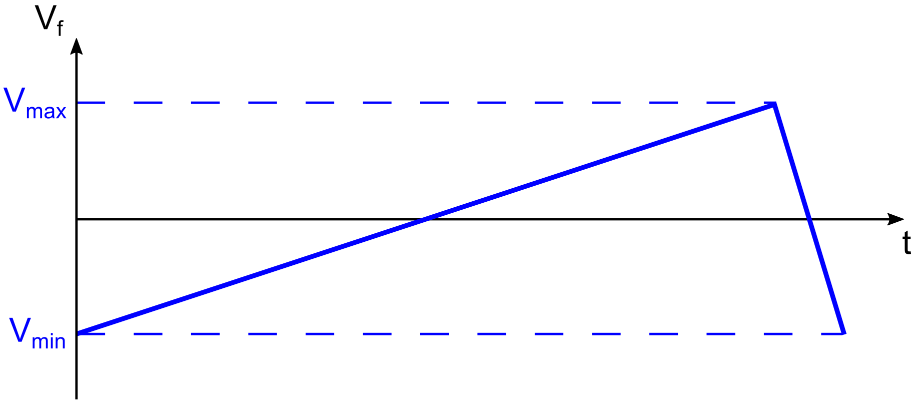

Figure 4.15: Saw-tooth function controlling the fast axis scanner. V_f is the voltage of the scanner’s control signal over time.

[viii] A B-scan consisting of 1000 A-scans is an image with 1000 pixels width and 2048 pixels height (as the CCD array has 2048 pixels). Hence, such a picture requires a buffer size of 3.9 megabyte for a pixel resolution of 16 bit.

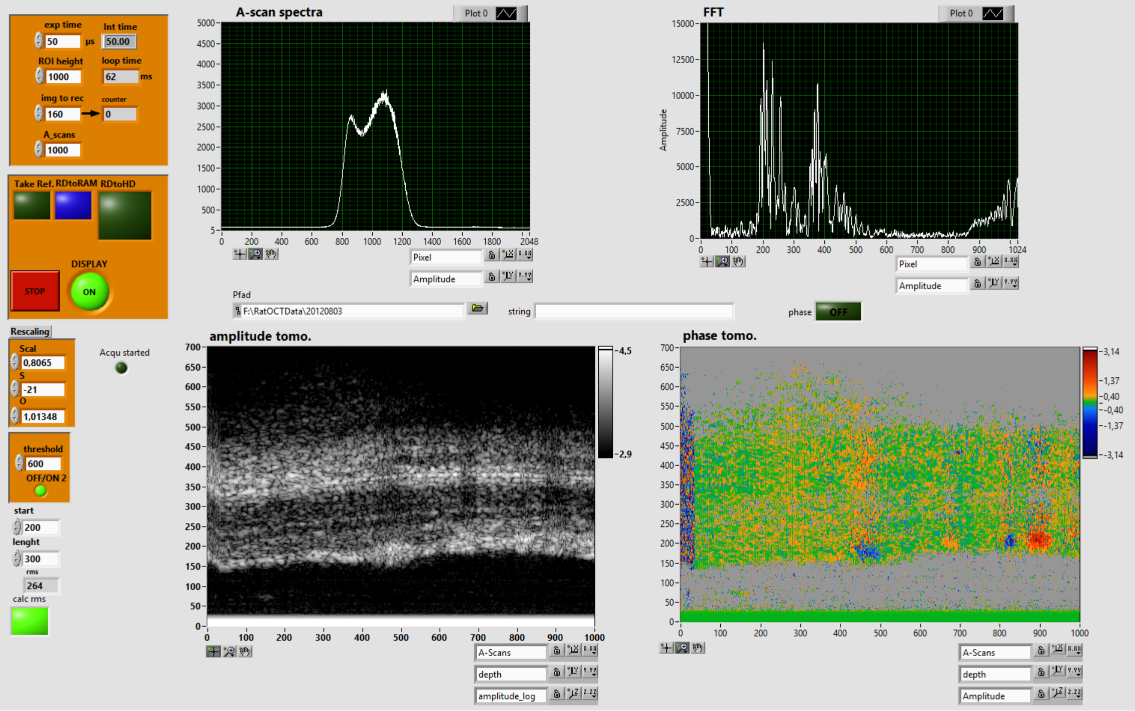
exp time 50 µs
Int time 50.00
ROI height 1000
loop time 62 ms
img to rec 160
counter 0
A_scans 1000
Scal 0,8065
S -21
O 1,01348
threshold 600
start 200
lenght 300
rms 264
Pfad F:\RatOCTData\20120803
phase OFF

Take Ref.
RDtoRAM
RDtoHD
DISPLAY
STOP
ON
Rescaling
OFF/ON 2
calc rms
Acqu started
A-scan spectra
Plot 0
5000
4500
4000
3500
3000
2500
2000
1500
1000
500
5
0
200
400
600
800
1000
1200
1400
1600
1800
2048
Pixel
Amplitude
FFT
15000
12500
10000
7500
5000
2500
Amplitude
100
300
500
700
900
1024
string
amplitude tomo.
700
650
600
550
500
450
400
350
300
250
200
150
100
50
-4,5
-2,9
A-Scans
depth
amplitude_log
phase tomo.
3,14
1,37
0,40
-0,40
-1,37
-3,14

Figure 4.16: Front panel of the data acquisition program showing the live images of an in vivo measurement of a rat retina.

camera writes adjacent B-scans alternatingly into buffer1 and buffer2. The data are written into buffer2, while the acquisition program reads the data from buffer1 and copies it to the system memory (copying the data directly to the hard disk drive (HDD) would be too slow); after 62.5 ms, the camera writes into buffer1 again and the acquisition program copies the data from buffer2 to the system memory. Once all B-scan data from one measurement are copied to the system memory, the data are saved as a 16-bit signed-integer binary file in the preset HDD folder. Storage on the HDD takes much longer than the actual acquisition time.

The data acquisition program has several live displays (see Fig. 4.16), which are needed for a successful OCT measurement. The first mathematical operation in the acquisition program's display section is the subtraction of a reference spectrum[ix] from every B-scan of the current measurement to remove unwanted system internal reflections. This step is not necessary to record OCT data; however, if no reference spectrum is recorded, the acquired spectra will not be corrected and the unwanted artifacts will stay visible in the live displays (see Fig. 4.17). Subsequently, every A-scan of the current B-scan is rescaled (see section A.2.2 for a description of the rescaling process), and the first of these rescaled A-scans is displayed on the program's front panel (see Fig. 4.16 upper left display). Then, the A-scan spectra are

---

[ix] A reference spectrum is recorded by blocking the sample arm right behind the RVA lens, and clicking the *Take Ref.* button in the data acquisition program. Thus, a full spectrum of one A-scan that includes all of the system's internal reflections, but no sample information, is recorded.

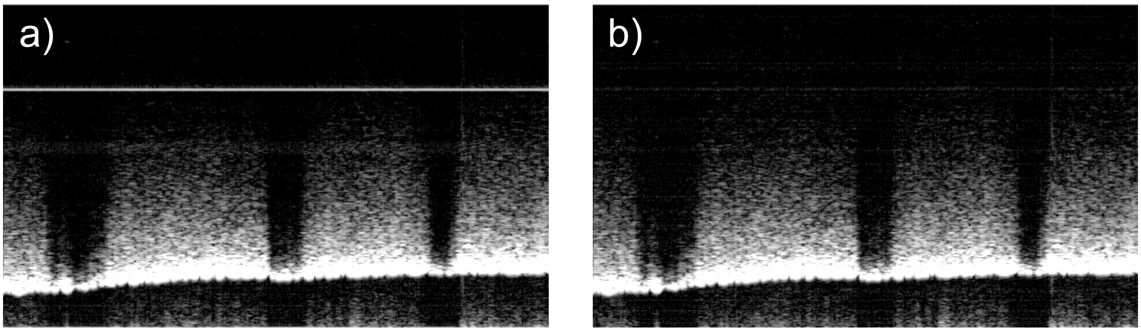

Figure 4.17: Amplitude image of an artificial eye[x]; in image a) an internal reflex of the OCT system can be seen as white line above the cross-sectional image of the artificial eye. Image b) shows the same B-scan after subtracting the reference spectrum from each A-scan.

Fourier transformed by a fast Fourier transform algorithm and shown on the front panel's second display (see Fig. 4.16 upper right display). Taking the amplitude of a B-scan's Fourier transform gives the intensity image, which is also displayed on the programs front panel (see Fig. 4.16 lower left display). The first line of the phase image is calculated by taking the phase difference between the B-scan's first and second A-scan (see section 3.4.1), the next line is calculated from the second and the third A-scan and so on. Thereafter, a threshold is applied to the amplitude image, and for every pixel with a value below this threshold the corresponding pixel in the phase image is grayed out. Thus, only phase image pixels corresponding to the object structure visible in the amplitude image are displayed in the resulting phase image, which is also displayed on the acquisition program's front panel (see Fig. 4.16 lower right display).

To record a measurement consisting of one or more B-scans, the displays need to be turned off, as the displays and their necessary mathematical operations require too much computing power and would slow down the data acquisition, i.e. there are no live images available during the data acquisition process.

The reference arm and the sample arm of the OCT system need to have approximately the same length, or else no object structure is visible in the intensity image display. If that is not the case, the reference mirror position has to be modified until the cross-sectional intensity image becomes visible in the display. The desired measurement position on the sample is found by means of the DVA fundus image and the system's target laser[xi]. Furthermore, the afore described OCT intensity live display is needed to check the focusing of the sample beam and the signal quality,

---

[x] An artificial eye is basically a lens focusing the sample beam onto a sheet of paper with lines drawn onto it. The incident light is absorbed by the ink of the lines and, consequently, cannot penetrate the paper as deep as in the other regions.

[xi] The DVA is designed for visible light and thus, cannot detect infrared light. Therefore, a target laser beam in the visible range (about 650 nm) that has to be collinear with the sample beam, is coupled into the OCT system.

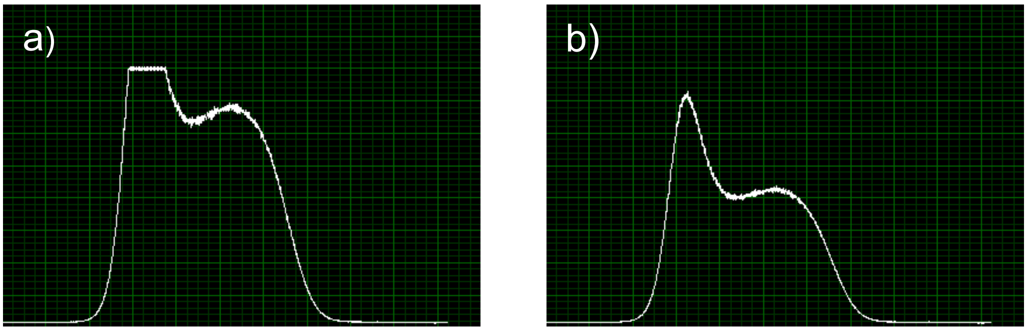

Figure 4.18: Spectrum of a single A-scan; a) recorded while the line camera was driven into saturation, b) recorded after the reference arm power was reduced, so that the line camera was not driven into saturation.

while the phase live image is used to verify that the Doppler angle does not equal 90°, in which case the blood flow velocity could not be measured, which would make it impossible to distinguish between blood vessels and static tissue in the phase image. Additionally, the powers of the recorded A-scan spectra have to be at a maximum without driving the line camera into saturation (see Fig. 4.18); this can be determined via the *A-scan spectra* display (upper left in Fig. 4.16). Since the main power of the back-reflected light comes from the reference arm, as the reference mirror usually has a much higher reflectivity than the sample layers, the power of the spectra can be increased or decreased by manipulating the NDF (neutral wedge, Qioptiq Photonics GmbH) in the system's reference arm.

4.3.2 Data evaluation

To evaluate the recorded Doppler OCT data of a capillary or an in vivo experiment, several post-processing steps have to be executed, before the data can be statistically evaluated and plotted with programs such as e.g. Microsoft Excel or OriginPro.

Image processing of amplitude and phase images

At first, the post-processing program reads the saved spectral data of one B-scan at a time from the binary files and exports the processed amplitude and phase images automatically.

In contrast to the data acquisition program (described in the previous section 4.3.1), the data evaluation program does not subtract one reference spectrum from all A-scans contained in the whole stack of B-scans of one OCT measurement, but it calculates a 'mean spectrum' for every B-scan individually, and subtracts the same from every line of the B-scan it was calculated from. To calculate a 'mean spectrum', the pixel by pixel mean value of all A-scans in a B-scan is taken. Thus, the background frequencies caused by e.g. the system's internal reflexes are retained, as they are the same in every A-scan, while the changing frequencies of the sample are averaged out. This method gives more reliable results than the reference spectrum technique. However, it also needs needs more computing power than the subtraction of a single reference spectrum from all A-scans of a recorded B-scan stack, which is the reason why the 'mean spectrum' method was not used in the data acquisition program, since it would have delayed the update rate of the live displays. The computing time, however, is of no consequence in case of the post-processing program, as the calculations and the data export are fully automatic.

The next step is the rescaling of all spectra, as they are recorded in λ-space and the data points are, thus, not equidistant in frequency-space (see section A.2 for further explanation). Subsequently, potentially remaining dispersion effects are compensated numerically, as the dispersion compensation in the reference arm (glass block), which compensates for lenses and eye (see section 4.1.2) is not perfect. This imperfectness of the dispersion compensation can be increased due to the fact that every rat eye is slightly different. Therefore, the compensation can be further improved by a numerical dispersion compensation. As the spectrometer's spectral fringe pattern is a real function, a Hilbert transformation has to be used to create a complex analytic representation of the spectral fringe pattern $\hat{S}(k) = |S(k)|\,\mathrm{e}^{i\phi(k)}$. The phase of $\hat{S}(k)$ is then corrected using an algorithm developed by Wojtkowski et al. [76]:

$$\bar{\phi}(k) = \phi(k_0) - a_2(k-k_0)^2 - a_3(k-k_0)^3, \tag{4.26}$$

where $\phi(k_0)$ is the original phase. The parameters a_2 and a_3 were chosen manually to improve the image quality. However, the values should be varied carefully, as wrong parameters in Eq. (4.26) can distort the amplitude image even more than insufficient or too much dispersion compensating glass in the reference arm. As shown in Fig. 4.19, an amplitude image with poor dispersion compensation looks blurry, while the same image appears sharper and more details become visible after applying the proper dispersion compensation.

The resulting rescaled and dispersion compensated data is then Fourier transformed using a fast Fourier transform algorithm. As shown in section 3.3.1, this Fourier transformation gives cross-correlation and auto-correlation terms, which are symmetrical with their mirror terms around zero, i.e. half of the resulting data are irrelevant. Thus, the half of each A-scan spectrum that is containing the mirror terms is deleted to save computing power and system memory, as well as disk space, since the processed tomograms are stored on the hard disk drive. The Fourier transformation yields complex data: the amplitudes of the complex data points are the intensity values that correspond to the object structure of the sample. Displaying all amplitude values of a B-scan as gray scale values gives the B-scan's amplitude tomogram; an example showing a cross-sectional region of a rat's retina and choroid can be seen in Fig. 4.19.

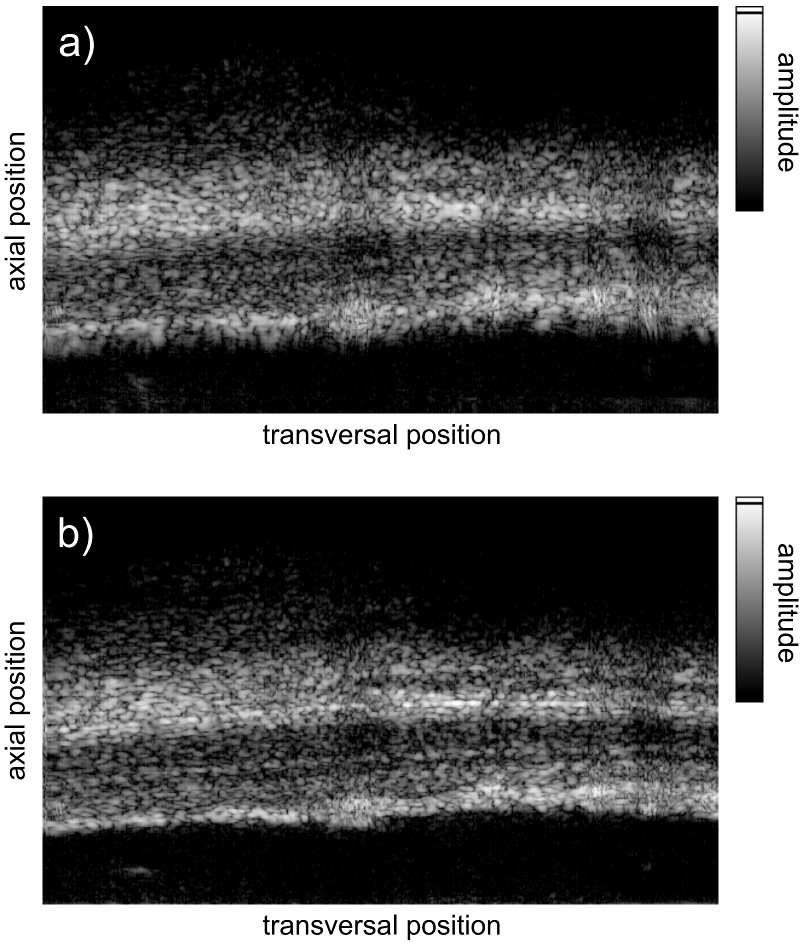

Figure 4.19: Rescaled amplitude tomogram of a rat retina with poor a) and proper b) dispersion compensation.

The phase data of the rescaled, dispersion compensated and Fourier transformed A-scan spectra $i_{D,n} = A_n \cdot \mathrm{e}^{i\phi_n}$ can be used to calculated the phase difference of two adjacent A-scans, which is proportional to the sample particle velocity (see Eq. (3.74)). However, as described in section 3.4.1, this method requires the two A-scans to be recorded exactly at the same sample positions at different times. As already mentioned in the description of the oversampling factor in section 4.1.5, the probe beam has to be scanned across the sample to acquire a B-scan. Thus, two adjacent A-scans are not recorded exactly at the same sample position. However, the diameter of a rat's red blood cell is about 7 µm [73], while the distance between two consecutive sample points is about 1 µm, which can be calculated by dividing the beam width $\delta x = 11.3\,\mu\mathrm{m}$ (see lateral resolution in section 4.1.5) by the used OF[xii]. Therefore, two consecutive sample points can be considered to be at the same position. The data evaluation program calculates the phase difference tomogram of

---

[xii] The oversampling factor OF = 10 was used for the capillary measurements in section 4.2.2, as well as for the in vivo measurements described in section 4.4.

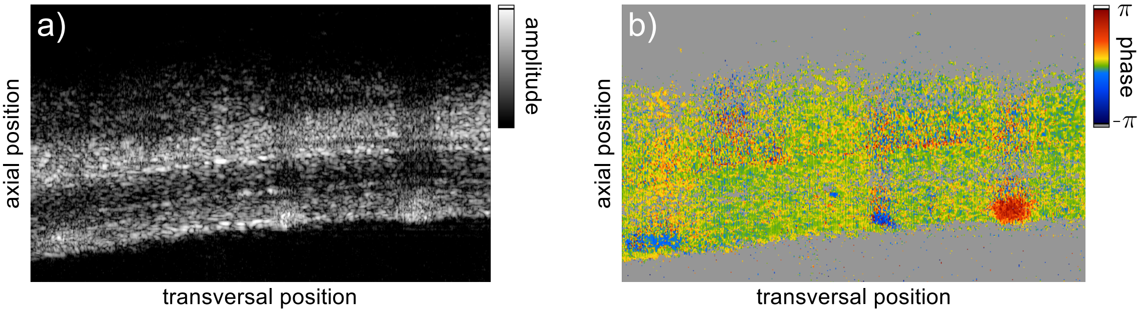

Figure 4.20: This figure shows the rescaled and dispersion compensated amplitude tomogram a), as well as the thresholded and motion corrected phase tomogram b) of a single B-scan from an in vivo measurement of a rat retina.

a whole B-scan, as it multiplies each A-scan (line) spectrum $i_{D,n}$ of a B-scan with the complex conjugate of its previous A-scan spectrum, line by line (cf. Eq. (3.68)):

$$A_{n-1} \cdot \mathrm{e}^{-i\phi_{n-1}} \cdot A_n \cdot \mathrm{e}^{i\phi_n} = A_{n-1}A_n \cdot \mathrm{e}^{i(\phi_n - \phi_{n-1})}. \tag{4.27}$$

The phase values of the result $\Delta\phi_{D,n} = \phi_n - \phi_{n-1}$ represent the values of the B-scan's phase difference tomogram.

Subsequently, as already mentioned in the description of the data acquisition program (see section 4.3.1), a threshold with respect to the amplitude image is applied to the phase image. To this end, the value of every pixel of the amplitude image has to be compared to the threshold, and if a pixel value is below the threshold, the corresponding pixel value of the phase image will be set to -100, and thus, be grayed out in the phase image, as this value lies far outside the phase value range, which is between $-\pi$ and π. This is done to show only the phase data of the highly reflective sample layers and the blood vessels in the phase images. An example for a phase tomogram and its corresponding amplitude tomogram is shown in Fig. 4.20, where the phase image is displayed as false-color image, so that blood vessel can easier be distinguished from static tissue. The pixels with greenish-yellowish color in Fig. 4.20 b) indicate that the Doppler shift and hence the axial sample velocity equals zero, while red and blue areas indicate the occurrence of blood vessels with positive or negative flow velocities. The tissue behind the large vessels is shadowed, as the blood inside the vessels reflects and absorbs more of the sample beam's light than the surrounding tissue. Furthermore, the phase values of the shadowed areas behind a large vessel are obscured due to multiple scattering of the incident light at the red blood cells.

Since the blood flow velocity measurement via Doppler OCT is a very sample motion sensitive technique, slight movements of the rat eye, or movements of the animal's head caused by respiration can induce phase shifts in the whole B-scan, or to parts of it. Such "bulk motion" artifacts are corrected by means of a histogram based correction method (see Fig. 4.21) that was first used by Makita et al. [77], and then

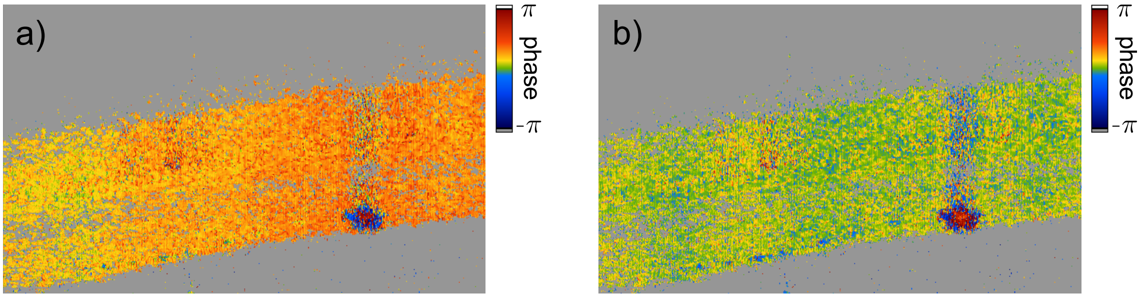

Figure 4.21: Image a) shows an in vivo phase tomogram of a rat retina with a sample motion artifact over the whole B-scan, while image b) shows the motion corrected version of the same phase tomogram.

adapted by Schmoll et al. [72] and Werkmeister et al. [78]. The bulk motion correction LabVIEW subprogram that is implemented in the data evaluation program was written by René Werkmeister.

After performing all those steps, the data evaluation program saves all the calculated amplitude and phase image data of a whole B-scan stack which was acquired during one OCT measurement to the HDD for further evaluation.

Blood vessel evaluation

To evaluate and average the velocity, or rather the phase data of one blood vessel in all phase images of one OCT measurement, only a small area containing the vessel data is extracted from every phase tomogram. The vessel area is selected via two horizontal and two vertical cursors (see Fig. 4.22). The cursors can be dragged per mouse or moved by entering the cursors' pixel position into numerical control fields. With decreasing blood flow velocity and signal quality, it is increasingly difficult to recognize the vessel's border or even its position. The most obvious way to identify a blood vessel is to use the color of the phase image, but using this method, one should keep in mind that the velocities close to the vessel border are small, which could lead to an underestimation of the vessel dimensions. Additionally, the afore mentioned shadowing of the regions behind the vessels in amplitude and phase image (see Fig. 4.20) can be used to find the transversal vessel borders. However, multiple scattering of the incident light in the blood vessel obscures the phase data of the tissue behind the vessel, which hampers the identification of the blood vessel's rear border. Consequently, some experience is required for reproducible vessel area determination.

In order to evaluate the vessel data of a whole series of measurements, the vessel area has to be defined by the cursors (see Fig. 4.22) for every B-scan, which means 140 times per measurement point, since the vessel position varies in consecutive B-scans due to sample motion. Thus, the vessel area extraction is the most time-consuming

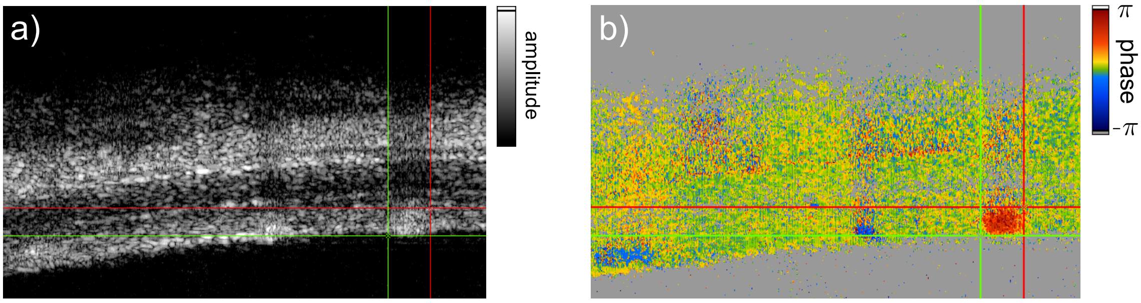

Figure 4.22: The blood vessel area is marked in both, amplitude and phase image using the green and the red cursors.

of all post-processing steps. Therefore, a vessel search subprogram that was written by Veronika Doblhoff-Dier and Stefan Löffler is implemented in the vessel extraction LabVIEW program. The subprogram locates vessels in a predefined searching area by fitting an ellipse into the phase images using a downhill simplex algorithm. The major and minor semi-axes of this ellipse have to be set manually, by defining the transversal as well as the axial vessel diameter using the green and the red cursors, as illustrated in Fig. 4.22. Then, the search algorithm tries to maximize the number of positive (or negative) pixels inside the ellipse, while the number of pixels outside the ellipse is minimized. This automatic vessel search method worked well for phase images with good signal quality and high velocities, so that the vessels were clearly distinguishable from static tissue. However, it was still necessary to monitor the automatic vessel detection and make manual adjustments in case of detection errors. Nevertheless, this semi-automatic vessel search technique saved a lot of time in the data evaluation.

After the vessel detection, the cursor positions are saved to a text file and the vessel areas of a B-scan stack are saved to a binary file, along with a size file describing the vessel areas' dimensions and the amount of B-scans in a stack.

For further evaluation, one vessel area stack is loaded into the vessel calculation LabVIEW program. In the event of high axial velocity components of the flow in a blood vessel, the phase values can exceed the phase angle range $[-\pi, \pi]$ of the Fourier transformed data and the phase values will 'wrap', i.e. values exceeding one end of this range (e.g. $-\pi$) will jump to the other end of the phase angle range. This 'phase wrapping' appears as a seemingly reverse flow in the center of the blood vessel (see Fig. 4.23 a), b), c). In case of single phase wrapping the data can be 'unwrapped' by adding or subtracting 2π, depending on whether the phase shift is positive or negative, which expands the phase angle range to $[-2\pi, 2\pi]$[xiii]. To unwrap the vessel data, the algebraic sign of the phase shift, as well as a phase threshold have to be set

---

[xiii] If the phase values still exceed the expanded range of $[-2\pi, 2\pi]$, this phenomenon is referred to as multiple phase wrapping. No multiple phase wrapping was encountered in the experiments that were conducted in the course of this thesis.

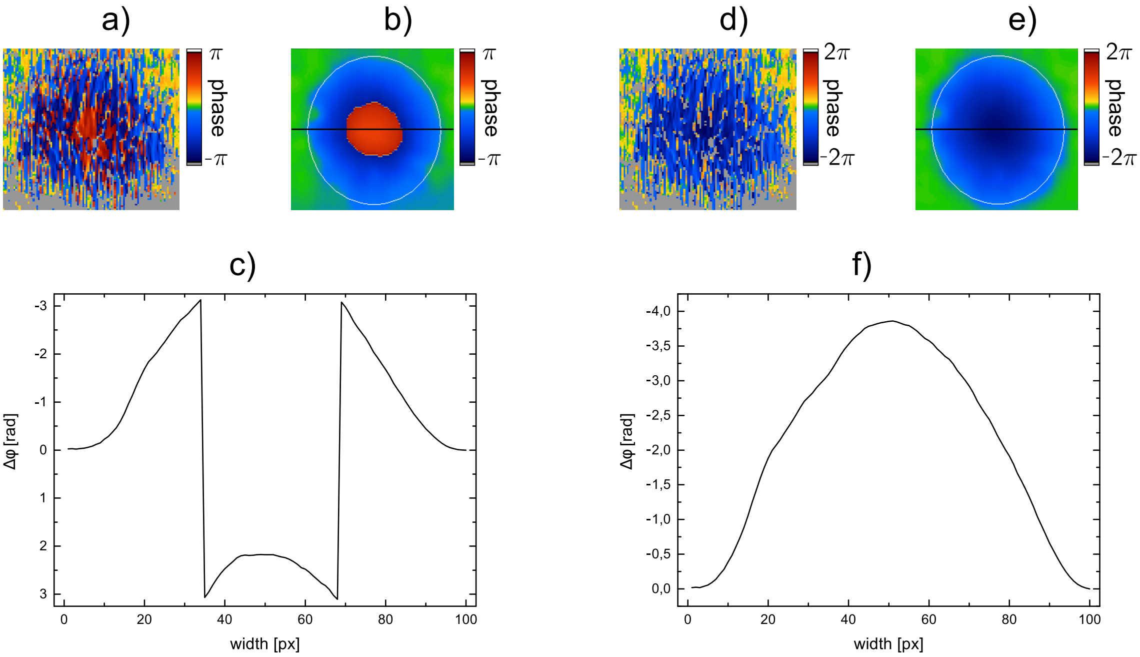

Figure 4.23: The images a), b) and c) show a phase wrapping artifact of a retinal blood vessel, while the images d), e) and f) represent the same blood vessel after the unwrapping procedure. The phase images a) and d) show a vessel area of a single B-scan; b) and e) are the corresponding averaged vessel areas of a whole B-scan stack (consisting of 140 B-scans); c) and f) show the velocity profiles of the averaged phase images at the positions of the black lines.

manually in the vessel calculation program, so that only those data points exceeding $[-\pi, \pi]$ are unwrapped. An example of the unwrapping procedure can be seen in Fig. 4.23, where the images on the left side a), b) and c) show a retinal vessel with a phase wrapping artifact, while the images on the right side d), e) and f) are the corresponding images of the unwrapped phase data. During the vessel evaluation, the necessity for unwrapping was decided for every B-scan stack individually.

Since the data points that were set to -100 are not included in the calculation of the vessel's mean phase shift, these 'missing' data points can lead to an underestimation of the mean phase shift (see Fig. 4.24). Therefore, the -100 values inside the vessel have to be interpolated, to prevent such an underestimation of the blood vessel's mean phase shift (see Fig. 4.24). The missing data points are calculated according to a parabolic fit-function:

$$f(x, y) = a + bx + cy + dx^2 + ey^2 + fxy. \tag{4.28}$$

After fitting, a mean filter in the form of a convolution with a 7×7 matrix is applied to the data to remove potential outliers.

Then, finally, the vessel's mean value of every phase tomogram in a B-scan stack is

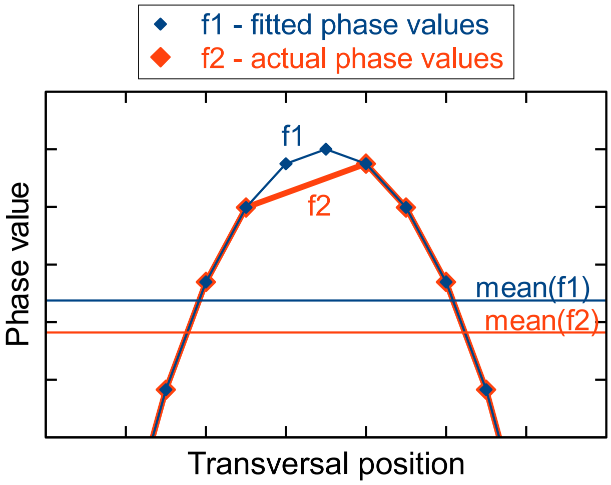

Figure 4.24: This graph illustrates the error being made, if the data points inside the vessel that were set to -100 are not fitted but excluded from the calculation of the mean phase shift. The red curve $f2$ is the result of the -100 values being excluded from the dataset, while the fitted data yields the blue curve $f1$, which is closer to reality (adapted from Doblhoff-Dier [21]).

calculated and written into a text file. The resulting list of mean phase values can be imported into any spreadsheet software.

In the course of this thesis, OriginPro 9.1 was used for all statistical calculations as well as for the creation of statistical plots.

4.4 In vivo measurements in large retinal veins

The following experiments and results were already published 2014 in the Journal of Biomedical Optics [65].

All OCT measurements described in this section were acquired and evaluated as explained in section 4.3. The vessel diameters were measured via the DVA rodent by Imedos (see section 4.1.3) and recorded using the commercially available RVA4.16 software, which was also developed by Imedos.

In order to test the single beam system's ability to detect relative changes in the retinal blood flow, two different in vivo experiments were conducted. In the first experiment, oxygen induced vasoconstriction was investigated, while vasodilation due to flicker light stimulation was studied in the second experiment.

In all animals of both experiments, only one major retinal vein was measured, since high velocities in the arteries, especially during systole, can cause multiple phase wrapping and fringe washout[xiv]. This limitation is caused by the relatively long exposure time of the used line cameras (see the velocity range of the OCT system in section 4.1.5). Thus, faster cameras would be needed to measure the high blood flow velocities in retinal arteries without encountering any multiple phase wrapping artifacts or fringe washout. Those phenomena have to be avoided, as they would make the calculation of a vessel's mean phase value more difficult and could lead to an underestimation of the actual mean phase value. However, the measurement of retinal veins would be sufficient for the assessment of the retinal perfusion, as the blood inflow into the inner retina through the CRA (see section 2.2) equals the blood outflow through the CRV [61].

The OCT scanning position on the retina of each animal measured in the experiments described in this section was chosen to be at a distance of one to two diameters of the optic disk from the ONH. The length of the scanned line on the rat retina, and thus the width of the acquired B-scans was 1.1 mm, using an oversampling factor of 10. During one OCT measurement, a stack of 140 B-scans was acquired, so that possible flow irregularities (retinal veins may show a low heart beat related pulsatility) averaged out.

4.4.1 Animal preparation

The measurements were performed following the statement for the use of animals in ophthalmic and vision research of the association for research in vision and ophthalmology (ARVO) and were approved by the ethical committee for animal experiments of the Medical University of Vienna.

For both the vasoconstriction and the vasodilation experiments, male Sprague-Dawley rats with a body weight in the range of 400 to 600 g were used. Anesthesia was induced by an intraperitoneal injection of 100 mg/kg ketamine and 5 mg/kg xylazine. Subsequently, the animals were intubated and ventilated with oxygen and 2 % isoflurane at a ventilator frequency (VF) of 70/min to maintain deep anesthesia during the surgical procedure. Then a bolus of 20 mg/kg was administered via a venous access. After that, the animals got a continuous intravenous infusion of 50 mg/kg/h ketamine, 0.05 mg/kg/h fentanyl and 20 mg/kg/h gallamine triethiodide. To control the depth of the anesthesia, blood pressure and heart rate were monitored permanently. Only the right eyes of the animals were used for the measurements. In order to prevent the rats' eyes from drying out and to maintain good imaging quality, the

---

[xiv] Fringe washout is a sensitivity decay phenomenon known in spectral domain FDOCT, where the signal to noise ratio (SNR) decreases with increasing transverse sample particle velocities [79]. To counteract the fringe washout, a shorter camera integration time would be needed. This can be achieved by using a faster line camera, or by using only a part of the camera's CCD pixels, to reduce the camera readout time. However, the second approach would decrease the range of detectable wavelengths and degrade the image resolution of the OCT system.

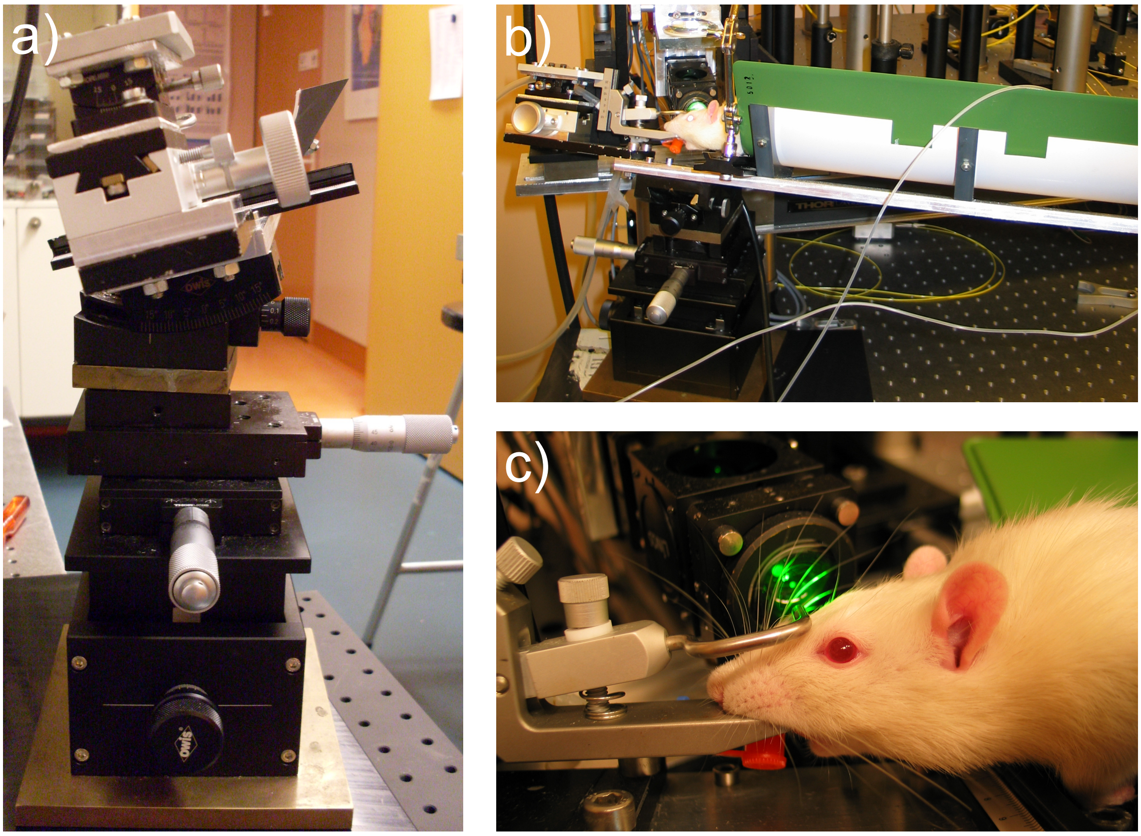

Figure 4.25: Photograph a) shows the front view of the rat holder with one vertical and two horizontal (x and y direction) translation stages, as well as the tilted goniometer table. In image b), the side view of the holder with a green heating mat and a test animal can be seen. Photograph c) shows the head of the rat with its teeth hooked into the tooth bar.

eyes were constantly moistened with eye drops containing hyaluronic acid (Hylo-Comod, 1 mg/ml sodium hylauronat; Ursapharm, Saarbrücken, Germany), except for the ongoing measurement (during DVA and OCT data acquisition).

The anesthetized rats were then put onto an animal holder, which allowed to manipulate the animals position in x, y and z axes, as well as to tilt the whole animal along its longitudinal axis (see Fig. 4.25). Furthermore, the animals teeth had to be hooked into a tooth bar to prevent the head from rolling to the side at high tilting angles. A heating mat beneath the rat was used to maintain a constant body temperature during the measurements. For a successful measurement, the animal position had to be altered by manipulating the animal holder's translation stages and its goniometer table, until a sharp DVA fundus image, a good OCT signal and a Doppler angle different from 90° was reached.

After completion of the experiments, the animals were euthanized via a lethal injection of pentobarbital (Release, Wirtschaftsgenossenschaft deutscher Tierärzte eG).

4.4.2 Vasoconstriction measurements

The single beam system's capability to detect in vivo flow changes in retinal vessels firstly was investigated by means of oxygen induced vasoconstriction measurements in six animals.

Experiment protocol

Once the animals were prepared for the measurements, as described in section 4.4.1, the ventilation gas was changed to ambient air for 10 minutes at constant VF. Then, the animals were ventilated with 100 % oxygen for another 10 minutes. Vessel diameter acquisition via the DVA was started at minute 8 of the air breathing phase and ran continuously until the end of the measurement (see Fig. 4.26). The vessel's blood flow velocity was measured, using the OCT system, at the minutes 8 and 9 of the air breathing phase and at the minutes 2, 4, 6, 8, 9 and 10 of the oxygen breathing phase. The data recorded at the air breathing phase were considered as the baseline of the measurement. The animals eyes were moistened constantly, except for the duration of the DVA and OCT measurements.

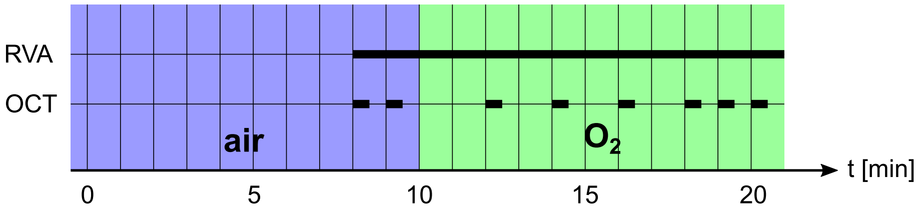

Figure 4.26: Experiment protocol of the hyperoxia induced vasoconstriction measurements (derived from a figure already published by the author [65]).

Results

The results of the vasoconstriction measurement of one animal are shown in Fig. 4.27. The phase tomogram Fig. 4.27 a) was recorded using the Doppler OCT method described in the section 3.4 and was acquired and post-processed as explained in section 4.3. This image shows one retinal vein at baseline conditions (during the air breathing phase) with a vessel diameter of approximately 100 µm that has a clearly visible phase wrapping artifact in the vessel center. The unwrapped nearly parabolic velocity profile through the vessels center is plotted in Fig. 4.27 c). After 10 min of oxygen breathing, the vessel diameter decreased to approximately 92 µm and the phase wrapping artifact disappeared as a result of the reduced blood flow velocity, as can be seen in Fig. 4.27 b). This decrease in vessel diameter and blood flow velocity is also visible in the velocity profile shown in Fig. 4.27 d), which is

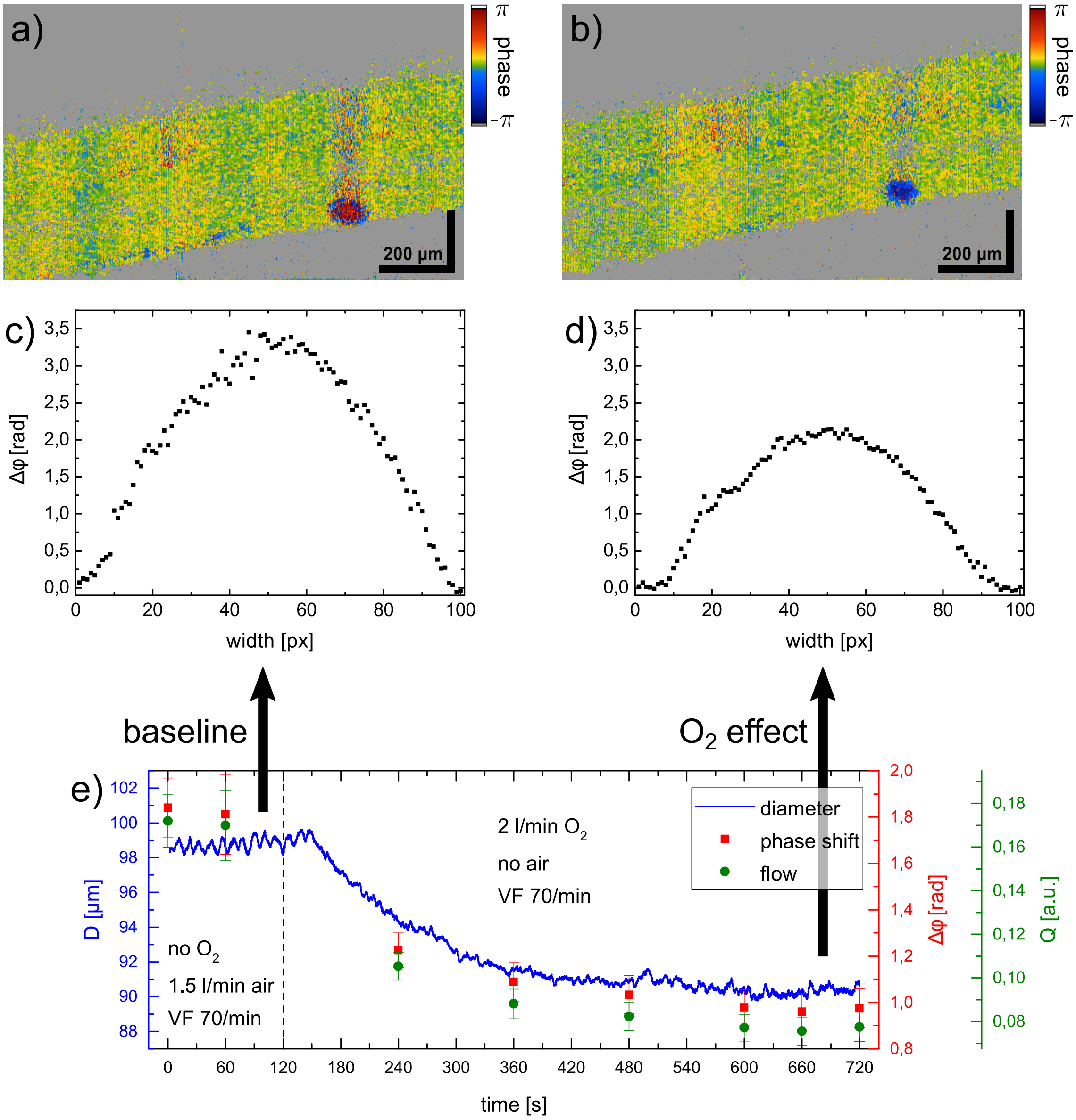

Figure 4.27: Image a) shows a phase tomogram containing a large retinal vein (with a phase wrapping artifact) acquired under baseline conditions and image c) illustrates the extracted unwrapped vessel profile. b) and d) show the corresponding images after 10 min of oxygen breathing. In graph e), the vessel's continuously measured diameter D, the phase shift $\Delta\phi$ measured via the OCT and the calculated relative flow Q are plotted against the measurement time. The dashed line at 120 s marks the change of the ventilation gas from ambient air to 100 % oxygen (derived from figures already published by the author [65]).

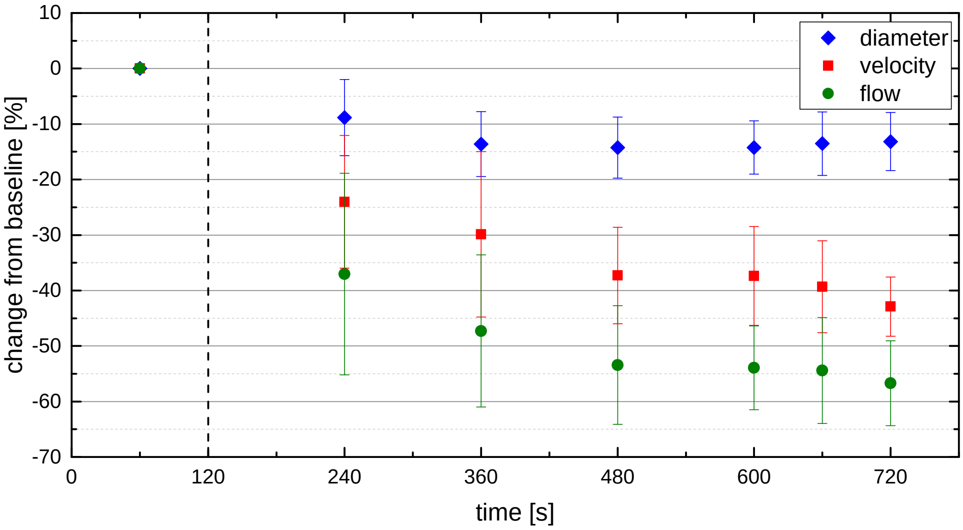

Figure 4.28: In this graph, the relative changes of diameter (blue diamonds), blood flow velocity (red squares), and blood flow (green circles) from baseline conditions during 100 % oxygen breathing are plotted over the measurement time. The datapoints represent the mean values ± SD of the large retinal veins measured in 6 animals. The dashed line indicates the start of the oxygen breathing phase.

still nearly parabolic, even though the blood flow velocity is significantly reduced. The acquired vessel diameter data of the whole measurement, as well as the eight Doppler OCT measurement points (see the experiment protocol paragraph of this section for the exact time points) and the vessel's blood flow are plotted over the measurement time in Fig. 4.27 e). The blood flow was calculated using the relation

$$Q = v \cdot A = v \cdot \frac{D^2\pi}{4} \propto \Delta\phi \cdot \frac{D^2\pi}{4}, \tag{4.29}$$

where A stands for the vessel's cross sectional area. As mentioned in section 3.4.2, the single beam Doppler OCT method used for the experiments described in this section could not measure absolute velocity values due to the lacking knowledge of the Doppler angle. Thus, the blood flow Q can only be calculated in arbitrary units. The vessel diameter curve of Fig. 4.27 e) shows that the diameter started to decrease less than 60 s after the ventilation gas was switched to 100 % oxygen. After about 360 s of oxygen breathing, the full vasocostriction effect was reached and the vessel diameter remained constant until the end of the experiment. A similar behavior can be observed for the phase shift, which is proportional to the blood flow velocity (cf. Eq. (3.74)), as well as for the blood flow (see Fig. 4.27 e)).

The change from baseline of the vessel diameter, the blood flow velocity and the blood flow was calculated for every OCT measurement time point, and then averaged for all six animals. The resulting mean values ± SD are plotted in Fig. 4.28. In this graph, it is clearly visible that the velocity decrease is far more distinct than the decrease of the venous diameter. After 600 s of oxygen breathing, a vasoconstriction of $(13.2 \pm 5.2)\,\%$, a blood flow velocity reduction of $(42.9 \pm 5.3)\,\%$ and a decrease in blood flow of $(56.7 \pm 7.6)\,\%$ can be observed.

It should be mentioned that in some rats, the eyes dried out sooner than in the other animals, which resulted in a blurry fundus image and a bad OCT signal. This issue was mostly related to scratches on the animals' corneas and to unusually long animal preparation times. In case of blurry fundus images, the DVA software had problems measuring the correct vessel diameter and misleadingly detected an increase of the vessel diameter with ongoing drying-out of the rat eye. If this was the case, the eye had to be moisturized with Hylo-Comod during the ongoing measurement; this had to be done carefully, so as not to move the animal and unintentionally change the measurement position. Also, the formation of a large drop on the eye's cornea had to be avoided, since this might change the eye's refractive power, also leading again to wrong vessel diameters, or even to different Doppler angles and thus to distorted phase-shift values.

4.4.3 Vasodilation measurements

The second experiment set that was conducted to test the single beam OCT system's ability to measure relative changes in the retinal blood flow were flicker light induced vasodilation measurements.

Experiment protocol

The ventilation gas and the VF of the test animals remained constant for the whole experiment. After positioning the rat in front of the measurement system and prior to the data acquisition, the RVA light as well as the ambient light were turned off for 10 min to let the animal's eyes adapt to the darkness. Then, the RVA light was switched on and the rat's position was fine adjusted. Subsequently, the vessel diameter measurement via the DVA and the first blood velocity measurement via the OCT system were started. This moment was defined as zero time point of the measurement (see Fig. 4.29). The light adaption phase lasted for 60 s, after which the RVA light was switched off to let the rat adapt to darkness again for 3 minutes. Two OCT measurements were recorded during the darkness adaption phase at the total time points 80 s and 200 s. The DVA system acquired data continuously throughout the measurement, although it could not measure vessel diameters while the RVA light was switched off. After the darkness adaption phase, a diffuse flicker light with a flicker frequency of 12 Hz was activated for 60 s and applied via the RVA's illumination path. An OCT measurement was recorded 20 s after the start of the flicker phase, at the time point 260 s. Then the flicker was turned off and the rat eye

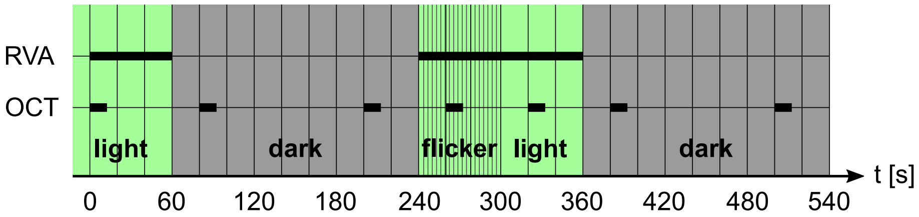

Figure 4.29: Experiment protocol of the flicker light induced vasodilatation measurements (derived from a figure already published by the author [65]).

was illuminated with constant RVA light for 60 s. An OCT measurement was taken at the time point 320 s. This light adaption phase was followed by another darkness adaption phase lasting 3 minutes, during which the last two OCT measurements were recorded at the time points 380 s and 500 s.

The ambient light remained turned off for the whole experiment to avoid possible degradation of the expected flicker light induced vasodilation effect.

Results

Fig. 4.30 shows the flicker light induced increase in the vessel diameter, the phase shift (proportional to the blood flow velocity), as well as the blood flow of one test animal. The DVA could not detect vessel diameters during the darkness adaption phases, as it needs the RVA light to acquire the fundus images that are required for the vessel diameter determination by the RVA4.16 software. Consequently, no blood flow values could be calculated for the dark phases. However, since the OCT system uses infrared light, blood velocity data could also be acquired during the dark phases. During the first light and the first darkness adaption phase, the blood flow velocity basically remained constant. Immediately after the onset of the flicker stimulus, the vessel diameter (see the blue curve in Fig. 4.30) started to increase and reached its peak value a few seconds afterwards, whereupon the diameter decreased again approximately half the value of its increase. An even higher increase due to the flicker light can be observed in the vessel's blood flow velocity (red squares) and in its blood flow (green circles). Throughout the light adaption phase following the flicker stimulus, vessel diameter, blood velocity and blood flow decreased slightly, but stayed elevated compared to the values from the first light adaption phase. During the second darkness adaption phase of the experiment, the blood flow velocity values went down to almost baseline conditions (the values measured during the first light adaption phase).

The changes from baseline in vessel diameter (blue diamonds), blood flow velocity (red squares) and blood flow (green circles) were averaged for the four animals on which the experiment was conducted, and the mean values ± SD are displayed in Fig. 4.31. The increase in the averaged venous vessel diameter was very small,

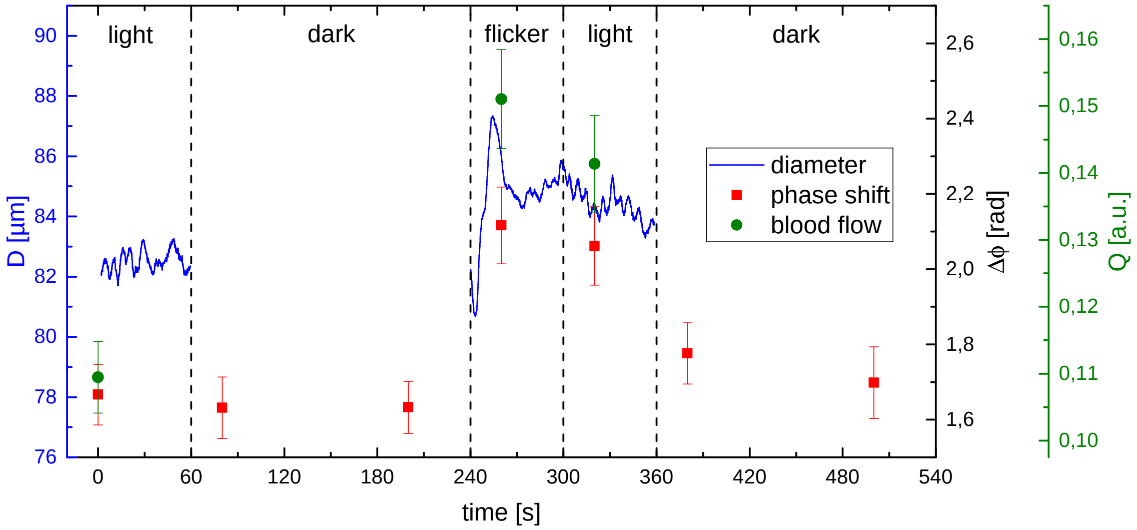

Figure 4.30: This figure shows flicker light induced changes in vessel diameter D, phase shift $\Delta\phi$ and thus blood flow velocity, as well as in the blood flow Q (derived from a figure, already published by the author [65]).

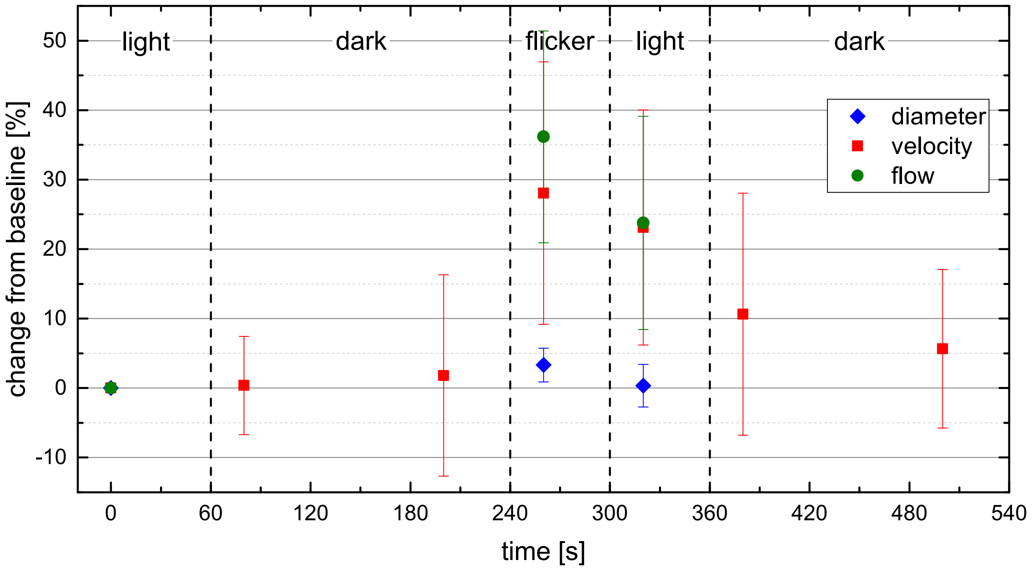

Figure 4.31: Relative changes of diameter (blue diamonds), blood flow velocity (red squares), and blood flow (green circles) due to flicker light stimulation. The datapoints represent the mean values ± SD of the large retinal veins measured in 4 animals.

merely $(3.2 \pm 2.4)\,\%$ at the peak value during the flicker stimulation; after the flicker stimulation, the vessel diameter decreased until it reached baseline values again. As mentioned above, the diameter values could not be determined during the darkness adaption phases. The averaged velocity value showed no change from baseline during the darkness adaption phase. However, in contrast to the averaged vessel diameter, the averaged velocity showed a much more pronounced increase of $(28.1 \pm 18.9)\,\%$ during the flicker stimulation. In agreement with the vessel diameter's behavior, the blood flow velocity decreased during the subsequent light adaption phase, but still remained elevated compared to its baseline. Throughout the following second darkness adaption phase the mean velocity values decreased further, nearly reaching baseline conditions. The averaged blood flow shows an even higher increase of $(36.2 \pm 15.2)\,\%$ due to flicker light stimulation; just like the flow velocity, the blood flow also decreased during the second light adaption phase, but remained elevated in comparison to its baseline.

4.4.4 Discussion

As already mentioned in section 2.5, several methods exist, which are capable of measuring the retinal blood flow. The Doppler OCT technique was chosen for the experiments conducted in the course of this work, as it is a very versatile method, capable of acquiring structural images (even 3D data-sets), as well as blood flow velocity information via the phase difference tomograms. Furthermore, depending on the measurement position, several blood vessels can be measured at once, in contrast to e.g. the LDV technique. In addition, it is possible to measure vessel diameters using the OCT amplitude or phase images, but as previously mentioned in the sections 4.1.3 and 4.3.2, the identification of the rear vessel wall can be difficult due to shadowing and multiple scattering. Using the phase image to extract the blood vessel width may lead to a velocity dependent underestimation of the vessel diameter, since the velocities close to the vessel wall are below the OCT system's minimum detectable velocity [46]. Additionally, the vessel diameter measurement via OCT images is limited by the system's axial resolution. In order to avoid these limitations of the vessel diameter measurement via OCT and due to the fact that the vessel diameter enters into the blood flow calculation with the second order, a commercial fundus camera (DVA rodent, Imedos), which has a resolution of up to 0.1 µm (see section 4.1.3), was combined with the OCT system.

The main limitation of the blood flow measurement via the Doppler OCT method, is its sensitivity to sample motion, which was negligible in the experiments described in this thesis due to the fact that only anesthetized animals were measured. However, in human measurements this limitation can be problematic, since it is likely that patients will move their eyes or even their heads unintentionally during the OCT data acquisition. Two common solutions for the eye motion problem in human experiments are firstly to keep the measurement time as short as possible, and secondly to use a fixation target on which the patient has to stare without blinking for the whole data acquisition time. Furthermore, the patient's head can be strapped to the head rest in order to minimize unintentional head movements.

The experiments described in section 4.4.2 show a vasoconstriction and a reduction in the retinal blood flow due to hyperoxia, which is induced by 100 % oxygen breathing. Changes in retinal blood flow, triggered by hyperoxia, have already been investigated in the rat by several other studies, using different measurement methods, e.g. magnetic resonance imaging [80] and scanning laser Doppler flowmetry [81]. Both of these studies reported a reduction in the retinal blood flow of about 25 %. Another study that used a dye dilution technique, measured a decrease in retinal blood flow of about 62 % [82]. The latter value, as well as the decrease in the venous blood flow of (56.7 ± 7.6) % that was presented in section 4.4.2 of the work at hand, are in good agreement with the results from human experiments, which range from 36 % – 60 % [83–88].

One reason to use hyperoxia for testing the OCT system's capability of measuring changes in the rat's retinal blood flow was the generally known pronounced decrease in vessel diameter, blood flow velocity and blood flow due to 100 % oxygen breathing. The fact that these regulatory responses to hyperoxia are disturbed early in diabetes [11], is another reason to study hyperoxia in animals, even though it is currently not known which mechanisms are responsible for these reduced regulatory responses to hyperoxia [89, 90].

The second set of experiments, described in section 4.4.3, used flicker light as stimulus to induce a change in the retinal blood flow. The flicker light stimulation leads to an increased neural activity in the retina, and thus to an increase in the retinal blood flow (hyperemia) to satisfy the heightened metabolic demands of the active tissue. This coupling between increased neural activity and hyperemia is called neurovascular coupling [91–93]. The retinal flicker response was measured using different techniques, namely laser speckle flowgraphy [94, 95], fluorescent microspheres [96], retinal vessel diameter assessment [97] and Doppler OCT [98]. The results of the flicker light experiments, conducted in the course of the work at hand (see section 4.4.3), show that the main part of the flicker light induced blood flow increase of (36.2 ± 15.2) % comes from the increase in retinal blood flow velocity of (28.1 ± 18.9) %, while the venous vasodilation effect of (3.2 ± 2.4) % was only minor. Garhöfer et al. [99] came to the same conclusion with data from human experiments. They measured an increase in retinal blood flow of about 60 %, while the vasodilation was in the range of 3 % – 5 %. Therefore, it is reasonable to propose that the bigger part of the retinal response to flicker light occurs in form of vasodilation in the small arterioles, as they are the major sites of resistance to blood flow [99].

Studying the response of the retinal blood flow to flicker light stimulation is interesting, as this flicker response is reduced in early diabetes [12]. By inhibition of inducible nitric oxide synthase (iNOS) with aminoguanidine, the disturbed flicker response of diabetic rats can be restored to normality, which agrees with the fact that iNOS inhibitors slow down the progression of diabetic retinopathy [97].

5 Assessment of the retinal microcirculation using Doppler OCT

As mentioned in the explanation of the velocity range of the single beam OCT system in section 4.1.5, blood flow velocities as low as $v_{\text{min}} = 1.8\,\text{mm/s}$ could be detected for a Doppler angle of 85°, using the Doppler OCT technique described in chapter 4. Doppler angles closer to 90° yield higher minimum detectable velocities, e.g. $v_{\text{min}} = 8.8\,\text{mm/s}$ for a Doppler angle of 89°. However, their small diameters of about 5 µm [100] lead to quite slow blood flow velocities inside the retinal capillaries[i], which are in the range of $0.5 - 2\,\text{mm/s}$ [101–105]. Consequently, the retinal microcirculation cannot be assessed using the OCT method described in the previous chapter.

The inspection of Eq. (3.74) reveals that lower v_{min} can be achieved by increasing the time period τ between the two A-scans, which is used for the calculation of the phase difference. Zotter et al. [106] showed that a time span of $\tau = 2.5\,\text{ms}$ is an appropriate value to assess the retinal microcirculation via Doppler OCT. Inserting this value into Eq. (3.74) yields $v_{\text{min}} = 0.2\,\text{mm/s}$ for a Doppler angle of 89°. Higher τ values lead to more phase noise and make the method even more motion sensitive [106], since there is simply more time for potential movements of the sample eye. In case of much too high τ values for the measured velocity range, the phase data will be uncorrelated, as a scatterer measured at a certain position will have completely moved past this position after the time τ has passed, so that the consecutive measurement detects a different scatterer, which will lead to random phase fluctuations.

The easiest way to achieve a time span of $\tau = 2.5\,\text{ms}$ between two consecutive A-scans is to simply use a slower A-scan rate, i.e. to have the scanner move the sample beam to the next position only after 2.5 ms. However, this way, a single B-scan consisting of 1000 A-scans would take 2.5 s and the acquisition of one OCT measurement including 100 B-scans would require about 4 min. This approach is too time consuming for in vivo experiments, even though the animals are anesthetized. During the 4 min or more of data acquisition, the sample eye would most likely start to dry out and thus develop small injuries (superficial keratopathy) on the surface of the cornea by the end of the measurement, which would gradually degrade the image quality of the ongoing measurement. Just for comparison: the acquisition of 100 B-scans with $\tau = 57\,\mu\mathrm{s}$ (this τ was used for the measurements in chapter 4) takes only a few seconds, hence all 100 B-scans have approximately the same image quality.

---

[i] The blood flow velocities in the retinal capillaries are in the same range for mice, rats, cats and humans [101–105].

Another method to realize a period of $\tau = 2.5\,\mathrm{ms}$ and hence be able to assess the retinal microcirculation, is to use a much faster A-scan rate, such that a whole B-scan can be recorded in 2.5 ms. Thereafter, the phase tomograms of the consecutive B-scans can be subtracted line by line to calculate the phase difference tomogram that contains the velocity information of the retinal capillaries. This method requires ultra fast line cameras, since a framerate of 400 B-scans/s is needed to achieve a time span of $\tau = 2.5\,\mathrm{ms}$ between two consecutive B-scans [107]. It should be mentioned that the possible number of A-scans per B-scan depends on the camera speed, and consequently higher A-scan numbers require faster cameras[ii].

Two approaches capable of assessing the retinal microcirculation using the consecutive B-scan technique but operating at lower imaging speeds were realized in the form of two different measurement systems, and will be described in the following (see sections 5.1 and 5.2). In these cases, the 20 kHz line camera from the OCT setup described in chapter 4 suffices, eliminating the need for an ultrafast camera.

5.1 The dual beam OCT method

One option to achieve a time difference of a few ms between two consecutive B-scans without ultra high speed cameras is to use two sample beams from two separate interferometers that are scanned over the exact same sample position at different times [106, 108, 109]. The time delay τ between two B-scans recorded by both interferometers at the same position can be controlled via a constant offset among both sample beams (see Fig. 5.1). An OCT setup with two separate interferometers will be presented in the following section.

5.1.1 Experimental dual beam OCT setup

The dual beam OCT setup that will be described in this section, is based on a system for optical micro-angiography measurements that was introduced by Zotter et al. [106]. Several adaptions were made to enable measurements of rat eyes and

---

[ii] Using the mentioned framerate and τ, an A-scan number of e.g. 1000 A-scans per B-scan would require a camera speed of 400 kHz.

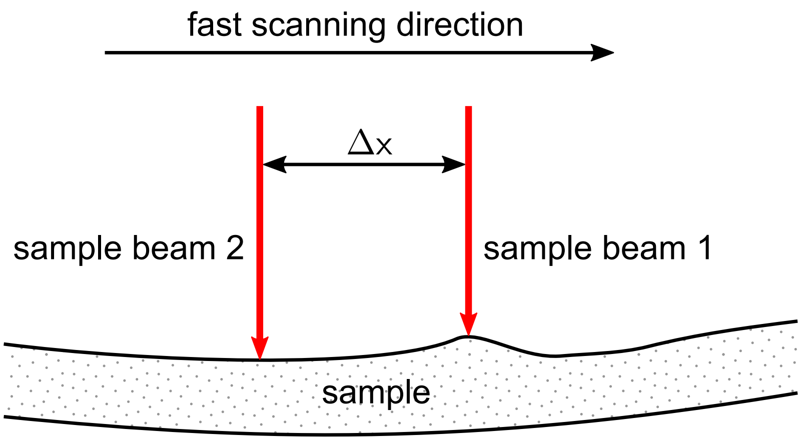

Figure 5.1: Illustration showing two sample beams with a fixed offset Δx scanning over a sample tissue.

to allow for the coupling of the OCT system with a DVA rodent system (see section 4.1.3). A schematic drawing of the dual beam setup's interferometers is shown in Fig. 5.2. Although it is shown as a black box in the illustration, the RVA is combined with the dual beam OCT system in the same way as was done with the single beam OCT system (see section 4.1.3). In contrast to the setup by Zotter et al. [106], the system that was built in the course of the work at hand uses only one light source for both interferometers (see Fig. 5.2).

The light source, the set-up and functionality of the spectrometers as well as the system parameters of the dual beam OCT system are identical with those explained in section 4.1. In addition, the interferometers of the dual beam setup are almost the same as the one of the single beam setup (see 4.1.2). There are only a few differences in the setup of the reference arm and the sample arms, which will be described in the following.

Interferometers

The light entering the setup through the fiber collimator FC1 is split into two beams by the 50:50 beam splitter BS1, as illustrated in Fig. 5.2. The resulting partial beams are then split again by the 50:50 beam splitters BS2 and BS3 of the two interferometers.

Both reference beams pass their own NDF and are then combined by BS4 and share the same reference arm, which includes the following optical components: a DC, the mirrors M6, M7 and the reference mirror M8. To avoid any cross-talk between the reference beams from the two interferometers, they are adjusted approximately 5 mm apart from each other, so that they cannot couple into the wrong fiber collimator. The reference beam of the first interferometer (continuous red line in Fig. 5.2) double

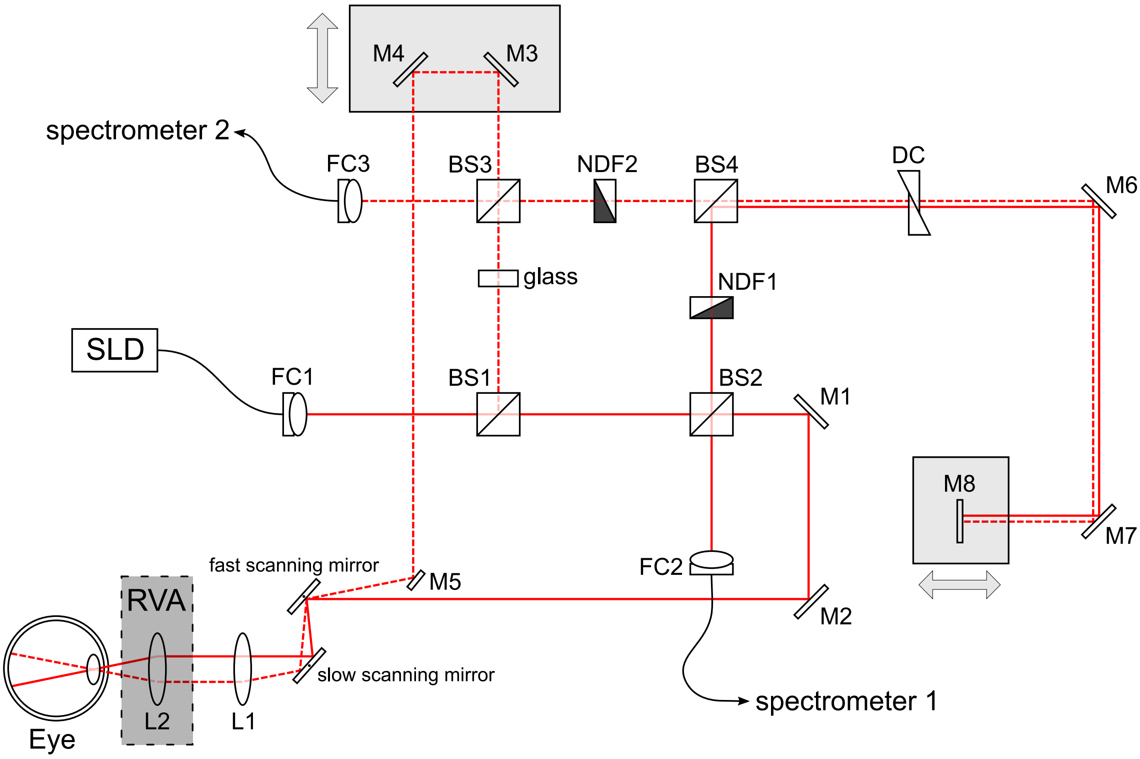

Figure 5.2: Schematic drawing of the dual beam OCT setup's interferometers. SLD = super luminescent diode, FC = fiber collimator, BS = beam splitter, M = mirror, NDF = neutral density filter, DC = dispersion compensation, L = lens, RVA = retinal vessel analyzer.

passes the reference arm and is coupled into FC2. The backreflected reference beam of the second interferometer (dashed red line in Fig. 5.2), on the other hand, is coupled into FC3. Each of the two fiber collimators FC2 and FC3 is connected to a spectrometer via a single mode fiber, as can be seen in the photograph of the setup in Fig. 5.3.

In contrast to the combined reference arms, the two sample arms are completely separated. The sample beam of the first interferometer is illustrated in Fig. 5.2 as continuous red line passing the following optical components: the beam splitter BS2, the mirrors M1, M2, the galvo-scanner (cf. fast and slow scanning mirror in Fig. 5.2), the lenses L1, L2 and the sample. The second interferometer's sample beam is indicated as dashed line passing BS3, M3, M4, M5, the galvo-scanner, L1, L2 and the sample. The mirrors M3 and M4 are mounted on a translation stage, which can be manipulated to change the second sample arm's length. Since the setup has only one reference arm, it is necessary to ensure that both sample arms have an identical length, or else it is not possible to acquire two identical depth profiles (A-scans) at the same sample position at different time points using two separate interferometers. Furthermore, the mirror M5 is mounted on a rotational stage, which is fixed upon an x-y translation stage. Thus, the angle between the

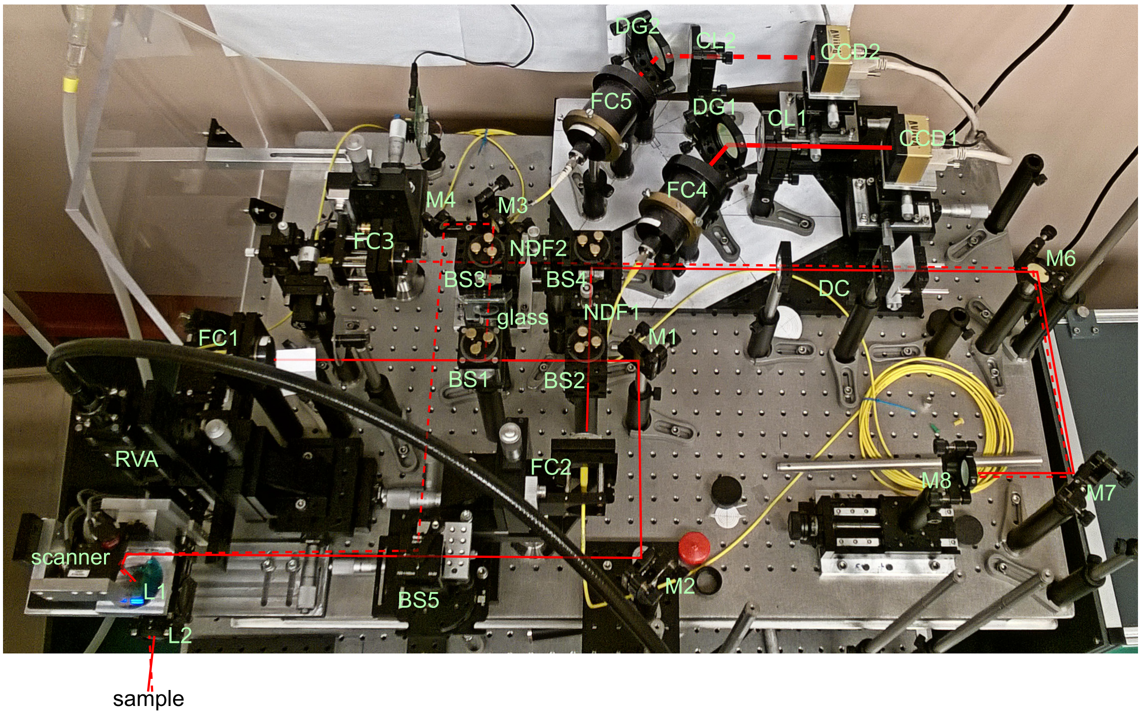

Figure 5.3: Photograph of the complete dual beam setup including both spectrometers.

two sample beams can be changed by rotating or moving M5. For reasons explained in the section on the adjustment, the mirror M5 was, at some point, replaced by another beam splitter BS5, which was mounted in the same way as M5 (see the photograph in Fig. 5.3).

In order to avoid cross talk between the two interferometers, a glass plate was inserted between BS1 and BS3. The optical path of the light passing through the glass plate is longer than the optical path between BS1 and BS2, i.e. sufficient glass between BS1 and BS3 ensures that the beams arriving at BS2 and BS3 are not coherent anymore. Thus, the two sample beams cannot interfere with each other, and there will be no cross talk between the two interferometers.

Adjustment

To calculate a phase difference tomogram from two consecutive B-scans, recorded by two separate interferometers, both sample beams have to scan over the exact same sample position but with a constant temporal delay in the fast scanning direction, which can be varied by changing the angle between the two sample beams via M5 (or BS5). It proved to be difficult to get M5 close enough to sample beam 1 without shadowing parts of the same. Hence, M5 was replaced by another beam splitter BS5 (see Fig. 5.3), even though this reduced the beam power of both sample beams by

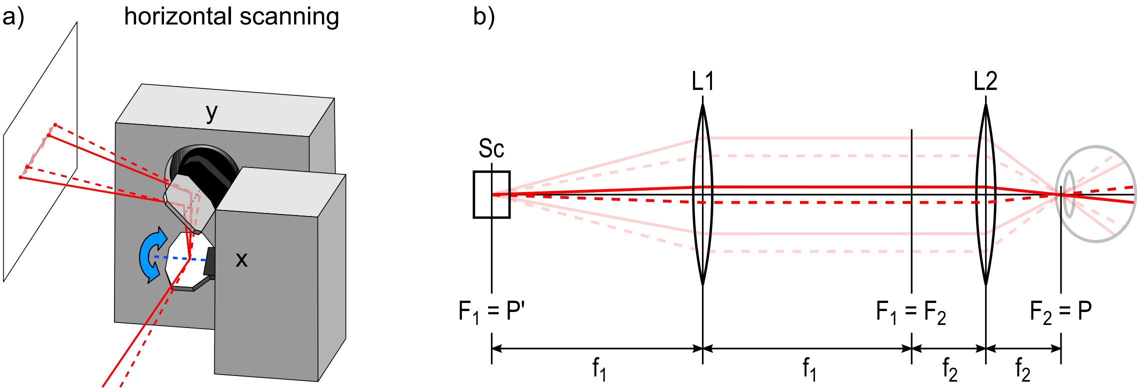

Figure 5.4: Scanning geometry of both sample beams. a) Both sample beams are reflected off the same point of the fast axis galvo-scanner. b) The beams' paths through the lens system while scanning is performed: the pivot-point of the fast axis scanner is in the second pupil plane P', which coincides with the focal point of L1 (adapted from [21]).

50 %. However, it allowed positioning both beams as close together as needed to achieve the desired offset of 2.5 ms or 44 A-scans, since the acquisition of one A-scan took 57 µs.

The sample beams were adjusted to be reflected off the same point on the pivot-axis of the fast scanning mirror, as shown in Fig. 5.4 a). The pivot-point of the fast axis scanner coincides with the focal point of L1, therefore both beams can pivot in the pupil plane of the sample eye (see Fig. 5.4 b)). If one of the sample beams is not directed onto the fast axis scanner's pivot-point, the motion of the scanning mirror will induce a phase shift in the signal that is measured by this sample beam.

Additionally, the spectrometers need to be adjusted carefully, so that they record identical spectra if they are connected to the same interference signal. Ideally, the CCD cameras of both spectrometers should have a pixel to pixel correspondence, which means that the wavelength λ_n should be imaged on the n-th pixel of both spectrometers' CCD cameras. A slight translational shift of one camera with respect to the other camera along the CCD array's length leads to λ_n being imaged on the $(n + \delta n)$-th pixel of the misaligned camera, which results in a shift of the recorded spectrum with respect to the other one. Subsequently, this leads to a phase shift of the Fourier transformed A-scan, which is proportional to the spectral shift and the sample layer depth [110].

To achieve a pixel to pixel correspondence in both spectrometers, an interference signal was split using a 50/50 fiber splitter and the resulting partial signals were connected to the two spectrometers[iii]. Afterwards, the spectrometers were manually adjusted by changing the position and the rotation of the first spectrometer's CCD camera, so that both spectra looked exactly the same on the *A-scan spectra* display of the data acquisition program (see Fig. 4.16 upper left display). Once the matching of the two spectra could not be improved any further by manual adjustment of spectrometer one, the rescaling parameters of channel one, which correspond to the newly aligned CCD camera, were varied for fine adjustment. After that, each interferometer was connected to its own spectrometer. Thereafter, the reference arm was blocked out and the interference signal between the backside of a microscope glass slide and a mirror mounted directly after the glass slide on a translation stage was used for the next fine adjustment step, since this setup yielded a dispersion-free interference signal. Then, the length difference between mirror and the glass slide was set close to zero, and afterwards, to a larger length difference leading to a higher interference modulation frequency. At both settings, the rescaling parameters of channel one were changed in such a way that the spectrum acquired by CCD1 matched the one recorded by CCD2. This is a very time-consuming procedure.

[iii] At this point, the two independent spectrometers have already been aligned optimally.

5.1.2 Why is the dual beam setup not usable in practice?

As already mentioned in section 5.1.1, both interferometers of the dual beam setup share the same reference arm. Therefore, the two sample beams need to have exactly the same length. The second sample beam's length can be varied by manipulating the translation stage, on which the mirrors M3 and M4 are mounted (see Fig. 5.2 and Fig. 5.3). The adjustment of the second sample arm's length with respect to the length of the first sample arm is extremely sensitive, and thus, very time-consuming[iv]. Furthermore, this has to be done for every test animal, as the eye lengths vary slightly from rat to rat. In addition, the eye of one animal will almost never be exactly at the same distance to the RVA lens, as the eye of the previous animal, and a changed distance between eye and RVA lens will also introduce a length difference between the two sample arms.

Even though the dual beam system works in principle, the sample arm adjustment procedure is simply too time consuming to be used for in vivo experiments. This is due to the fact that the anesthesia cannot be prolonged indefinitely and even if the eyes are moistened constantly, they will eventually dry out. Consequently, the cornea will develop superficial injuries during long experiment times. An unclear cornea reduces the measurement quality gravely and it will degrade even further with ongoing measurement time, until it becomes impossible to acquire any useful data.

For these reasons, another technique using the simpler single beam OCT system but a more complicated scanner motion will be described in the following section.

[iv] It can take several hours until both sample arms have virtually the same length.

5.2 Segmented B-scan method to assess microcirculation

The segmented B-scan method is another option to achieve a time difference of $\tau = 2.5\,\mathrm{ms}$ between two consecutive B-scans, and thus, to assess the retinal microcirculation, without the need of ultra high speed cameras. Also, it can be implemented into a single beam OCT system, which can be adjusted much faster and easier than the afore mentioned dual beam setup. Consequently, only the sample arm of the first interferometer, and thus, the first spectrometer of the dual beam setup, which was described in section 5.1.1, were used for the experiments in the sections 5.3 and 5.5.

5.2.1 Description of segmented scanning

The segmented B-scan method that will be described in the following is based on the work of Grulkowski et al. [111]. The idea here is to acquire a certain number of consecutive B-scan segments consisting of several A-scans instead of whole consecutive B-scans, which also works well for CCD cameras with lower acquisition speeds of e.g. 20 kHz. The time difference between two consecutive segments can be varied by changing the number of A-scans per segment.

A segmented B-scan requires a more complex scanning protocol (see Fig. 5.5) than the one normally used for a B-scan in OCT (see Fig. 4.15). As shown in Fig. 5.5 a), there is a small saw-tooth on the rising ramp of the scanner function. A closer inspection of this small saw-tooth (see Fig. 5.5 b)) reveals that the fast scanning mirror moves constantly in one direction for a certain time, which is referred to as one B-scan segment. Then, the scanning mirror “jumps” back half the way, thereafter follows another B-scan segment. This is repeated several times to acquire an entire segmented B-scan (see Fig. 5.5 a)). The two red lines in Fig. 5.5 b) indicate the second half of a B-scan segment as well as the first half of the subsequent B-scan segment, and they represent the same scanning position at different time points. The two data-sets that are recorded at this position starting at the time points A and B, respectively, can be subtracted from each other to calculate the corresponding phase difference half B-scan segment. The time period between the starting points A and B was set to $\tau = 2.5\,\mathrm{ms}$, this value can be changed via the number of A-scans per B-scan segment.

To achieve the time period of $\tau = 2.5\,\mathrm{ms}$, one B-scan segment was set to 4.1 ms or 72 A-scans, as the acquisition of an A-scan takes 57 µs. Consequently, the red line in Fig. 5.5 b) corresponds to 36 A-scans (half the B-scan segment). Considering that the galvo-scanner requires some time to move back half a B-scan segment, this

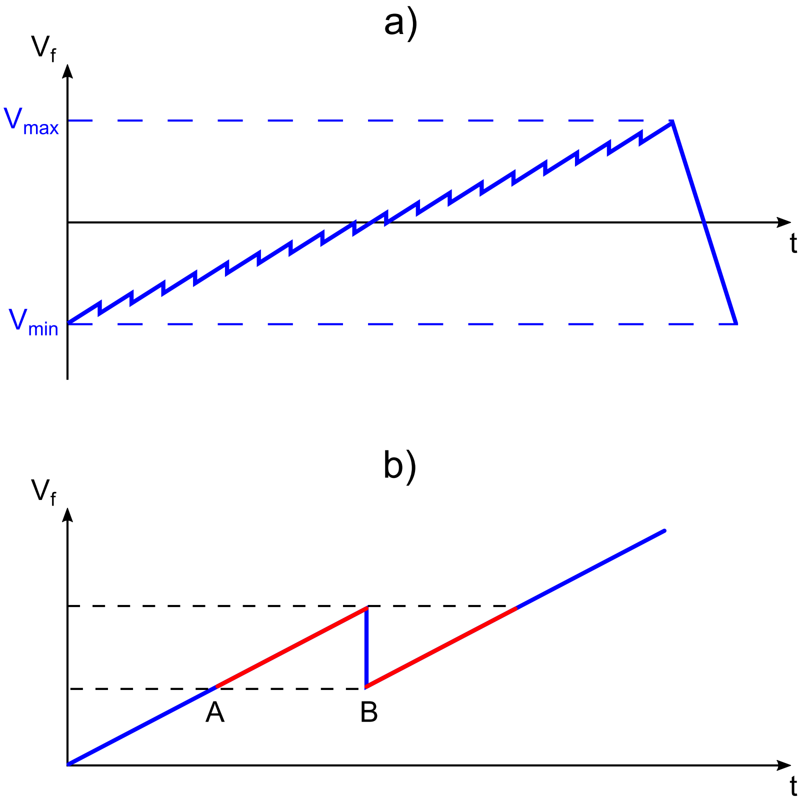

Figure 5.5: a) Saw-tooth scanner function of the fast axis galvo-scanner of one segmented B-scan; the segments are shown as small saw-tooth on scanner function's rising ramp. b) Close-up of two adjacent scanning segments. The red lines indicate that the sample beam is scanned exactly over the same sample position, staring at the different time points A and B.

backwards movement was set to 8 A-scans. Hence, 44 A-scans are recorded between the time points A and B (see Fig. 5.5 b)), which takes approximately 2.5 ms. The settings that were used for the experiments described in section 5.5 were 26 B-scan segments, and thus, 25 backward "jumps" of the galvo scanner per segmented B-scan, which sums up to 2072 A-scans. The second half of the last B-scan segment is not needed for the calculation of the phase difference B-scan, hence, only 2036 A-scans need to be recorded. Therefore, the CCD camera (Atmel, AViiVA M2 CL 2014) is sufficient to acquire such segmented B-scans, as it is able to record a maximum of 2048 lines during one scan. After those 2048 lines the memory of the camera board is full and the data need to be copied to the PC's memory.

The post processing steps between the read out of the saved spectral data and the Fourier transformation of the the rescaled and dispersion compensated spectra have already been described in section 4.3.2. In the subsequent step, the first half B-scan segments (see Fig. 5.5 b, the red line starting at A) are separated from their corresponding consecutive B-scan segments (see Fig. 5.5 b, the red line starting at B), which results in two amplitude and two phase tomograms (see Fig. 5.6 b), c)) that

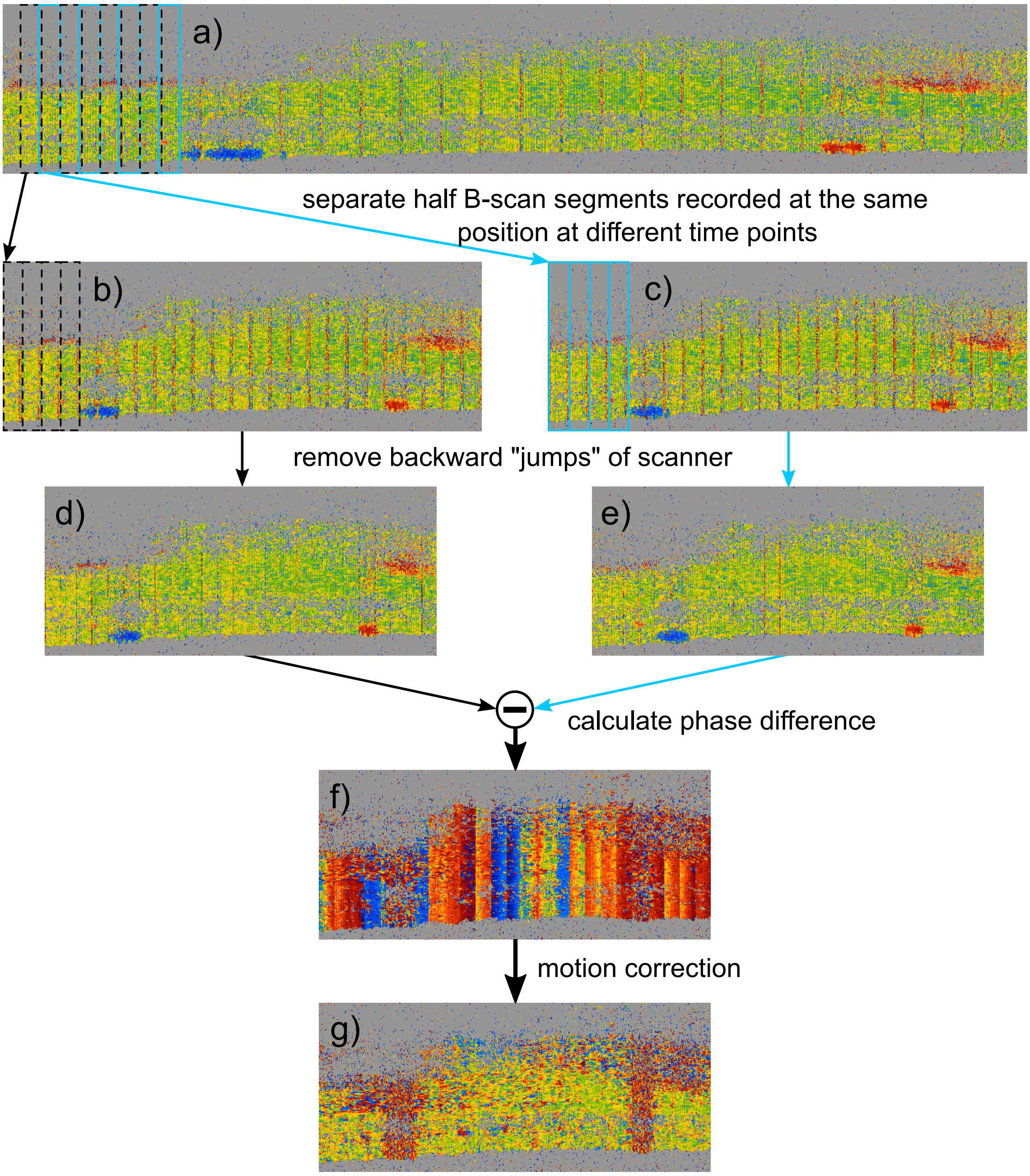
a)
separate half B-scan segments recorded at the same position at different time points
b)
c)
remove backward "jumps" of scanner
d)
e)
calculate phase difference
f)
motion correction
g)

Figure 5.6: The images a) - e) were created using the adjacent A-scan method (see section 4.3.2), for better visualization of the steps between the acquired segmented B-scan a) and the calculated phase difference tomogram f). However, actually, the raw phases of the unthresholded Fourier transformed data were used to calculate the phase difference tomogram f). Image b) consists of the half B-scan segments (see red lines in Fig. 5.5 b)) that were acquired at first, where image c) is composed of the consecutive half B-scan segments. The removal of the fast axis scanner's backward "jumps" yields the images d) and e). A histogram based linewise motion correction of the phase difference tomogram f) finally gives image g).

were recorded at the same position with a time difference of $\tau = 2.5\,\mathrm{ms}$. Thereafter, the fast axis scanner's backward "jumps" are removed from the tomograms (the same is done for the amplitude tomograms). Calculating the difference of the resulting tomograms (see Fig. 5.6 d), e)) yields the phase difference tomogram, displayed in Fig. 5.6 f). Furthermore, it should be mentioned that a threshold with respect to the combined consecutive amplitude tomogram, which is calculated from the corresponding segmented B-scans' amplitude tomograms is applied to the phase difference tomogram, before it is displayed on the front panel.

Since the technique described in this section is capable of measuring very low velocities, naturally, it is more susceptible to sample motions and system vibrations than the conventional Doppler OCT method, as can be seen in Fig. 5.6 f). Consequently, a histogram based motion correction was implemented in the post processing Labview program, in order to remove those motion artifacts, as done by Zotter et al. [106]. In the following, this motion correction method will be explained shortly: at first, it has to be assumed that more static tissue than capillaries is observed, and that there are no motion or vibration induced phase changes along a single A-scan, i.e. all phase changes along a single A-scan are due to moving red blood cells. Furthermore, the histogram for each A-scan of the phase difference tomogram is calculated and should reveal global phase shifts between the consecutive B-scans in the current A-scan. Then, the histograms' maximum values are subtracted from each pixel of the phase difference tomogram's corresponding A-scans. Applying this motion correction to the phase difference tomogram that is shown in Fig. 5.6 f), gives the motion corrected tomogram displayed in Fig. 5.6 g), which is then saved to the HDD.

5.3 In vitro experiments using the segmented B-scan method

The segmented B-scan method had to be tested thoroughly in several in vitro tests, before it was used to assess the retinal microcirculation in living animals, as not to sacrifice any test animals unnecessarily.

5.3.1 Artificial eye

The first in vitro test was the measurement of an artificial eye, which is basically a lens that focuses the sample beam onto a static piece of paper with lines drawn onto it[v]. Even though, a static sample does not induce any phase shifts in the sam-

---

[v] The areas with the drawn lines absorb more light of the sample beam than the blank paper. Consequently, these areas appear shadowed in the OCT tomograms. An example with two shadowed areas is shown in Fig. 5.7.

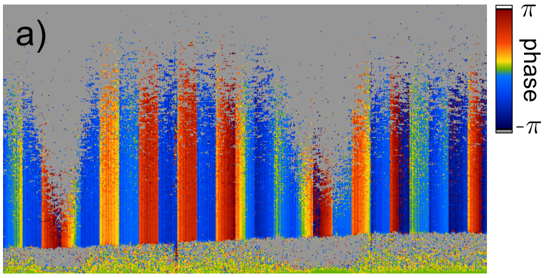

Figure 5.7: This figure shows a segmented phase difference B-scan of the artificial eye before a) and after b) linewise motion correction.

ple beam, the segmented phase difference tomogram that is displayed in Fig. 5.7 a) shows strong phase shifts, which occurred during the 2.5 ms between the consecutive B-scan segments. As already mentioned in section 5.2.1, these phase shifts can be explained by vibrations of the static sample, as well as by vibrations of the interferometer's optical components. The motion correction, which has been explained in the previous section, is capable of removing these vibrations (at least in a static sample), so that one gets the motion corrected phase difference tomogram that is displayed in Fig. 5.7 b). As expected, the motion corrected segmented phase difference tomogram of a static sample has no phase shifts whatsoever, and thus, appears greenish-yellowish in the false color phase display.

However, by the use of a pneumatic dampening system for the optical table, on which the OCT setup is built-on, the phase shifts due to the setup's vibrations can be reduced considerably, as can be seen in Fig. 5.8.

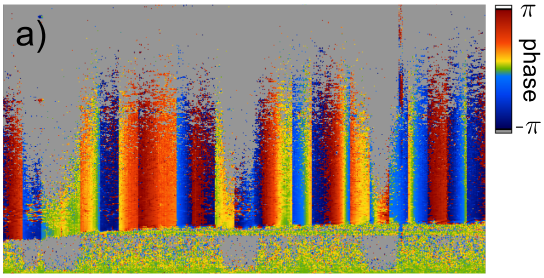

Figure 5.8: This figure shows two segmented phase difference B-scans of the artificial eye that were recorded at the same position, one before a) and one after b) the activation of the pneumatic dampening system.

5.3.2 Rotating disk

In the second in vitro test of the segmented B-scan method, the sample beam was scanned over the surface of a rotating cardboard disk. This is in contrast to the rotating disk experiment that was described in section 4.2.1, where the disk was

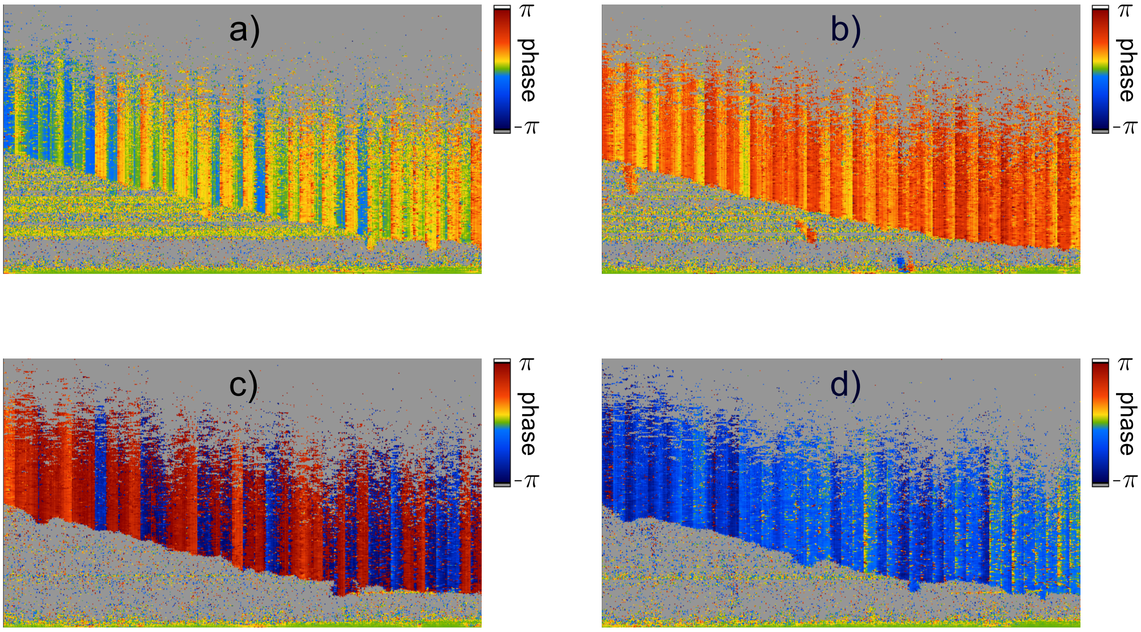

Figure 5.9: The rotating cardboard disk was measured with the segmented B-scan method with a time difference of 1.5 ms, at several different rotation speeds. The phase difference tomograms a)-d) correspond to four different disk rotation speeds.

illuminated with a static sample beam. However, it was difficult to quantify the results of these measurements, as the velocities varied over one B-scan due to the scanning of the sample beam over the disk surface[vi]. Additionally, the velocity information in the phase difference tomogram was overlain with phase shifts that were induced by the system's vibrations, even though, the pneumatic dampening was activated. Furthermore, the motion correction could not be used to remove these vibrations, as it would also have removed the desired phase shifts corresponding to the disk rotation. Nevertheless, it can be seen in Fig. 5.9 that increasing rotational disk speeds result in higher phase shifts, where Fig. 5.9 a) corresponds to the lowest and Fig. 5.9 d) to the highest disk velocity of the four displayed measurements. The phase difference tomogram Fig. 5.9 c) shows phase wrapping of a few B-scan segments, while Fig. 5.9 d) shows phase wrapping of all B-scan segments.

[vi] The rotating disk's tangential velocity v_{disk}, its longitudinal velocity component $v_{\mathrm{disk,L}}$ (see Fig. 4.11), and thus, the detected phase shift equal zero at the center of the rotating disk, and increase with the radius to the measurement point. Consequently, a B-scan recorded by scanning the sample beam over the rotating disk in a straight line yields lower phase shifts for the lines corresponding to scanning positions with smaller radii, and higher phase shifts for the lines corresponding to scanning positions with larger radii.

5.3.3 Glass capillary

In order to simulate a retinal vessel, a glass capillary was measured using the segmented B-scan method. The were only two differences between this experiment and the one described in section 4.2.2: firstly, a segmented scanning protocol (cf. Fig. 5.5) was used to acquire OCT data, and secondly, lower flow velocities in the capillary, ranging from 0 mm/s to 1.8 mm/s, were set. The Doppler angle between sample beam and glass capillary is approximately 85° and it was unclear how accurate the syringe pump would be at flow rates below 1 mm/s. Therefore, a time difference between two consecutive B-scans of $\tau = 1\,\text{ms}$ was used, to be able to measure velocities of up to 1.8 mm/s without encountering any phase wrapping artifacts[vii].

Even with turned off syringe pump, sample movements were visible in the phase difference tomograms (see Fig. 5.10), which were supposedly due to Brownian movements of the fat globules in the milk water dilution in the glass capillary. This theory is supported by the fact that the Brownian movements can have velocities of up to 1 mm/s [112, 113].

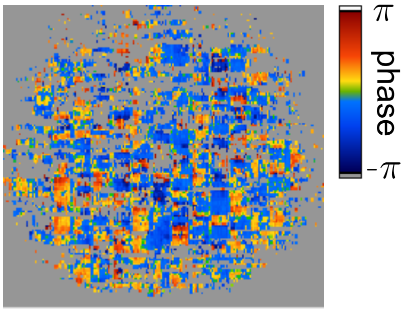

Figure 5.10: Segmented B-scan of a capillary, filled with a milk-water-dilution. The flow velocity of the sample fluid was zero, as the syringe pump was switched off.

However, after unwrapping the capillary data, using a low threshold, the unwrapped capillary tomograms of the segmented B-scan stack were averaged and the capillary's mean phase shift was calculated (cf. blood vessel evaluation in section 4.3.2). Doing this for different flow velocities, yielded a linear relationship between the velocities in the capillary and the calculated mean phase values of the averaged segmented B-scan stacks, which can be seen in Fig. 5.11. The syringe pump was quite inconsistent at low velocities and did over and under shoot the set velocities, which is one possible explanation for the outliers at 0.5 mm/s and at 1 mm/s. Additionally, the detected phase shifts are overlain with system vibrations that cannot be removed by the motion correction, as it would also remove the phase shift, induced by the flow velocity of the sample fluid. Due to these overlain vibrations and the unwrapping of

---

[vii] For $\tau = 2.5\,\text{ms}$ and a Doppler angle of 85°, it is only possible to detect velocities of up to 0.7 mm/s without phase wrapping.

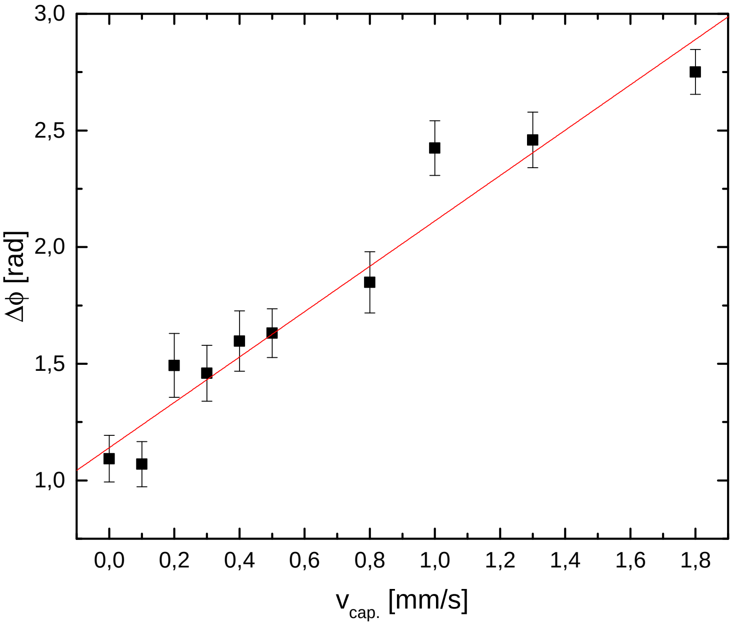

Figure 5.11: In this plot, the mean phase difference values, calculated from the segmented B-scan stacks of one capillary measurement, respectively, are plotted over the velocity $v_{\text{cap.}}$ inside the glass capillary.

the Brownian motions, the phase shift values do not go down to zero, or at least to the phase noise, for $v_{\text{cap.}} = 0\,\text{mm/s}$. Nevertheless, the calculated mean phase shift values are highly linear correlated to the actual velocity $v_{\text{cap.}}$ inside the capillary (see Fig. 5.11; the correlation coefficient was calculated to be 0.9738).

These results confirm the segmented B-scan method's capability of measuring flow velocities as slow as the blood flow velocities actually occurring in the retinal capillaries ($0.5 - 2\,\text{mm/s}$, [101–105]), at least inside a glass capillary.

5.4 New data evaluation

As already mentioned at the beginning of this chapter, the retinal capillaries have diameters in the range of 5 µm [100], thus, they have sizes of a few pixels, or even of single pixels in the calculated phase difference tomograms, while they cannot be seen in the amplitude tomograms. Therefore, the vessel evaluation method that is described in section 4.3.2 cannot be used to evaluate blood flow velocity changes in the retinal microcirculation. Consequently, a new evaluation method had to be developed, which will be described in the following.

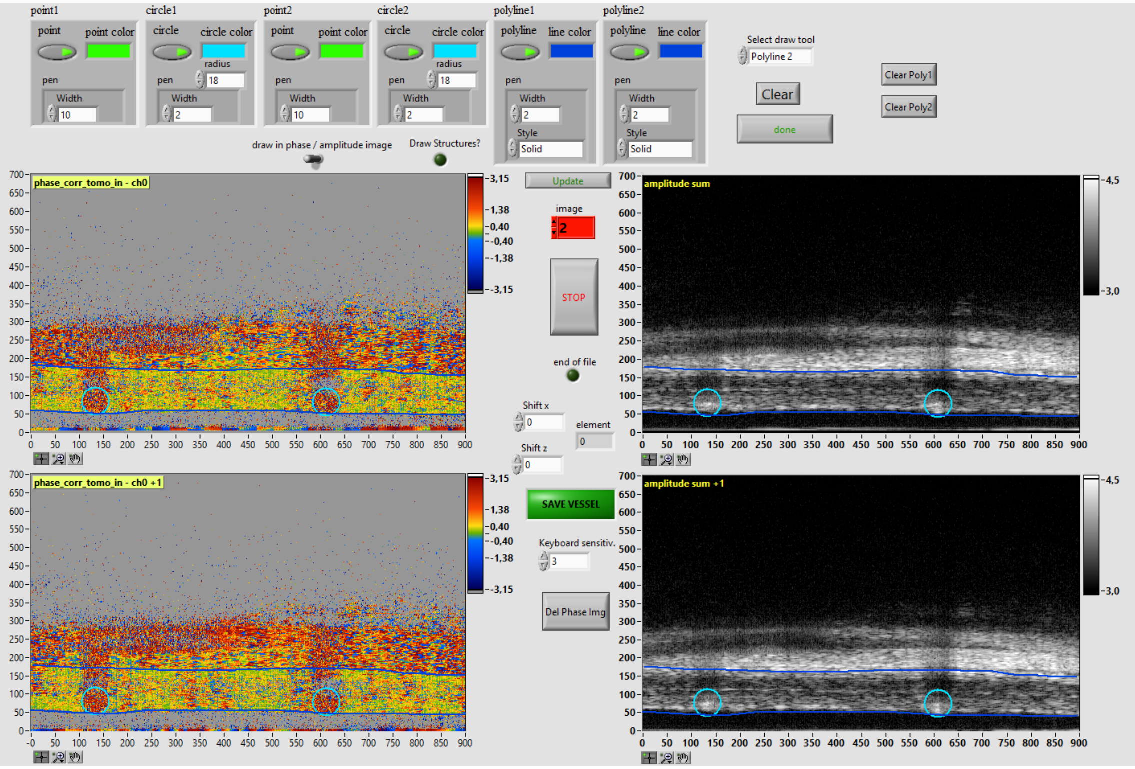
point1
circle1
point2
circle2
polyline1
polyline2
point
point color
circle
circle color
radius
18
polyline
line color
pen
Width
10
2
Style
Solid
Select draw tool
Polyline 2
Clear
done
Clear Poly1
Clear Poly2
draw in phase / amplitude image
Draw Structures?
phase_corr_tomo_in - ch0
phase_corr_tomo_in - ch0 +1
amplitude sum
amplitude sum +1
Update
image
2
STOP
end of file
Shift x
0
Shift z
element
SAVE VESSEL
Keyboard sensitiv.
3
Del Phase Img
3,15
1,38
0,40
-0,40
-1,38
-3,15
4,5
-3,0
0
50
100
150
200
250
300
350
400
450
500
550
600
650
700
750
800
850
900

Figure 5.12: This image presents a screenshot of the Labview image registration program. The controls at the top can be altered to change the appearance of the structures that can be drawn into the upper phase or amplitude image. The upper displays show a phase difference tomogram and its corresponding amplitude tomogram of one segmented B-scan, while the two lower displays show phase difference and amplitude tomogram of the subsequent segmented B-scan.

5.4.1 Histogram based evaluation method

The segmented phase difference tomograms of an OCT measurement are calculated as explained in section 5.2.1, afterwards, they are saved to the HDD. Before these phase images can be evaluated any further, they need to be registered, in order to remove shifts in z in x-axis (axial or transversal to the sample beam) between two adjacent phase difference images. These small translational shifts can mostly be reduced to respiration induced movements of the test animal's head.

At first an automatic phase image registration via the program "ImageJ" was attempted, however, this approach did not provide the desired accuracy and sometimes did even worsen the problem. Therefore, a Labview program for manual image registration was written in the course of this work. A screenshot of this program is presented in Fig. 5.12. The registration program loads the phase difference image and the corresponding amplitude image of a segmented B-scan into the upper two

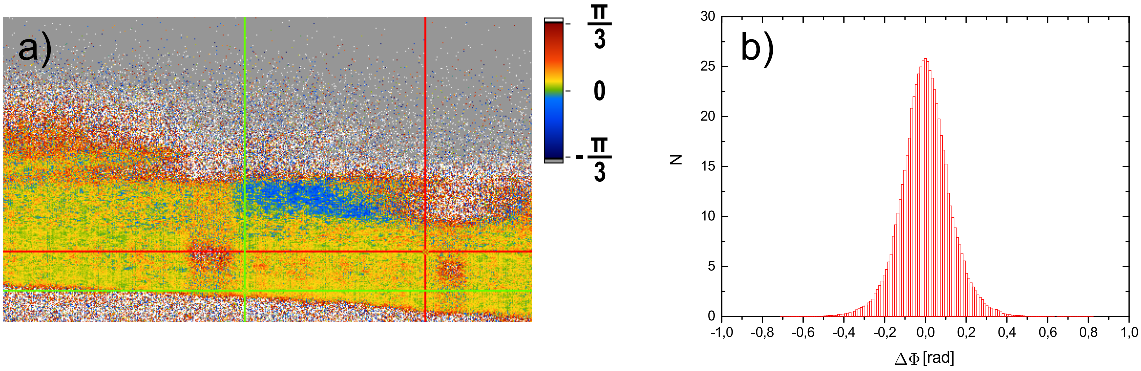

Figure 5.13: Image a) shows an averaged segmented phase difference tomogram of an OCT measurement. Between the two large vessels, an ROI has been selected by red and green cursors. The histogram calculated from this ROI is displayed in image b).

displays, and the phase difference as well as the amplitude image of the subsequent segmented B-scan into the two lower displays. For better visual comparison, structures like dots, circles and poly lines can be drawn into the upper phase or amplitude display, and are then visible in all four displays. The tomograms in the two lower displays can be shifted in x or z direction, with respect to the upper images, via the cursor keys. Once the shift is compensated, the changes can be saved directly to the opened file by hitting the space-bar. Thereafter, the program loads the next image pair. This procedure is repeated until the end of the segmented B-scan stack is reached. If the motion correction did not remove all sample motion artifacts in one phase difference tomogram, every pixel of the whole phase image could be set to -100, and thus be excluded from the averaging in the next evaluation step, by pressing the delete key before saving the changes.

Afterwards, all registered phase difference images of a whole segmented B-scan stack are averaged[viii], and an ROI for the histogram calculation is selected via four cursors, as shown in Fig. 5.13 a). Then, a histogram of all datapoints in this ROI, except for the ones with -100 values, is calculated (see Fig. 5.13 b)). In order to get a smoother histogram without using a large histogram bin width, which would decrease the accuracy of the FWHM, eight histograms with slightly shifted origins of bins are averaged [40, 77]. Thereafter, the FWHM of the averaged histogram is calculated to quantify changes in the histogram width.

[viii] All -100 values are excluded from the averaging process, as they would severely distort the pixel mean values of the resulting averaged phase difference image, due to the fact that all original phase values are in the range of $\pm\pi$.

5.4.2 Histogram simulation

As shown in Eq. (3.74), the measured phase difference $\Delta\phi$ is proportional to the velocity of the moving red blood cells. Therefore, one can say that the FWHM of the histogram, which is calculated from the chosen ROI of the average phase difference tomogram, corresponds to the mean blood flow velocity within the capillaries that are supplying the tissue under study and to the random phase noise of the OCT system. Hence, an increase of the blood flow velocities within the capillaries under study will lead to a broadening of the histogram, while a decrease of their blood flow velocities will lead to a narrowing of the histogram. However, this correlation can only hold true, if a sufficient high number of datapoints in the chosen ROI, correspond to retinal capillaries.

For further investigation of the relationship between the histogram width and the change of the blood flow velocities in the retinal capillaries, a simulation program was written in Labview. The program creates a phase image with a Gaussian noise pattern similar to the one of a living animal, which results in a histogram width of $\mathrm{FWHM}_{\mathrm{noise}} \approx 0.16\,\mathrm{rad}$. Furthermore, by changing the variable n, it can be chosen how many percent of the available datapoints are replaced by velocity values of the simulated capillaries. Additionally, the velocity range as well as the Doppler angle range have to be set before the simulation can be started. To quantify the actual change of the histogram width due to the velocities in the capillaries, the difference between the FWHM of the histogram corresponding to the set velocity range and the noise histogram was calculated:

$$\Delta\mathrm{FWHM} = \mathrm{FWHM}_{\mathrm{vel.}} - \mathrm{FWHM}_{\mathrm{noise}}. \tag{5.1}$$

The results of a simulated B-scan with six different numbers of simulated capillaries (six different n settings) in the chosen ROI, at five different maximum capillary velocities, are plotted in Fig. 5.14. As can be seen, this relationship becomes more linear with increasing n. This effect is understandable, as for a low number of capillaries, many pixels with random phase noise will contribute to the histogram, and thus, the histogram's broadening due to the velocities in the relatively small number of capillaries will be marginal. It should be mentioned that for the simulation, whose results are presented in Fig. 5.14, it was assumed that the simulated capillaries are all in one layer that is almost perpendicular to the sample beam. Thus, a Doppler angle range between 89° and 91° was chosen for the simulation.

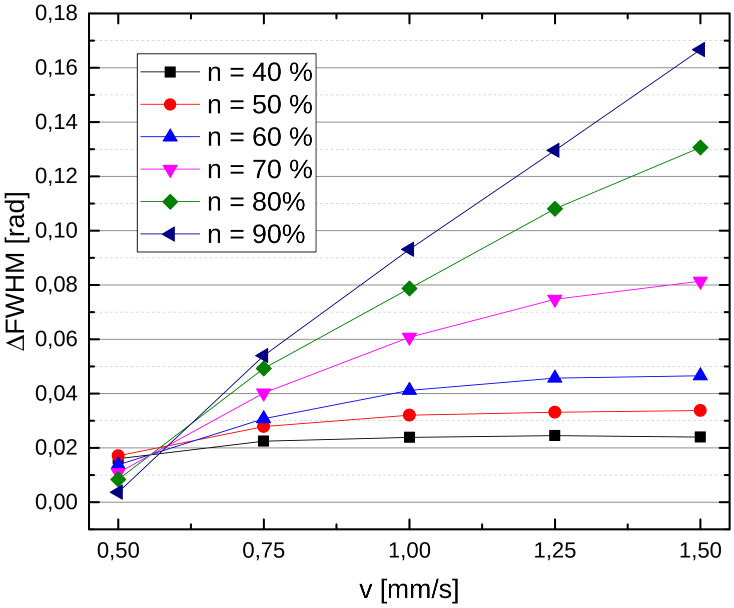

Figure 5.14: Results of the evaluated simulated microcirculation data. n indicates how many of the available datapoints in the evaluated ROI correspond to simulated capillaries.

5.5 In vivo measurements of the retinal microcirculation

In order to test whether the segmented B-scan method (see section 5.2.1) in combination with the histogram based data evaluation (see section 5.4.1) is capable of measuring relative changes in the blood flow velocities of retinal capillaries, a hyperoxia experiment similar to the one presented in section 4.4.2 was conducted.

For the in vivo experiments described in this section, a measurement position including one major retinal vein and one major retinal artery was chosen to be at a distance of about one to two diameters of the optic disk from the ONH. The area between the large vessels was used to assess the retinal microcirculation, while the large retinal veins were evaluated, to be able to verify the oxygen induced blood flow decrease in the measured animal, and compare the results to the microcirculation data.

The microcirculation data were evaluated as described in the sections 5.2.1 and 5.4. For the evaluation of the large vessels, the tomograms consisting of the first half B-scan segments (see section 5.2.1 and Fig. 5.6 for explanation) were used. The following calculation of the phase difference tomograms, as well as the blood vessel evaluation were done exactly as described in section 4.3.2.

A segmented phase difference tomogram consists of $N = 900$ lines and has a geometric width of $d \approx 1\,\mathrm{mm}$[ix]. Inserting these values together with the systems lateral resolution $\delta x = 11.3\,\mu\mathrm{m}$ (see section 4.1.5) into Eq. (4.23) yields an oversampling factor of $\mathrm{OF} \approx 10$. Each OCT measurement that was recorded to assess the retinal microcirculation, contains 100 consecutive segmented B-scans, so that possible flow irregularities due to heart beat related pulsatility are averaged out.

5.5.1 Animal preparation

The study was performed following the statement for the use of animals in ophthalmic and vision research of the association for research in vision and ophthalmology (ARVO) and was approved by the ethical committee for animal experiments of the Medical University of Vienna.

Eight male Sprague-Dawley rats with a body weight of 350 g to 400 g were used for the in vivo measurements. Anesthesia was induced with an intraperitoneal injection of 100 mg/kg ketamine and 5 mg/kg xylazine. The rats were intubated and ventilated with oxygen, air and 1.5 % – 2 % isoflurane, at a VF of 70/min, to maintain deep anesthesia. Furthermore, 3 mg/kg piritramide were applied subcutaneously for analgesia. To control the depth of the anesthesia, blood pressure and heart rate were monitored continuously. The right eye of each test animal was used for the measurements. In order to prevent the animal's eyes from drying-out and to maintain good imaging quality, the eye under study was continuously moistened with hyaluronic acid containing eye drops (Hylo-Comod, 1 mg/ml sodium hylauronat; Ursapharm, Saarbrücken, Germany). After completion of the experiments the animals were euthanized via a lethal injection of pentobarbital.

5.5.2 Experiment protocol

After the animal preparation that was described in the previous subsection, the animals were ventilated with ambient air for 10 min, using a constant VF (baseline conditions). Thereafter, the ventilation gas was changed to 100 % oxygen for another 10 min. At the end of the air breathing phase, as well as the oxygen breathing phase, three OCT measurements were recorded, each consisting of 100 segmented B-scans. The acquisition of a single segmented B-scan took 16 s. If necessary (e.g. due to bad signal quality, or clearly visible eye movements), a second hyperoxia experiment was

---

[ix] A segmented B-scan contains 26 B-scan segments, each consisting of 72 A-scans, and the scanner "jumps" back, half a B-scan segment, 25 times (see section 5.2.1). This yields $N = 26 \cdot 72 - 25 \cdot 36 = 972$ A-scans at a geometric width of $d = 1.1\,\mathrm{mm}$. Since the first and the last half B-scan segment are not used for the phase difference calculation, the resulting phase difference tomogram has only $N = 900$ A-scans, which corresponds to a geometrical width of $d \approx 1\,\mathrm{mm}$.

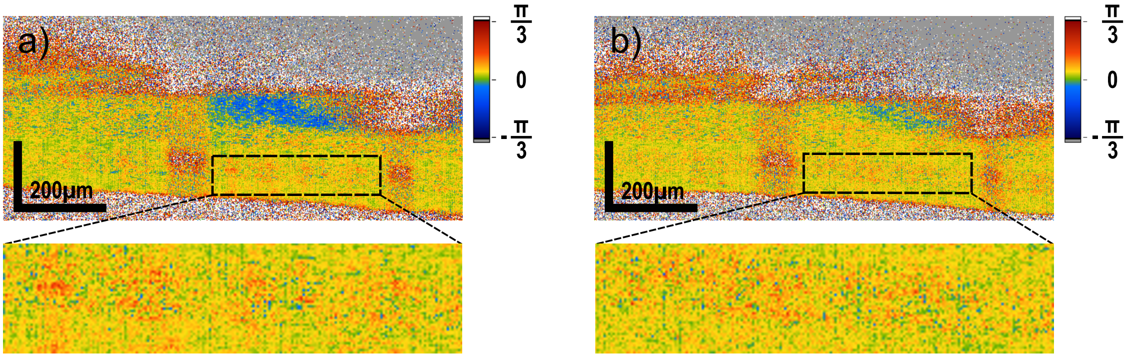

Figure 5.15: Phase images illustrating the oxygen induced blood flow velocity reduction in the retinal microcirculation of one rat. Both shown phase tomograms were averaged over a 100 segmented B-scan phase difference tomograms recorded at the same retinal position during the air breathing phase a) and after 10 min of 100 % oxygen breathing b), respectively.

conducted in the same animal, after a pause of at least 10 min, in which the animal was ventilated with 1.5 l/min ambient air and 0.8 l/min oxygen. After completion of all experiments and OCT measurements the animals were sacrificed. In every test animal, three additional OCT measurements were recorded 10 min after death. The animals eyes were moistened constantly, and in contrast to the vasoconstriction experiment described in section 4.4.2, they were also moistened during the whole air and oxygen breathing phase, especially shortly before each OCT measurement.

5.5.3 Results

The averaged phase difference tomograms, of an in vivo hyperoxia microcirculation experiment of one animal, which were acquired using the segmented B-scan method, are shown in Fig. 5.15. The left image (see Fig. 5.15 a)) was calculated from a dataset that was recorded during the air breathing phase, while the right image (see Fig. 5.15 b)) was calculated from a dataset, recorded at the same position during the oxygen breathing phase. Magnifications of the areas inside the dashed rectangles are displayed below the corresponding averaged phase difference tomograms. By comparing these two magnified phase image ROIs, one can see a decrease in the blood flow velocities of the retinal capillaries, where the values corresponding to the measurements recorded during the air breathing phase (see Fig. 5.15 a)) are higher than the ones corresponding to the measurements acquired during the oxygen breathing phase (see Fig. 5.15 b)).

The histograms shown in Fig. 5.16 (red bars and blue envelope curves) were calculated from the ROIs (indicated by dashed rectangles) of the averaged phase difference tomograms, which are depicted in Fig. 5.15. Furthermore, the histogram

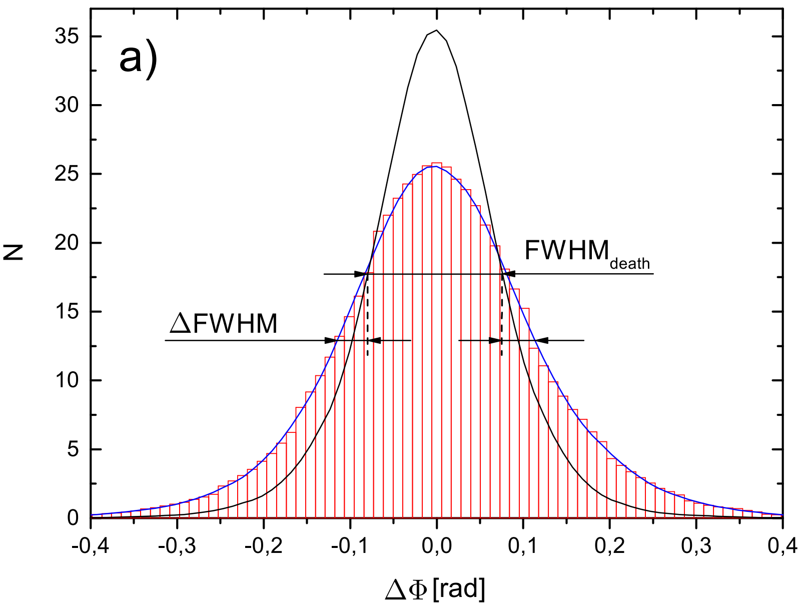

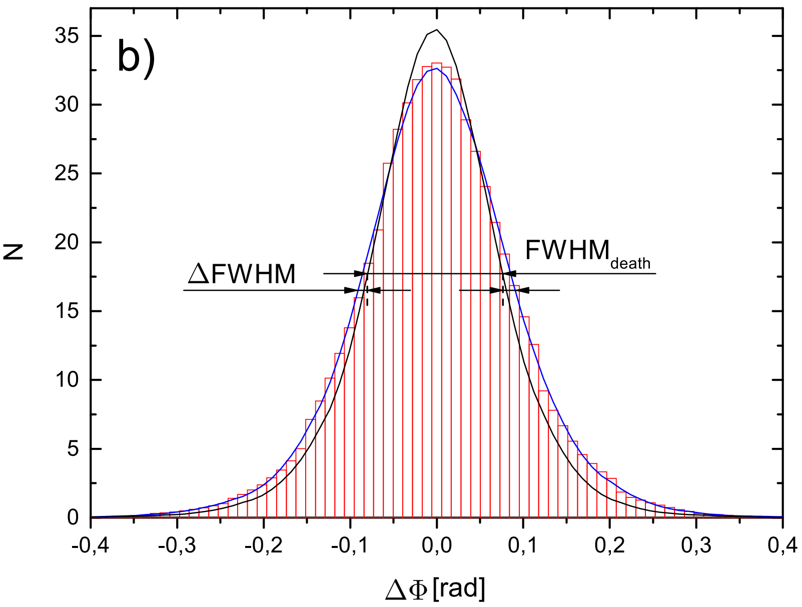

Figure 5.16: Phase histograms calculated from the ROIs in Fig. 5.15, where a) corresponds to the air breathing phase and b) to the oxygen breathing phase. The black curve and $\text{FWHM}_{\text{death}}$ correspond to the data recorded after the animal's death. Thus, $\text{FWHM}_{\text{death}}$ is in the range of the system's phase noise histogram's width. The calculation of ΔFWHM can be found in Eq. (5.2).

corresponding to the averaged phase difference tomogram of a measurement that was recorded after the animal's death is plotted as black curve in Fig. 5.16 a) and b). As done for the histogram simulation in section 5.4.2, the ΔFWHM was used to quantify relative changes of the histogram width. The ΔFWHM is indicated in Fig. 5.16 and calculates as follows (cf. Eq. (5.1)):

$$\Delta\mathrm{FWHM} = \mathrm{FWHM}_{\text{in-vivo}} - \mathrm{FWHM}_{\text{death}}, \tag{5.2}$$

where $\mathrm{FWHM}_{\text{in-vivo}}$ represents the FWHMs of the histograms corresponding to the data that were recorded during the air breathing phase as well as after 10 min of 100 % oxygen breathing. $\mathrm{FWHM}_{\text{death}}$ stands for the FWHM of the histogram corresponding to the data acquired after the test animal's death and is, thus, in the range of the phase noise ($\Delta\phi_{\text{err}}^{\text{avg}} = 0.18\,\text{rad}$). The mean $\mathrm{FWHM}_{\text{in-vivo}}$ and the mean $\mathrm{FWHM}_{\text{death}}$ of one animal experiment are shown in Fig. 5.17.

As expected, the oxygen breathing induced reduction of the blood flow velocities in the retinal capillaries leads to a narrower histogram than the data recorded during the air breathing phase (see Fig. 5.16). Similar results were obtained for all eight test animals, and the ΔFWHM was used as measure for the histogram widths. However, in three animals no reasonable $\mathrm{FWHM}_{\text{death}}$ could be acquired, by reason of bad imaging quality, which was probably due to the drying-out of the sample eye, as a consequence of too long experiment durations. Hence, the $\mathrm{FWHM}_{\text{death}}$ values of the other five animals were averaged, which yielded $\overline{\mathrm{FWHM}}_{\text{death}} = (0.16 \pm 0.02)\,\text{rad}$. This value was used for the calculation of the ΔFWHMs of the three animals, in which no reasonable $\mathrm{FWHM}_{\text{death}}$ could be acquired. As can be seen the $\mathrm{FWHM}_{\text{death}}$ range is very narrow, hence it might be possible to use this value for future experiments, so that it is not necessary to sacrificed every test animal to get a baseline value. This approach should of course be investigated in further experiments before using it in a new study.

Afterwards, the changes from baseline of the blood flow velocities in the capillaries as well as in the large retinal vessels were calculated for every test animal. Thereafter, the change from baseline values of all eight rats were averaged, and the resulting mean values ± SD are represented in Table 5.1 and Fig. 5.18, respectively. Compared to the baseline values, a decrease in the mean blood flow velocities of (48.2 ± 9.9) % for the microcirculation and (38.2 ± 14.3) % for the large vessels can be observed after 10 min of ventilation with 100 % oxygen.

The blood flow velocity value within the large retinal vessel of animal # 4 was excluded from the calculation of the average change from baseline in the large retinal vessels (see Table 5.1). This was necessary, since no reasonable change from baseline value could be calculated, as a consequence of a small movement of the sample eye, which resulted in a change of the Doppler angle between the sample beam and the measured vessel. Given that there was only a change in the Doppler angle but hardly any alteration of the scanning position on the retina, this did scarcely effect

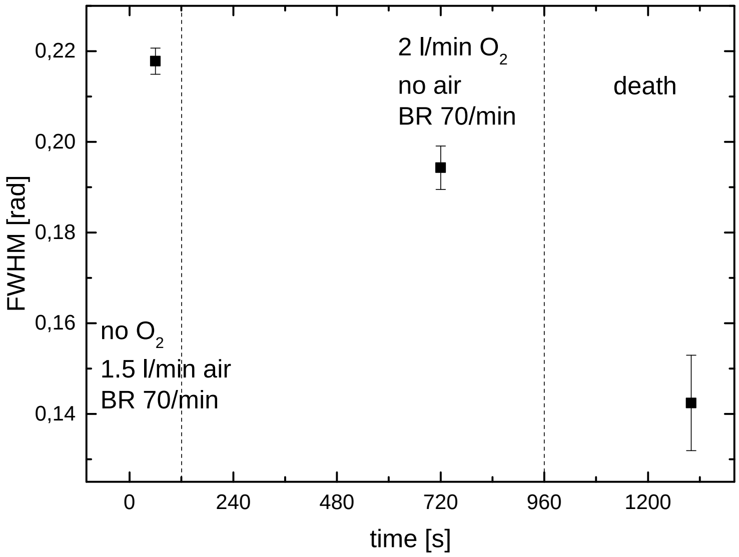

Figure 5.17: The exemplary results of one animal experiment are plotted in this graph. Every datapoint represents the mean FWHM ± SD of at least three histograms, calculated from as many different OCT measurements. From left to right: the first datapoint corresponds to the air breathing phase (baseline conditions), the second datapoint corresponds to the data that were recorded after 10 min of oxygen breathing and the last datapoint corresponds to the measurements, which were performed after the animals death.

Table 5.1: Relative changes in blood flow velocity due to oxygen breathing, as compared to base line conditions (air breathing) in the retinal micro vessels as well as in large retinal vessels. The blood flow velocity of animal # 4 is not shown in the table and was not included in the calculation of the mean value (see text for explanation).

Animal #	change from baseline [%]	
	microcirculation	large vessels
1	-60.2	-57.0
2	-56.5	-47.7
3	-36.7	-18.8
4	-46.7	–
5	-53.4	-23.2
6	-31.1	-32.0
7	-49.1	-50.3
8	-52.0	-38.6
mean ± SD	-48.2 ± 9.9	-38.2 ± 14.3

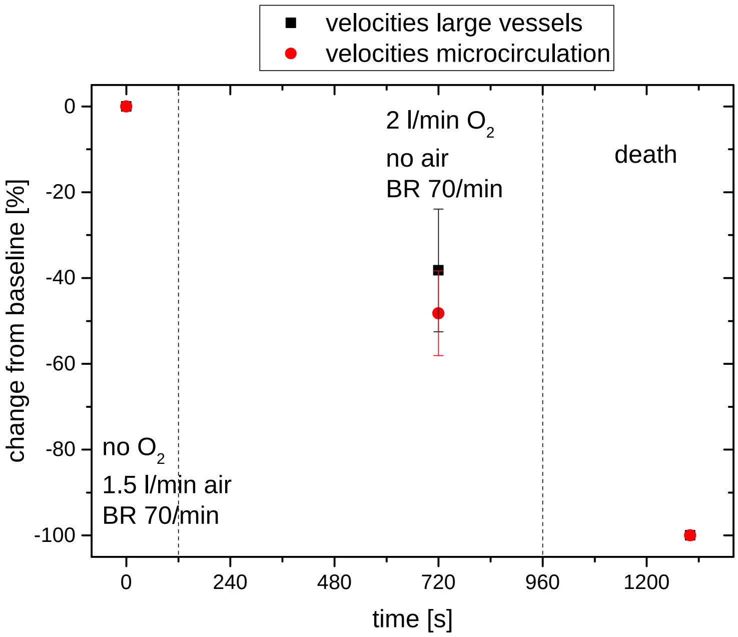

Figure 5.18: In this graph, relative changes in the mean blood flow velocities of the retinal microcirculation (red circles) and of large retinal veins (black squares) from baseline conditions, due to ventilation with 100 % oxygen, are plotted over the measurement time. The datapoints represent the mean changes from baseline ± SD of all 8 animals.

the histogram based microcirculation evaluation. One possible explanation for this behavior is the fact that the two retinal capillary layers consist of countless micro vessels, which are randomly oriented in many different directions, therefore, a change of the Doppler angle would not make much of a difference, if looking at a region including a large number of capillaries.

5.5.4 Discussion

As mentioned in connection with the histogram simulation in section 5.4.2, the relationship between the blood flow velocities in the retinal capillaries and the ΔFWHM of the histogram corresponding to these capillaries is only linear if almost all of the pixels in the evaluated cross-sectional area[x] correspond to capillaries (see Fig. 5.14). Consequently, this relation will most likely be non-linear for a real in vivo measurement, since in that case less than 100 % of the datapoints will correspond to a capillary. In order to calculate the actual relationship between ΔFWHM and the velocities in the retinal capillaries, it would be necessary to know the exact number of datapoints corresponding to capillaries in the ROI under study, which cannot be determined using the method that is presented in the work at hand. However, it is still true that the histogram broadens with increasing blood flow velocities in the capillaries, which is sufficient for the detection of relative velocity changes. Therefore, the results of the previously described in vivo experiments in eight animals are comparable with each other, assuming that the different test animals had comparable capillary densities at similar measurement positions.

---

[x] The evaluated cross-sectional area is the chosen ROI of the averaged phase difference tomogram, from which the histogram and subsequently the ΔFWHM is calculated.

A major drawback of the microcirculation assessment and evaluation method described in section 5.2 is the need for post mortem measurements to calculate the histogram width $\mathrm{FWHM}_{\mathrm{death}}$ of the OCT system's phase noise for in vivo measurements. One possibility to overcome this limitation is the measurement of the system's phase noise using the consecutive A-scan method (see section 4.3). If the evaluated retinal cross-sectional area contains only capillaries and no large vessels, and if the time period τ between two adjacent A-scans is sufficiently short (e.g. $\tau = 57\,\mu\mathrm{s}$, or shorter), the slow blood flow velocities in the capillaries cannot be detected. Thus, the resulting histogram width is in the range of the OCT system's phase noise, and, consequently, in the range of the histogram width corresponding to the data that can be acquired post mortem via the segmented B-scan method (see section 5.2). However, further experiments should be conducted to investigate, which τ values have to be used for the consecutive A-scan method to achieve similar phase noise histogram widths as the ones corresponding to the post mortem data that are acquired using of the segmented B-scan method.

Another limitation of the segmented B-scan OCT method is its sensitivity to sample motion, which is a common problem for Doppler OCT techniques. However, as already mentioned in section 4.4.4, the sample motion artifacts were minimal in the experiments conducted in the course of this work, as the test animals were anesthetized during the measurements.

Regrading the experimental results, the results of the hyperoxia experiment described in section 5.5 show a decrease of the blood flow velocities in the retinal capillaries of $(48.2 \pm 9.9)\,\%$, which fits the velocity decrease of $(38.2 \pm 14.3)\,\%$ in the corresponding large retinal veins (see Table 5.1 and Fig. 5.18). Furthermore, these results are in very good agreement with the outcome of the vasoconstriction experiment described in section 4.4.2.

Cheng et al. [114] used a laser speckle technique to assess the retinal perfusion and measured an oxygen induced decrease of 20 % – 30 % in the whole retinal blood flow (capillaries and large vessels) of rats. On the other hand, as already mentioned in section 4.4.4, the results of hyperoxia experiments in humans show oxygen induced blood flow decreases ranging from 36 % – 60 % [83–88]. Hence, the values, describing the oxygen induced decrease in retinal blood flow, that were acquired in the course of this work (microcirculation and large vessels) are closer to the results of the human experiments than the values presented by Cheng et al. [114].

One possible explanation for the lower oxygen induced decrease in the retinal perfusion determined by Cheng et al. [114] is the fact that they used the relatively short time period of 3 min for the ambient air and the oxygen breathing phase before measuring the animals' blood flow. The previously mentioned human studies, as well as the work at hand, used longer time periods at baseline conditions and especially for the oxygen breathing phase, which might explain the more pronounced hyperoxia effect.

A few other methods exist that allow assessing capillaries noninvasively. An approach used by Srinivasan et al. [24] is based on an OCT angiography technique that is capable of measuring the total retinal blood flow in the large retinal vessels. However, this method can only qualitatively assess the retinal capillaries in form of angiography maps. Zhi et al. [115] used a similar method to measure changes in the retinal perfusion due to increased IOP. It should also be mentioned that Srinivasan et al. [116] and Lee et al. [117] introduced two different OCT angiography based methods, which are capable of measuring the velocities in the capillaries of the cerebral cortex.

It is interesting to study changes of the blood flow velocities in the retinal microcirculation, as the oxygen exchange between blood and retinal tissue mainly occurs in the capillaries. Therefore, it would be desirable to measure abnormalities in the retinal microcirculation even more precise than done in the course of this thesis, so that these abnormalities can be detected before retinal tissue is damaged due to insufficient blood and consequently oxygen supply.

6 Conclusion

In this thesis, a Fourier-domain Doppler OCT system combined with a dynamic vessel analyzer was developed in order to measure relative blood flow changes in large retinal vessels of the rat eye. Furthermore, a method to detect changes of the blood flow velocities in the retinal capillaries using the same OCT system was developed.

The measurement system's functionality was tested by performing in vitro experiments before any in vivo measurements were conducted. The blood flow values of the large retinal vessels were calculated from the vessels' blood flow velocities, which were acquired using the OCT system, and from the vessel diameters, which were measured simultaneously using the integrated dynamic vessel analyzer.

In the first set of in vivo experiments, the vasoconstriction effect of large retinal vessels due to oxygen breathing was studied in six test animals, yielding a vasoconstriction of $(13.2 \pm 5.2)\,\%$, a blood flow velocity reduction of $(42.9 \pm 5.3)\,\%$ and a decrease in blood flow of $(56.7 \pm 7.6)\,\%$. Thereafter, the flicker light induced vasodilation of large retinal vessels was investigated in four additional test animals, in which a vascular dilatation of $(3.2 \pm 2.4)\,\%$, a blood flow velocity increase of $(28.1 \pm 18.9)\,\%$ and an increase in blood flow of $(36.2 \pm 15.2)\,\%$ was observed. The results of both sets of experiments are in good agreement with the values from earlier human studies.

Not only the blood flow in large retinal vessels was determined, however: a further objective was to measure the blood flow in the retinal microcirculation. Before assessing the velocities in the retinal capillaries, it was necessary to develop LabVIEW post processing and data evaluation programs to extract the microcirculation information from segmented B-scans. Additionally, the system's ability to measure low flow velocities (as low as they occur in retinal capillaries) was tested by means of in vitro experiments before any animal was measured. Subsequently, relative blood flow velocity changes in the microcirculation due to oxygen breathing were measured in eight test animals. These experiments showed a decrease in the mean blood flow velocities of the retinal capillaries of $(48.2 \pm 9.9)\,\%$, which is in excellent agreement with the results of the large vessels' vasoconstriction experiments that were mentioned in the previous paragraph.

In summary, a small animal OCT system designed for the measurement of the retinal perfusion was developed and methods for the assessment of the retinal microcirculation were realized. Both the measurement system and the assessment methods were tested in vivo in rat eyes and showed promising results. The techniques developed in the course of this thesis have considerable potential to study ocular diseases in animal models, and thus, help gaining a deeper understanding of ocular diseases and their underlying perfusion disturbances, so that possible treatment strategies may be developed and tested.

7 Outlook

The measurement of blood flow changes in large retinal vessels and of blood flow velocity changes in the retinal capillaries with the OCT setup that was developed in the course of this thesis showed promising results in healthy rat eyes.

However, the data evaluation could be accelerated considerably by full automation of the vessel search program as well as the image registration program for the microcirculation data. The development of a fully automated image registration program could be useful for both the evaluation of large vessels, as well as for the registration of mircrocirculation tomograms.

Regarding the OCT setup, it might be a better approach to have the test animal lying on its side, so that the eye under study faces upwards, while the DVA and the OCT system's sample arm can be moved around to reach the desired measurement position instead of moving the animal. However, this approach would require a fiber based interferometer.

In order to be less sensitive to sample motion in future experiments, the data acquisition time of the OCT system needs to be shortened. This can be achieved by higher A-scan rates of just a few µs per A-scan. Therefore, the usage of a faster CCD camera in the OCT system's spectrometer is planned. Having an A-scan rate of e.g. 2.5 µs per A-scan will reduce the eye motion problem in the microcirculation measurements dramatically, as the acquisition of 100 B-scans consisting of 1000 A-scans each will only require 250 ms in contrast to the 16 s it takes with the system described in chapter 5. Furthermore, no segmented scanning will be needed to use the consecutive B-scan method, due to the fact that it will be possible to record a whole B-scan consisting of 1000 A-scans in 2.5 ms[i]. In addition, high speed data acquisition will allow recording a whole 3D data-set with e.g. 100 A-scans per slow scanning axis position. Thus, it will be possible to calculate the histogram of an averaged volume instead of only one averaged cross-sectional image. Besides, a faster line camera will enable the measurement of the high blood flow velocities in retinal arteries close to the ONH.

---

[i] Zotter et al. [106] showed that 2.5 ms is an appropriate time period between two consecutive A-scans, to assess the retinal microcirculation via Doppler OCT.

In order to gain a deeper understanding of the correlation between the disturbed retinal perfusion and the pathological mechanisms underlying the ocular diseases, it is necessary to use eye disease models and not only healthy rat eyes. Thus, our group has already begun with experiments that use rats with artificially elevated IOP as a model for glaucoma.

In conclusion there is potential for improvement in the measurement system, the data acquisition and the post-processing software; nevertheless important accomplishments were achieved in the course of this thesis: an OCT system capable of measuring blood flow changes in large retinal vessels as well as a measurement method for the assessment of the retinal microcirculation in rat eyes were developed. Both the OCT system and the microcirculation assessment method were successfully tested in vitro as well as in living animals.

It remains to be hoped that the findings of this thesis will contribute to the development of treatment methods for ocular diseases and will help to prevent irreversible blindness.

Appendix

A.1 Coherence

A.1.1 Relation: coherence time and spectral width

The following mathematical derivation of the relation between spectral width and coherence time can also be found in [50].

The quasi monochromatic light of a source is split into two beams using a Michelson interferometer setup (see Fig. 3.1). After double passing the interferometer arms the two beams interfere with each other and have gained a path length difference $\Delta L = z_R - z_{S_n}$. If both optical paths have a nearly equal length, distinct interference fringes are formed in the detector plane. An increasing ΔL results in a decreasing visibility of the interference fringes and they eventually disappear. This phenomenon can be explained by the assumption that light from a real source is not strictly monochromatic, but rather consists of wave trains of finite length. A large number of these wave trains pass at random time intervals during the time required to make an observation. Furthermore, we define that $F(t)$ is a light disturbance at the observation point P at the time t of a single wave train. $F(t)$ is assumed to be zero for $|t| \geq t_0$, where t_0 is the half duration time of the wave train, and can be expressed as Fourier integral

$$F(t) = \int\limits_{-\infty}^{\infty} f(\nu) \mathrm{e}^{-2\pi i \nu t} d\nu, \tag{A.1}$$

and by the Fourier inversion theorem

$$f(\nu) = \int\limits_{-\infty}^{\infty} F(t) \mathrm{e}^{2\pi i \nu t} dt. \tag{A.2}$$

During the time required for an observation, N such wave trains pass the point P, and hence, the total observed light disturbance can be written as

$$V(t) = \sum_{n=1}^{N} F(t - t_n), \tag{A.3}$$

where t_n stands for the arrival times of the wave trains. The light intensity averaged over the observation time $2T$ is

$$I = \frac{1}{2T} \int\limits_{-T}^{T} |V(t)|^2 \, dt \sim \frac{1}{2T} \int\limits_{-\infty}^{\infty} |V(t)|^2 \, dt, \tag{A.4}$$

if T is large compared to the half duration time t_0 of each wave train. Similar to the equation (A.1) one can define

$$V(t) = \int\limits_{-\infty}^{\infty} v(\nu) \mathrm{e}^{-2\pi i \nu t} d\nu, \tag{A.5}$$

and using (A.2) on (A.3) yields

$$v(\nu) = \sum_{n=1}^{N} \int\limits_{-\infty}^{\infty} F(t) \mathrm{e}^{2\pi i \nu (t - t_n)} dt = f(\nu) \sum_{n=1}^{N} \mathrm{e}^{2\pi i \nu t_n}. \tag{A.6}$$

by using the Parseval's theorem

$$\int\limits_{-\infty}^{\infty} |F(t)|^2 \, dt = \int\limits_{-\infty}^{\infty} |f(\nu)|^2 \, d\nu, \tag{A.7}$$

one gets

$$\int\limits_{-\infty}^{\infty} |V(t)|^2 \, dt = \int\limits_{-\infty}^{\infty} |v(\nu)|^2 \, d\nu = \int\limits_{-\infty}^{\infty} |f(\nu)|^2 \sum_{n=1}^{N} \sum_{m=1}^{N} \mathrm{e}^{2\pi i \nu (t_n - t_m} d\nu. \tag{A.8}$$

Looking closer at the double sum gives

$$\begin{aligned}\sum_{n=1}^{N}\sum_{m=1}^{N} \mathrm{e}^{2\pi i\nu(t_n-t_m)} &= N + \sum_{n\neq m} \mathrm{e}^{2\pi i\nu(t_n-t_m)} \\ &= N + \sum_{n<m} \mathrm{e}^{2\pi i\nu(t_n-t_m)} + \sum_{n>m} \mathrm{e}^{2\pi i\nu(t_n-t_m)} \\ &= N + \sum_{n<m} \mathrm{e}^{2\pi i\nu(t_n-t_m)} + \sum_{n<m} \mathrm{e}^{2\pi i\nu(t_m-t_n)} \\ &= N + \sum_{n<m} \left[\mathrm{e}^{2\pi i\nu(t_n-t_m)} + \mathrm{e}^{-2\pi i\nu(t_n-t_m)}\right].\end{aligned} \tag{A.9}$$

using the relation $\frac{\mathrm{e}^{ix}+\mathrm{e}^{-ix}}{2} = \cos x$ yields

$$\sum_{n=1}^{N}\sum_{m=1}^{N} \mathrm{e}^{2\pi i\nu(t_n-t_m)} = N + 2\sum_{n<m} \cos(2\pi\nu(t_n - t_m)). \tag{A.10}$$

Since, the t_n's in the double sum are randomly distributed, there is an equal probability for each cosine term to be positive or negative. Therefore, the cosine term vanishes for large N and the double sum results in N. Inserting this result in (A.8) and then in (A.4), one gets

$$I = \frac{N}{2T} \int_{-\infty}^{\infty} |f(\nu)|^2 \, d\nu. \tag{A.11}$$

Thus, the light intensity is proportional to the integral of the intensities $i(\nu) = |f(\nu)|^2$ of the monochromatic components that are forming a single wave train. The relation between the frequency range, over which the Fourier components have appreciable intensities, and the duration of the wave trains can be shown by a simple experiment. We assume that all wave trains have the duration Δt_c and $F(t)$ is periodic with the frequency ν_0 during Δt_c

$$F(t) = \begin{cases} f_0 \mathrm{e}^{-2\pi i\nu_0 t} & \text{when } |t| \leq \frac{\Delta t_c}{2} \\ 0 & \text{when } |t| > \frac{\Delta t_c}{2}, \end{cases} \tag{A.12}$$

and f_0 is a constant. Inserting (A.12) in (A.2) gives

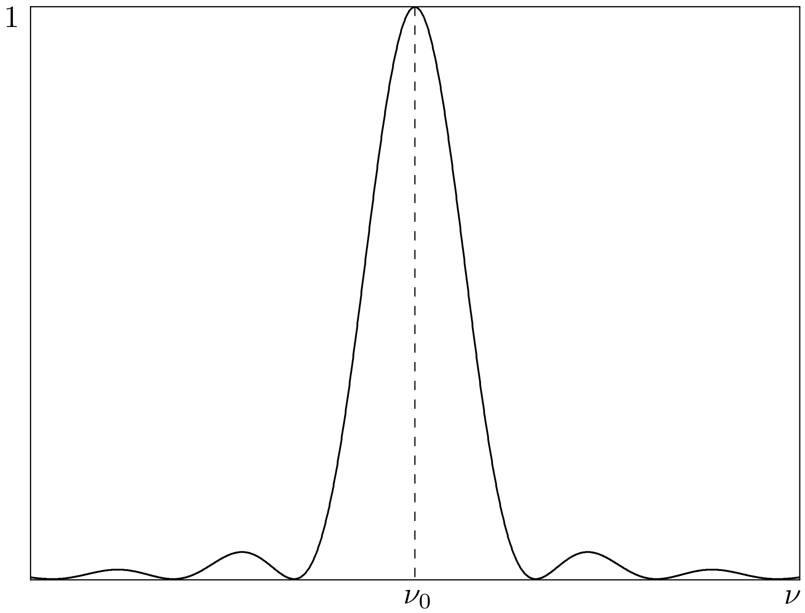

Figure A.1: Intensity distribution $[\sin(\pi(\nu-\nu_0)\Delta t_c)/(\pi(\nu-\nu_0)\Delta t_c)]^2$.

$$\begin{aligned} f(\nu) &= f_0 \int\limits_{-\frac{\Delta t_c}{2}}^{\frac{\Delta t_c}{2}} \mathrm{e}^{2\pi i(\nu-\nu_0)t} dt \\ &= f_0 \left[\frac{\mathrm{e}^{i\pi(\nu-\nu_0)\Delta t_c} - \mathrm{e}^{-i\pi(\nu-\nu_0)\Delta t_c}}{2i\pi(\nu-\nu_0)}\right] \\ &= f_0 \Delta t_c \left[\frac{\sin(\pi(\nu-\nu_0)\Delta t_c)}{\pi(\nu-\nu_0)\Delta t_c}\right] \end{aligned} \tag{A.13}$$

where the relation $\frac{\mathrm{e}^{ix}-\mathrm{e}^{-ix}}{2i} = \sin x$ was used. The intensity distribution of the Fourier components of equation (A.12) is given by $[\sin(\pi(\nu-\nu_0)\Delta t_c)/(\pi(\nu-\nu_0)\Delta t_c)]^2$, which is shown in Fig. A.1. Appreciable intensity values can be found in the frequency interval $\nu_0 - \frac{\Delta\nu}{2} \leq \nu \leq \nu_0 + \frac{\Delta\nu}{2}$. The first zero occurs at $\nu - \nu_0 = \pm\frac{1}{\Delta t_c}$, thus, it is obvious that

$$\Delta\nu \sim \frac{1}{\Delta t_c} \tag{A.14}$$

This equation tells us that the effective frequency range of the Fourier spectrum is of the order of the reciprocal of the duration of a single wave train Δt_c, which is also known as coherence time.

A.1.2 Spectral width and relative spectral width

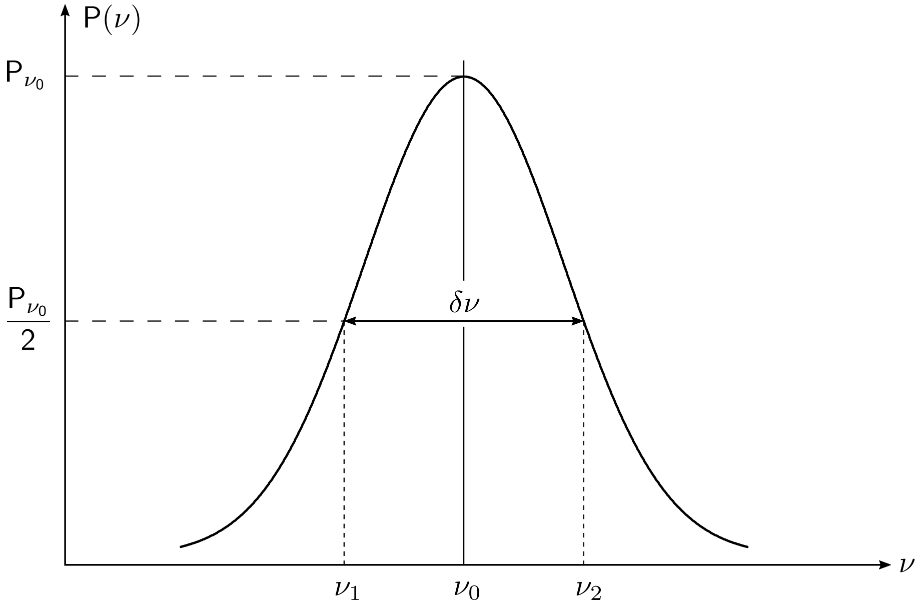

Figure A.2: Gaussian power spectrum and its spectral line width $\delta\nu$. ν_0 is the center frequency of this power spectrum.

The spectral bandwidth of a light source or rather a light beam $\delta\nu = |\nu_1 - \nu_2|$ (ν represents the frequency), is defined as the FWHM of the power spectrum of this light beam; as illustrated in Fig. A.2. It is also common to write the spectral bandwidth as angular frequency $\delta\omega = 2\pi\delta\nu$ or as wave length interval $\delta\lambda = |\lambda_1 - \lambda_2|$. Knowing the relation $\lambda = c/\nu$, where c stands for the speed of light, one can write

$$\begin{aligned} \delta\lambda &= -\frac{c}{\nu^2}\delta\nu \\ \delta\lambda &= -\frac{\lambda}{\nu}\delta\nu \\ \frac{\delta\lambda}{\lambda} &= -\frac{\delta\nu}{\nu}. \end{aligned} \tag{A.15}$$

This leads to the conclusion that the relative spectral width is the same in all notations

$$\left|\frac{\delta\lambda}{\lambda}\right| = \left|\frac{\delta\nu}{\nu}\right| = \left|\frac{\delta\omega}{\omega}\right|. \tag{A.16}$$

Therefore the spectral bandwidth can also be written as

$$\begin{aligned}\frac{\Delta\nu}{\nu} &= \frac{\Delta\lambda}{\lambda} \\ \Delta\nu &= \frac{\Delta\lambda\cdot\nu}{\lambda} = \frac{\Delta\lambda\cdot c}{\lambda\cdot\lambda} = c\cdot\frac{\Delta\lambda}{\lambda^2} \\ \frac{1}{\Delta\nu} &= \frac{1}{c}\cdot\frac{\lambda^2}{\Delta\lambda}.\end{aligned} \tag{A.17}$$

A.1.3 FWHM of a Gaussian function

An arbitrary Gaussian function is defined as:

$$f(x) = a\cdot \mathrm{e}^{-\frac{(x-b)^2}{2d^2}} \tag{A.18}$$

To fit the case in section 3.1.2 equation (3.10) we make the assumption that $a = 1$ and $b = 0$, and we pull the factor 2 in the denominator of the exponent into the constant d^2, which yields

$$f(x) = \mathrm{e}^{-\frac{x^2}{d^2}}. \tag{A.19}$$

To get the maximum of the Gaussian function, equation (A.19) has to be differentiated

$$\frac{\mathrm{d}}{\mathrm{dx}}f(x) = f'(x) = -\frac{2x}{d^2}\cdot \mathrm{e}^{-\frac{x^2}{d^2}} \tag{A.20}$$

and evaluated at the postition $x = 0$, which yields $f'(0) = 0$. Knowing the position of the maximum and inserting it in equation (A.19) results in $f(0) = 1$. Accordingly, the half maximum has to be 1/2 and one gets

$$\begin{aligned}f(x) = \mathrm{e}^{-\frac{x^2}{d^2}} &= \frac{1}{2} \\ -\frac{x^2}{d^2} &= \ln\frac{1}{2} = \ln 1 - \ln 2 = -\ln 2 \\ x^2 &= \ln 2\cdot d^2 \\ x_{1,2} &= \pm\sqrt{\ln 2}\cdot d.\end{aligned} \tag{A.21}$$

The FWHM is the difference between x_1 and x_2:

$$\begin{aligned}\Delta x_{FWHM} &= |x_1 - x_2| \\ &= \left|\sqrt{\ln 2}\cdot d + \sqrt{\ln 2}\cdot d\right| \\ &= 2\sqrt{\ln 2}\cdot d.\end{aligned} \tag{A.22}$$

To calculate the FWHM of the Gaussian self coherence function [51]

$$|\Gamma(\tau)| \propto \exp\left[-\left(\frac{\pi\Delta\nu}{2\sqrt{\ln 2}}\tau\right)^2\right], \tag{A.23}$$

equation (A.22) can be rewritten to

$$\frac{\Delta x_{FWHM}}{d} = 2\sqrt{\ln 2}. \tag{A.24}$$

Considering that the FWHM of the coherence function $\Gamma(\tau)$ can be defined as the coherence time Δt_c, and using (A.24) on (A.23) results in

$$\begin{aligned}\frac{\Delta x_{FWHM}}{d} = \frac{\pi\Delta\nu}{2\sqrt{\ln 2}}\Delta t_c &= 2\sqrt{\ln 2} \\ \Delta t_c &= \frac{4\ln 2}{\pi\Delta\nu}.\end{aligned} \tag{A.25}$$

A.2 Linear approximation of the wavelength to pixel correlation and rescaling of the spectra

A.2.1 Linear approximation of the relationship between λ_x and x

As mentioned in section 4.1.4, the wavelength λ_x of a light beam, diffracted by the spectrometer's grating, is related to the distance x, between the center of the CCD array and the position, on which the light beam is focused. This relation (cf. 4.9)

$$\lambda_x = g\cdot\left(\sin\phi + \sin\left[\psi_c + \arctan\left(\frac{x}{f}\right)\right]\right) \tag{A.26}$$

is non-linear, thus, the distribution of wavelengths on the camera pixels is not entirely equidistant. This non-linear behavior of Eq. (A.26) can be investigated by means of a Taylor expansion:

$$\begin{aligned}\lambda_x &\approx g\cdot\left(\sin\phi+\sin\psi_c\cdot\left[1-\frac{1}{2}\left(\frac{x}{f}\right)^2+...\right]+\right.\\ &\qquad\left.+\cos\psi_c\cdot\left(\frac{x}{f}\right)\left[1-\frac{1}{2}\left(\frac{x}{f}\right)^2+...\right]\right)\\ &=g\cdot\left(\sin\phi+\sin\psi_c+\cos\psi_c\left(\frac{x}{f}\right)-\frac{\sin\psi_c}{2}\left(\frac{x}{f}\right)^2-\right.\\ &\qquad\left.-\frac{\cos\psi_c}{2}\left(\frac{x}{f}\right)^3+...\right).\end{aligned}\tag{A.27}$$

A detailed explanation of the mathematical steps between Eq. (A.26) and Eq. (A.27) is given by Doblhoff-Dier [21]. Due to the fact that the focal length of the camera lens f is longer than half the length of the CCD array, $\frac{x}{f}$ is small and terms of the order 2 or higher can be disregarded, thus one gets

$$\lambda_x \approx g\cdot\left(\sin\phi+\sin\psi_c+\cos\psi_c\left(\frac{x}{f}\right)\right).\tag{A.28}$$

To check how much this linear approximation (A.28) deviates from the exact relation between λ_x and x (A.26), the maximum wavelength $\lambda_{x_{\max}}$ that is still imaged on the CCD array is calculated with both equations. As mentioned in section 4.1.4, the grating constant $g=\frac{1}{1200}$ mm, the angle of the incident beam $\phi=30°$ and the angle of diffraction, of light beams with the central wavelength of 841 nm, $\psi_c=30.6°$. Inserting this parameters, along with half the length of the CCD array $x_{\max}=14.34\,\text{mm}$[ii] and the focal length of the camera lens $f=100\,\text{mm}$, into Eq. (A.26) and Eq. (A.28) yields

$$\begin{aligned}\lambda^{\text{exact}}_{x_{\max}} &= 938.39\,\text{nm},\\ \lambda^{\text{approx}}_{x_{\max}} &\approx 943.73\,\text{nm},\end{aligned}\tag{A.29}$$

respectively. Hence, the error that is made when using the linear approximation is very small $\Delta\lambda_{x_{\max}}=0.57\,\%$ and can be compensated in the rescaling process.

A.2.2 Rescaling of the spectra

As stated in Eq. (A.28), the position on the CCD array is correlated linearly with the wavelength of the arriving light beam. Hence, every CCD pixel records a different wavelength, as the pixels correspond to different positions on the CCD array, i.e. in FDOCT the spectra are recorded in λ-space.

[ii] The CCD array of the AViiVA M2 CL 2014 line camera has 2048 pixels with 14 × 14 µm each. Thus, half of the array has a length of 14.34 mm.

However, FDOCT measures the depths of the reflecting sample layers via the oscillation frequencies in the interference signal (see section 3.3). In order to gain the depth information of the sample layers these oscillation frequencies have to be Fourier transformed. Before doing so the data have to be converted in frequency-space (also known as k-space or $\frac{1}{\lambda}$-space). However, since the spectra are recorded in λ-space, the datapoints are not regularly spaced in k-space, as it is reciprocal to the λ-space. To describe measured object structures correctly, the calculated intensity values have to be equidistant in the position-space (z-space). Therefore, the spectra need to be rescaled, so that they already have equidistant datapoints in k-space before the Fourier transformation [118]. Furthermore, equidistant datapoins are required to use a fast Fourier transform (FFT) algorithm[iii].

The rescaling process is described graphically in Fig. A.3, for wavelengths that are linearly distributed in λ-space. The indices i (see the blue bars in Fig. A.3) represent the numbers of the CCD pixels, each recording a certain wavelength. i are hence linear in λ-space (according to the approximation described by Eq. (A.28)), and consequently non-linear in k-space. j on the other hand represent the corresponding indices that are linear in k-space and non-linear in λ-space (see the orange bars in Fig. A.3).

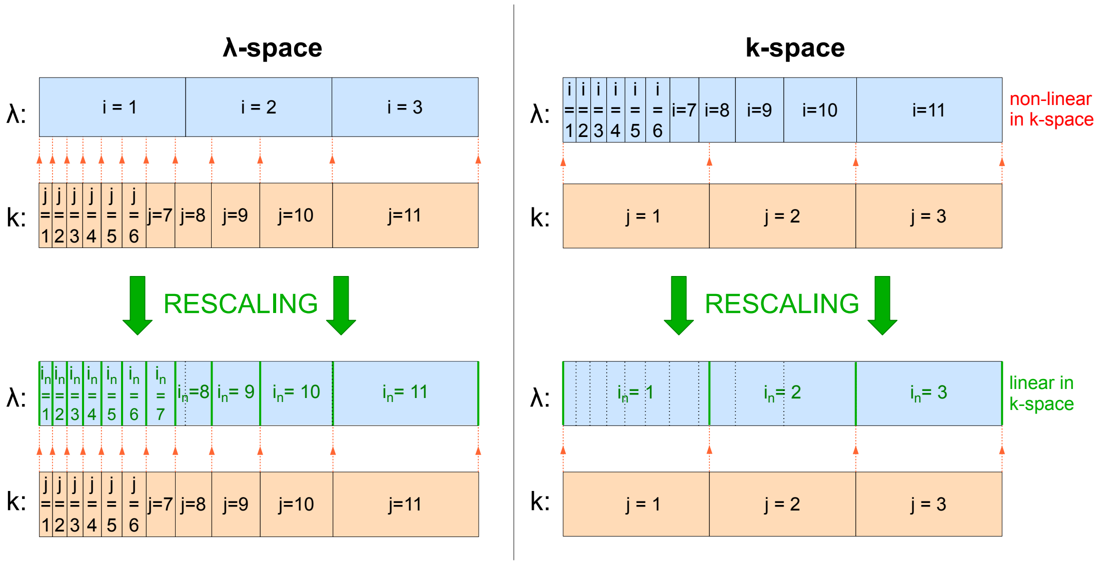

Figure A.3: Graph showing the rescaling process in λ-space, as well as in k-space. Indices i describe the pixel numbers on the CCD array and hence are linear in *lambda*-space. i need to be rescaled to the indices i_{new} (or i_n in this graph), which are linear in k-space [21].

[iii] To Fourier transform non-linear data, a discrete Fourier transform (DFT) algorithm can be used, but none of these algorithms are as efficient as FFT algorithms in terms of computing time. However, data sets with uneven spacing of datapoints have to be rescaled, in such a way that they have an equidistant datapoint distribution in k-space, to be transformed by an FFT algorithm [119].

In order to get datapoints that are linearly distributed in k-space, the indices i have to be rescaled to i_{new}, which are linear in k-space, as shown at the bottom of Fig. A.3.

Mathematical description of the rescaling process

A mathematical derivation of the afore mentioned rescaling process is given in the following, and can also be found in Baumann[118] and Doblhoff-Dier [21]. However, it is only applicable for datapoints that are equidistant in λ-space.

As described in section 4.1.4, each wavelength λ_i is imaged onto a different position and hence a different CCD pixel i of the spectrometer's line camera. Since the line camera's CCD array has N pixel, $i \in [0, N-1]$. Thus, the minimum wavelength λ_{min} that is still detectable by the spectrometer, is imaged onto the pixel $i = 0$, while the maximum detectable wavelength λ_{max} is imaged onto the pixel $i = N-1$. Dividing the interval $[\lambda_{\mathrm{min}}, \lambda_{\mathrm{max}}]$ into N equal steps $\frac{1}{N-1}\left(\lambda_{\mathrm{max}} - \lambda_{\mathrm{min}}\right)$, one can write

$$\lambda_i = \lambda_{\mathrm{min}} + \frac{i}{N-1}\left(\lambda_{\mathrm{max}} - \lambda_{\mathrm{min}}\right). \tag{A.30}$$

A similar relation that is equidistant in the reciprocal k-space can be formulated, with $k_{\mathrm{min}} \propto \frac{1}{\lambda_{\mathrm{max}}}$ and $k_{\mathrm{max}} \propto \frac{1}{\lambda_{\mathrm{min}}}$:

$$\begin{aligned} k_j &= k_{\mathrm{min}} + \frac{j}{N-1}\left(k_{\mathrm{max}} - k_{\mathrm{min}}\right) \\ &= \frac{1}{\lambda_{\mathrm{max}}} + \frac{j}{N-1}\left(\frac{1}{\lambda_{\mathrm{min}}} - \frac{1}{\lambda_{\mathrm{max}}}\right). \end{aligned} \tag{A.31}$$

To put λ_i in the correct reciprocal relation with k_j, which are equidistant distributed in k-space, a new set of indices i_{new} (see Fig. A.3, bottom) that are interpolated between the original integer indices i, has to be introduced:

$$\begin{aligned} \frac{1}{\lambda_{i_{\mathrm{new}}}} &= k_j \\ \frac{1}{\lambda_{\mathrm{min}} + \frac{i_{\mathrm{new}}}{N-1}\left(\lambda_{\mathrm{max}} - \lambda_{\mathrm{min}}\right)} &= \frac{1}{\lambda_{\mathrm{max}}} + \frac{j}{N-1}\left(\frac{1}{\lambda_{\mathrm{min}}} - \frac{1}{\lambda_{\mathrm{max}}}\right). \end{aligned} \tag{A.32}$$

Reducing the right side of this equation to a common denominator and taking the reciprocal of the whole equation yields

$$\lambda_{\mathrm{min}} + \frac{i_{\mathrm{new}}}{N-1}\left(\lambda_{\mathrm{max}} - \lambda_{\mathrm{min}}\right) = \frac{(N-1)\cdot\lambda_{\mathrm{max}}\cdot\lambda_{\mathrm{min}}}{(N-1)\cdot\lambda_{\mathrm{min}} + j\cdot\left(\lambda_{\mathrm{max}} - \lambda_{\mathrm{min}}\right)}. \tag{A.33}$$

Solving this equation for i_{new} gives

$$i_{\mathrm{new}} = \frac{N-1}{\lambda_{\mathrm{max}} - \lambda_{\mathrm{min}}}\cdot\left(\frac{(N-1)\cdot\lambda_{\mathrm{max}}\cdot\lambda_{\mathrm{min}}}{(N-1)\cdot\lambda_{\mathrm{min}} + j\cdot\left(\lambda_{\mathrm{max}} - \lambda_{\mathrm{min}}\right)} - \lambda_{\mathrm{min}}\right) \tag{A.34}$$

Reducing the expression in the brackets to a common denominator and simplifying the equation results in

$$i_{\text{new}} = \frac{(N-1)\cdot(N-1-j)}{N-1+j\cdot(\frac{\lambda_{\text{max}}}{\lambda_{\text{min}}}-1)}. \tag{A.35}$$

Defining $q = \frac{\lambda_{\text{max}}}{\lambda_{\text{min}}}$ finally gives

$$i_{\text{new}} = \frac{(N-1)\cdot(N-1-j)}{N-1+j\cdot(q-1)}. \tag{A.36}$$

This equation describes the relation between the index of interpolation i_{new} of the datapoints in λ-space and a certain index j of the datapoints in k-space.

Bibliography

[1] Beatrix Feigl. Age-related maculopathy – Linking aetiology and pathophysiological changes to the ischaemia hypothesis. *Progress in Retinal and Eye Research*, 28(1):63–86, 2009. doi: 10.1016/j.preteyeres.2008.11.004.

[2] Berthold Pemp and Leopold Schmetterer. Ocular blood flow in diabetes and age-related macular degeneration. *Canadian Journal of Ophthalmology*, 43(3): 295–301, 2008. doi: 10.3129/i08-049.

[3] Juan E Grunwald, Charles E. Riva, Joan Baine, and Alexander J. Brucker. Total retinal volumetric blood flow rate in diabetic patients with poor glycemic control. *Investigative Ophthalmology and Visual Science*, 33(2):356–63, 1992.

[4] B. Pemp, E. Polska, G. Garhofer, M. Bayerle-Eder, A. Kautzky-Willer, and L. Schmetterer. Retinal blood flow in type 1 diabetic patients with no or mild diabetic retinopathy during euglycemic clamp. *Diabetes Care*, 33(9):2038–42, 2010. doi: 10.2337/dc10-0502.

[5] Jennifer T. Durham and Ira M. Herman. Microvascular modifications in diabetic retinopathy. *Current Diabetes Reports*, 11(4):253–264, 2011. doi: 10.1007/s11892-011-0204-0.

[6] A. Popa Cherecheanu, G. Garhofer, D. Schmidl, R. Werkmeister, and L. Schmetterer. Ocular perfusion pressure and ocular blood flow in glaucoma. *Current Opinion in Pharmacology*, 13(1):36–42, 2013. doi: 10.1016/j.coph.2012.09.003.

[7] Vital P. Costa, Alon Harris, Douglas Anderson, Richard Stodtmeister, Fernanda Cremasco, Helene Kergoat, John Lovasik, Ingborg Stalmans, Oliver Zeitz, Ines Lanzl, Konstantin Gugleta, and Leopold Schmetterer. Ocular perfusion pressure in glaucoma. *Acta Ophthalmologica*, 92(4):e252–e266, 2014. doi: 10.1111/aos.12298.

[8] Z. Chen and J. Zhang. Doppler optical coherence tomography. In Wolfgang Drexler and James G. Fujimoto, editors, *Optical Coherence Tomography: Technology and Applications*, chapter 21, pages 621–651. Springer-Verlag, Berlin, Heidelberg, 2008.

[9] Rainer A. Leitgeb, René M. Werkmeister, Cedric Blatter, and Leopold Schmetterer. Doppler optical coherence tomography. *Progress in Retinal and Eye Research*, 41:26–43, 2014. doi: 10.1016/j.preteyeres.2014.03.004.

[10] Gerhard Garhofer, Rene Werkmeister, Dragostinoff Nikolaus, and Leopold Schmetterer. Retinal blood flow in healthy young subjects. *Investigative Ophthalmology and Visual Science*, 53(2):698–703, 2012. doi: 10.1167/iovs.11-8624.

[11] J. E. Grunwald, J. DuPont, and C. E. Riva. Retinal haemodynamics in patients with early diabetes mellitus. *British Journal of Ophthalmology*, 80(4): 327–331, 1996. doi: 10.1136/bjo.80.4.327.

[12] Michael Lasta, Berthold Pemp, Doreen Schmidl, Agnes Boltz, Semira Kaya, Stefan Palkovits, Rene Werkmeister, Kinga Howorka, Alina Popa-Cherecheanu, Gerhard Garhöfer, and Leopold Schmetterer. Neurovascular dysfunction precedes neural dysfunction in the retina of patients with type 1 diabetes. *Investigative Ophthalmology and Visual Science*, 54(1):842–847, 2013. doi: 10.1167/iovs.12-10873.

[13] Wolfgang Drexler and James G. Fujimoto. State-of-the-art retinal optical coherence tomography. *Progress in Retinal and Eye Research*, 27(1):45–88, 2008. doi: 10.1016/j.preteyeres.2007.07.005.

[14] H.E. König and H. Bragulla. *Anatomie der Haussäugetiere: Lehrbuch und Farbatlas für Studium und Praxis*. Schattauer GmbH, Stuttgart, 4th edition, 2009.

[15] Michael Land. *photoreception, Encyclopædia Britannica*. Encyclopædia Britannica Ultimate Reference Suite. Encyclopædia Britannica, Chicago, 2015.

[16] Laura Fanea and Andrew J. Fagan. Review: Magnetic resonance imaging techniques in ophthalmology. *Molecular Vision*, 18:2538–2560, 2012.

[17] Puneet Tyagi, Rajendra S. Kadam, and Uday B. Kompella. Comparison of suprachoroidal drug delivery with subconjunctival and intravitreal routes using noninvasive fluorophotometry. *PLoS ONE*, 7(10):1–9, 2012. doi: 10.1371/journal.pone.0048188.

[18] Jonathan J. Liu, Ireneusz Grulkowski, Martin F. Kraus, Benjamin Potsaid, Chen D. Lu, Bernhard Baumann, Jay S. Duker, Joachim Hornegger, and James G. Fujimoto. In vivo imaging of the rodent eye with swept source/Fourier domain OCT. *Biomedical Optics Express*, 4(2):351–363, 2013. doi: 10.1364/BOE.4.000351.

[19] Henry Gray. *Gray's Anatomy*. Lea and Febiger, Philadelphia, 20th edition, 1918. URL `http://www.bartleby.com/107/illus882.html`.

[20] Gerhard Thews, Ernst Mutschler, and Peter Vaupel. *Anatomie, Physiologie, Pathophysiologie des Menschen.* Wissenschaftliche Verlagsgesellschaft, 1999.

[21] Veronika Doblhoff-Dier. *Determination of the Total Retinal Blood Flow Using Fourier-Domain Optical Coherence Tomography and Fundus Imaging.* Doctoral thesis, 2014.

[22] A. Hughes. A schematic eye for the rat. *Vision Research*, 19(5):569–588, 1979. doi: 10.1016/0042-6989(79)90143-3.

[23] Richard S. Snell and Michael A. Lemp. *Clinical Anatomy of the Eye.* Blackwell Science Ltd, Oxford, 2nd edition, 1998.

[24] Vivek J. Srinivasan and Harsha Radhakrishnan. Total average blood flow and angiography in the rat retina. *Journal of Biomedical Optics*, 18(7):076025, 2013. doi: 10.1117/1.JBO.18.7.076025.

[25] Lee Ann Remington. *Clinical anatomy and physiology of the visual system.* Butterworth-Heinemann, Saint Louis, 3rd edition, 2012.

[26] R. Heywood. Some clinical observations on the eyes of sprague-dawley rats. *Laboratory Animals*, 7(1):19–27, 1973. doi: 10.1258/002367773781005914.

[27] Gesine Huber, Severin Heynen, Coni Imsand, Franziska vom Hagen, Regine Muehlfriedel, Naoyuki Tanimoto, Yuxi Feng, Hans-Peter Hammes, Christian Grimm, Leo Peichl, Mathias W. Seeliger, and Susanne C. Beck. Novel rodent models for macular research. *PLoS ONE*, 5(10):e13403, 2010. doi: 10.1371/journal.pone.0013403.

[28] Hermann D. Schubert. Structure and function of the neural retina. In Myron Yanoff and Jay S. Duker, editors, *Ophthalmology*, chapter 99, pages 771–774. Mosby, 2nd edition, 2004.

[29] Anne Hanson. The rat's eyes. *Rat Behavior and Biology*, 11 June 2009. URL `http://www.ratbehavior.org/Eyes.htm`. Web. 16 May 2015.

[30] Shiyoung Roh and John J. Weiter. Retinal and choroidal circulation. In Myron Yanoff and Jay S. Duker, editors, *Ophthalmology*, chapter 101, pages 779–782. Mosby, 2nd edition, 2004.

[31] Adam Martidis and Matthew T.S. Tennant. Age-related macular degeneration. In Myron Yanoff and Jay S. Duker, editors, *Ophthalmology*, chapter 125, pages 925–933. Mosby, 2nd edition, 2004.

[32] Brett J. Rosenblatt and William E. Benson. Diabetic retinopathy. In Myron Yanoff and Jay S. Duker, editors, *Ophthalmology*, chapter 117, pages 877–886. Mosby, 2nd edition, 2004.

[33] Scott Fraser and Richard Wormald. Epidemiology of glaucoma. In Myron Yanoff, Jay S. Duker, and Mark Sherwood, editors, *Ophthalmology*, chapter 210, pages 1413–1417. Mosby, 2nd edition, 2004.

[34] Paul F. Palmberg and Janey L. Wiggs. Mechanisms of glaucoma. In Myron Yanoff, Jay S. Duker, and Mark Sherwood, editors, *Ophthalmology*, chapter 212, pages 1423–1430. Mosby, 2nd edition, 2004.

[35] Matthias C. Grieshaber and Josef Flammer. Blood flow in glaucoma. *Current Opinion in Ophthalmology*, 16(2):79–83, 2005.

[36] Maneli Mozaffarieh, Matthias C. Grieshaber, and Josef Flammer. Oxygen and blood flow: players in the pathogenesis of glaucoma. *Molecular Vision*, 14:224–233, 2008.

[37] Michael G. Morley and Jeffrey S. Heier. Venous obstractive disease of the retina. In Myron Yanoff and Jay S. Duker, editors, *Ophthalmology*, chapter 115, pages 862–869. Mosby, 2nd edition, 2004.

[38] Alon Harris, Larry Kagemann, and George A. Cioffi. Assessment of human ocular hemodynamics. *Survey of Ophthalmology*, 42(6):509–533, 1998.

[39] Leopold Schmetterer and Gerhard Garhofer. How can blood flow be measured? *Survey of Ophthalmology*, 52(2):S134–S138, 2007.

[40] René M. Werkmeister. *Dual-beam Bidirectional Doppler Fourier-Domain Optical Coherence Tomography.* Doctoral thesis, 2010.

[41] Daniel Pauleikhoff, Georg Spital, Martin Radermacher, Gabriele A. Brumm, Albrecht Lommatzsch, and Alan C. Bird. A fluorescein and indocyanine green angiographic study of choriocapillaris in age-related macular disease. *Archives of Ophthalmology*, 117(10):1353–1358, 1999. doi: 10.1001/archopht.117.10.1353.

[42] C. E. Riva and B. Petrig. Blue field entoptic phenomenon and blood velocity in the retinal capillaries. *Optical Society of America*, 70(10):1234–1238, 1980.

[43] Charles E. Riva, Gilbert T. Feke, Bruno Eberli, and Vili Benary. Bidirectional LDV system for absolute measurement of blood speed in retinal vessels. *Applied Optics*, 18(13):2301–2306, 1979.

[44] Robert F. Bonner and Ralph Nossal. Principles of laser-Doppler flowmetry. In A. Shepherd and P. Oberg, editors, *Laser-Doppler Blood Flowmetry*, chapter 2, pages 17–45. Kluwer Academic Publishers, 1990.

[45] Sunil Ganekal. Retinal functional imager (RFI): Non-invasive functional imaging of the retina. *Nepalese Journal of Ophthalmology*, 5(10):250–257, 2013.

[46] Veronika Doblhoff-Dier, Leopold Schmetterer, Walthard Vilser, Gerhard Garhöfer, Martin Gröschl, Rainer A. Leitgeb, and René M. Werkmeister. Measurement of the total retinal blood flow using dual beam Fourier-domain Doppler optical coherence tomography with orthogonal detection planes. *Biomedical Optics Express*, 5(2):630–642, 2014.

[47] René M. Werkmeister, Nikolaus Dragostinoff, Michael Pircher, Erich Götzinger, Christoph K. Hitzenberger, Rainer A. Leitgeb, and Leopold Schmetterer. Bidirectional Doppler Fourier-domain optical coherence tomography for measurement of absolute flow velocities in human retinal vessels. *Optics Letters*, 33(24):2967–2969, 2008. doi: 10.1364/OL.33.002967.

[48] James G. Fujimoto and Wolfgang Drexler. Introduction to optical coherence tomography. In Wolfgang Drexler and James G. Fujimoto, editors, *Optical Coherence Tomography: Technology and Applications*, chapter 1, pages 1–45. Springer-Verlag, Berlin, Heidelberg, 2008.

[49] J.A. Izatt and M.A. Choma. Theory of optical coherence tomography. In Wolfgang Drexler and James G. Fujimoto, editors, *Optical Coherence Tomography: Technology and Applications*, chapter 2, pages 47–72. Springer-Verlag, Berlin, Heidelberg, 2008.

[50] Max Born and Emil Wolf. Elements of the theory of interference and interferometers. In *Principles of Optics: Electromagnetic Theory of Propagation, Interference and Diffraction of Light*, chapter 7, pages 286–411. Cambridge University Press, 7th edition, 1999.

[51] A.F. Fercher and C.K. Hitzenberger. Optical coherence tomography. In E. Wolf, editor, *Progress in Optics*, volume 44, chapter 4, pages 215–302. Elsevier, 2002.

[52] Anjul M. Davis. *Development of Fourier domain optical coherence tomography for applications in developmental biology.* Dissertation, 2008.

[53] M. Wojtkowski, A. Kowalczyk, R. Leitgeb, and A. F. Fercher. Full range complex spectral optical coherence tomography technique in eye imaging. *Optics Letters*, 27(16):1415–1417, 2002.

[54] Rainer A. Leitgeb, Christoph K. Hitzenberger, Adolf F. Fercher, and Tomasz Bajraszewski. Phase-shifting algorithm to achieve high-speed long-depth-range probing by frequency-domain optical coherence tomography. *Optics Letters*, 28(22):2201–2203, 2003.

[55] Erich Götzinger, Michael Pircher, Rainer A. Leitgeb, and Christoph K. Hitzenberger. High speed full range complex spectral domain optical coherence tomography. *Optics Express*, 13(2):583–594, 2005.

[56] Bernhard Baumann, Michael Pircher, Erich Götzinger, and Christoph K. Hitzenberger. Full range complex spectral domain optical coherence tomography without additional phase shifters. *Optics Express*, 15(20):13375–13387, 2007.

[57] Blausen.com staff. Blausen gallery 2014. *Wikiversity Journal of Medicine*, 2014. doi: 10.15347/wjm/2014.010.

[58] Edmund Koch, Julia Walther, and Maximiliano Cuevas. Limits of Fourier domain Doppler-OCT at high velocities. *Sensors and Actuators A: Physical*, 156(1):8–13, 2009. doi: 10.1016/j.sna.2009.01.022.

[59] Stephen D. Wajer, Makoto Taomoto, D. Scott McLeod, Russell L. McCally, Hirokazu Nishiwaki, Mary E. Fabry, Ronald L. Nagel, and Gerard A. Lutty. Velocity measurements of normal and sickle red blood cells in the rat retinal and choroidal vasculatures. *Microvascular Research*, 60(3):281–293, 2000. doi: 10.1006/mvre.2000.2270.

[60] Tess E. Kornfield and Eric A. Newman. Measurement of retinal blood flow using fluorescently labeled red blood cells. *eNeuro*, 2(2):e0005–15.2015, 2015. doi: 10.1523/ENEURO.0005-15.2015.

[61] Yimin Wang, Bradley A. Bower, Joseph A. Izatt, Ou Tan, and David Huang. Retinal blood flow measurement by circumpapillary Fourier domain Doppler optical coherence tomography. *Journal of Biomedical Optics*, 13(6):064003, 2008. doi: 10.1117/1.2998480.

[62] Bernhard Baumann, Benjamin Potsaid, Martin F. Kraus, Jonathan J. Liu, David Huang, Joachim Hornegger, Alex E. Cable, Jay S. Duker, and James G. Fujimoto. Total retinal blood flow measurement with ultrahigh speed swept source/Fourier domain OCT. *Biomedical Optics Express*, 2(6):1539–1552, 2011. doi: 10.1364/BOE.2.001539.

[63] WooJhon Choi, Bernhard Baumann, Jonathan J. Liu, Allen C. Clermont, Edward P. Feener, Jay S. Duker, and James G. Fujimoto. Measurement of pulsatile total blood flow in the human and rat retina with ultrahigh speed spectral/Fourier domain OCT. *Biomedical Optics Express*, 3(5):1047–1061, 2012. doi: 10.1364/BOE.3.001047.

[64] Wolfgang Trasischker, René M. Werkmeister, Stefan Zotter, Bernhard Baumann, Teresa Torzicky, Michael Pircher, and Christoph K. Hitzenberger. In vitro and in vivo three-dimensional velocity vector measurement by three-beam spectral-domain Doppler optical coherence tomography. *Journal of Biomedical Optics*, 18(11):116010, 2013. doi: 10.1117/1.JBO.18.11.116010.

[65] René M. Werkmeister, Martin Vietauer, Corinna Knopf, Clemens Fürnsinn, Rainer A. Leitgeb, Herbert Reitsamer, Martin Gröschl, Gerhard Garhöfer,

Walthard Vilser, and Leopold Schmetterer. Measurement of retinal blood flow in the rat by combining Doppler Fourier-domain optical coherence tomography with fundus imaging. *Journal of Biomedical Optics*, 19(10):106008, 2014. doi: 10.1117/1.JBO.19.10.106008.

[66] Dietmar Link, Clemens Strohmaier, Bernd U. Seifert, Thomas Riemer, Herbert A. Reitsamer, Jens Haueisen, and Walthard Vilser. Novel non-contact retina camera for the rat and its application to dynamic retinal vessel analysis. *Biomedical Optics Express*, 2(11):3094–3108, 2011. doi: 10.1364/BOE.2.003094.

[67] B. Hyle Park, Mark C. Pierce, Barry Cense, Seok-Hyun Yun, Mircea Mujat, Guillermo J. Tearney, Brett E. Bouma, and Johannes F. de Boer. Real-time fiber-based multi-functional spectral-domain optical coherence tomography at 1.3 µm. *Optics Express*, 13(11):3931–3944, 2005.

[68] Sang-Won Lee, Hyun-Woo Jeong, Beop-Min Kim, Yeh-Chan Ahn, Woong-gyu Jung, and Zhongping Chen. Optimization for axial resolution, depth range, and sensitivity of spectral domain optical coherence tomography at 1.3 µm. *Journal of the Korean Physical Society*, 55(6):2354–2360, 2009. doi: 10.3938/jkps.55.2354.

[69] F.J. Duarte. The uncertainty principle in optics. In F.J. Duarte, editor, *Tunable Laser Optics*, chapter 3, pages 59–76. CRC Press, Boca Raton, Florida, 2nd edition, 2015.

[70] Amardeep S. G. Singh, Tilman Schmoll, and Rainer A. Leitgeb. Segmentation of Doppler optical coherence tomography signatures using a support-vector machine. *Biomedical Optics Express*, 2(5):1328–1339, 2011. doi: 10.1364/BOE.2.001328.

[71] R. Leitgeb, C. K. Hitzenberger, and A. F. Fercher. Performance of fourier domain vs. time domain optical coherence tomography. *Optics Express*, 11(8): 889–894, 2003. doi: 10.1364/OE.11.000889.

[72] Tilman Schmoll, Christoph Kolbitsch, and Rainer A. Leitgeb. Ultra-high-speed volumetric tomography of human retinal blood flow. *Optics Express*, 17 (5):4166–4176, 2009. doi: 10.1364/OE.17.004166.

[73] Peter B. Canham, Richard F. Potter, and Dennis Woo. Geometric accommodation between the dimensions of erythrocytes and the calibre of heart and muscle capillaries in the rat. *The Journal of Physiology*, 347:697–712, 1984.

[74] T. Huppertz and A. L. Kelly. Physical chemistry of milk fat globules. In P. F. FOX and P. L. H. McSWEENEY, editors, *Advanced Dairy Chemistry, Volume 2: Lipids*, chapter 5, pages 173–212. Springer Science + Business Media, Inc., New York, 3rd edition, 2006.

[75] Lars Wiking, Jan Stagsted, Lennart Björck, and Jacob H. Nielsen. Milk fat globule size is affected by fat production in dairy cows. *International Dairy Journal*, 14(10):909–913, 2004. doi: 10.1016/j.idairyj.2004.03.005.

[76] Maciej Wojtkowski, Vivek J. Srinivasan, Tony H. Ko, James G. Fujimoto, Andrzej Kowalczyk, and Jay S. Duker. Ultrahigh-resolution, high-speed, Fourier domain optical coherence tomography and methods for dispersion compensation. *Optics Express*, 12(11):2404–2422, 2004. doi: 10.1364/OPEX.12.002404.

[77] Shuichi Makita, Youngjoo Hong, Masahiro Yamanari, Toyohiko Yatagai, and Yoshiaki Yasuno. Optical coherence angiography. *Optics Express*, 14(17): 7821–7840, 2006. doi: 10.1364/OE.14.007821.

[78] René M. Werkmeister, Nikolaus Dragostinoff, Stefan Palkovits, Reinhard Told, Agnes Boltz, Rainer A. Leitgeb, Martin Gröschl, Gerhard Garhöfer, and Leopold Schmetterer. Measurement of absolute blood flow velocity and blood flow in the human retina by dual-beam bidirectional Doppler Fourier-domain optical coherence tomography. *Investigative Ophthalmology and Visual Science*, 53(10):6062–6071, 2012. doi: 10.1167/iovs.12-9514.

[79] S. H. Yun, G. J. Tearney, J. F. de Boer, and B. E. Bouma. Motion artifacts in optical coherence tomography with frequency-domain ranging. *Optics Express*, 12(13):2977–2998, 2004. doi: 10.1364/OPEX.12.002977.

[80] Yingxia Li, Haiying Cheng, and Timothy Q. Duong. Blood-flow magnetic resonance imaging of the retina. *Neuroimage*, 39(4):1744–1751, 2008. doi: 10.1016/j.neuroimage.2007.10.030.

[81] Akitaka Tsujikawa, Junichi Kiryu, Atsushi Nonaka, Kenji Yamashiro, Yuichiro Ogura, and Yoshihito Honda. Reproducibility of scanning laser Doppler flowmetry in the rat retina and optic nervehead. *Japanese Journal of Ophthalmology*, 44(3):257–262, 2000. doi: 10.1016/S0021-5155(99)00226-9.

[82] C. Takagi, G. L. King, H. Takagi, Y. W. Lin, A. C. Clermont, and S. E. Bursell. Endothelin-1 action via endothelin receptors is a primary mechanism modulating retinal circulatory response to hyperoxia. *Investigative Ophthalmology and Visual Science*, 37(10):2099–2109, 1996.

[83] C. E. Riva, J. E. Grunwald, and S. H. Sinclair. Laser Doppler velocimetry study of the effect of pure oxygen breathing on retinal blood flow. *Investigative Ophthalmology and Visual Science*, 24(1):47–51, 1983.

[84] Barbara Kiss, Elzbieta Polska, Guido Dorner, Kaija Polak, Oliver Findl, Gabriele Fuchsjäger Mayrl, Hans-Georg Eichler, Michael Wolzt, and Leopold Schmetterer. Retinal blood flow during hyperoxia in humans revisited: Concerted results using different measurement techniques. *Microvascular Research*, 64(1):75–85, 2002. doi: 10.1006/mvre.2002.2402.

[85] A. Luksch, G. Garhöfer, A. Imhof, K. Polak, E. Polska, G. T. Dorner, S. Anzenhofer, M. Wolzt, and L. Schmetterer. Effect of inhalation of different mixtures of O_2 and CO_2 on retinal blood flow. *British Journal of Ophthalmology*, 86(10):1143–1147, 2002. doi: 10.1136/bjo.86.10.1143.

[86] Edward D. Gilmore, Chris Hudson, David Preiss, and Joe Fisher. Retinal arteriolar diameter, blood velocity, and blood flow response to an isocapnic hyperoxic provocation. *American Journal of Physiology - Heart and Circulatory Physiology*, 288(6):H2912–H2917, 2005. doi: 10.1152/ajpheart.01037.2004.

[87] M. Kisilevsky, C. Hudson, A. Mardimae, T. Wong, and J. Fisher. Concentration-dependent vasoconstrictive effect of hyperoxia on hypercarbia-dilated retinal arterioles. *Microvascular Research*, 75(2):263–268, 2008. doi: 10.1016/j.mvr.2007.07.007.

[88] René M. Werkmeister, Stefan Palkovits, Reinhard Told, Martin Gröschl, Rainer A. Leitgeb, Gerhard Garhöfer, and Leopold Schmetterer. Response of retinal blood flow to systemic hyperoxia as measured with dual-beam bidirectional Doppler Fourier-domain optical coherence tomography. *PLoS One*, 7(9):e45876, 2012. doi: 10.1371/journal.pone.0045876.

[89] Juan E. Grunwald and Sven-Erik Bursell. Hemodynamic changes as early markers of diabetic retinopathy. *Current Opinion in Endocrinology and Diabetes*, 3(4):298–306, 1996.

[90] L. Schmetterer and M. Wolzt. Ocular blood flow and associated functional deviations in diabetic retinopathy. *Diabetologia*, 42(4):387–405, 1999.

[91] Joanna Kur, Eric A. Newman, and Tailoi Chan-Ling. Cellular and physiological mechanisms underlying blood flow regulation in the retina and choroid in health and disease. *Progress in Retinal and Eye Research*, 31(5):377–406, 2012. doi: 10.1016/j.preteyeres.2012.04.004.

[92] Eric A. Newman. Functional hyperemia and mechanisms of neurovascular coupling in the retinal vasculature. *Journal of Cerebral Blood Flow & Metabolism*, 33(11):1685–1695, 2013. doi: 10.1038/jcbfm.2013.145.

[93] Charles E. Riva, Eric Logean, and Benedetto Falsini. Visually evoked hemodynamical response and assessment of neurovascular coupling in the optic nerve and retina. *Progress in Retinal and Eye Research*, 24(2):183–215, 2005. doi: 10.1016/j.preteyeres.2004.07.002.

[94] Anja I. Srienc, Zeb L. Kurth-Nelson, and Eric A. Newman. Imaging retinal blood flow with laser speckle flowmetry. *Frontiers in Neuroenergetics*, 2(128): 1–10, 2010. doi: 10.3389/fnene.2010.00128.

[95] Adrien Ponticorvo, Damon Cardenas, Andrew K. Dunn, Daniel Ts'o, and Timothy Q. Duong. Laser speckle contrast imaging of blood flow in rat retinas using an endoscope. *Journal of Biomedical Optics*, 18(9):090501, 2013. doi: 10.1117/1.JBO.18.9.090501.

[96] Yen-Yu I. Shih, Lin Wang, Bryan H. De La Garza, Guang Li, Grant Cull, Jeffery W. Kiel, and Timothy Q. Duong. Quantitative retinal and choroidal blood flow during light, dark adaptation and flicker light stimulation in rats using fluorescent microspheres. *Current Eye Research*, 38(2):292–298, 2013. doi: 10.3109/02713683.2012.756526.

[97] Anusha Mishra and Eric A. Newman. Aminoguanidine reverses the loss of functional hyperemia in a rat model of diabetic retinopathy. *Frontiers in Neuroenergetics*, 3(10):1–7, 2011. doi: 10.3389/fnene.2011.00010.

[98] Harsha Radhakrishnan and Vivek J. Srinivasan. Multiparametric optical coherence tomography imaging of the inner retinal hemodynamic response to visual stimulation. *Journal of Biomedical Optics*, 18(8):086010, 2013. doi: 10.1117/1.JBO.18.8.086010.

[99] G. Garhöfer, C. Zawinka, H. Resch, K. H. Huemer, G. T. Dorner, and L. Schmetterer. Diffuse luminance flicker increases blood flow in major retinal arteries and veins. *Vision Research*, 44(8):33–838, 2004. doi: 10.1016/j.visres.2003.11.013.

[100] Tess E. Kornfield and Eric A. Newman. Regulation of blood flow in the retinal trilaminar vascular network. *The Journal of Neuroscience*, 34(34): 11504–11513, 2014. doi: 10.1523/JNEUROSCI.1971-14.2014.

[101] Hirokazu Nishiwaki, Yuichiro Ogura, Hideya Kimura, Junichi Kiryu, Kazuaki Miyamoto, and Naoko Matsuda. Visualization and quantitative analysis of leukocyte dynamics in retinal microcirculation of rats. *Investigative Ophthalmology and Visual Science*, 37(7):1341–1347, 1996.

[102] Patrick S. Jensen and Matthew R. Glucksberg. Regional variation in capillary hemodynamics in the cat retina. *Investigative Ophthalmology and Visual Science*, 39(2):407–415, 1998.

[103] Ramin Tadayoni, Michel Paques, Alain Gaudric, and Eric Vicaut. Erythrocyte and leukocyte dynamics in the retinal capillaries of diabetic mice. *Experimental Eye Research*, 77:497–504, 2003. doi: 10.1016/S0014-4835(03)00155-6.

[104] Miyuki Unekawa, Minoru Tomita, Yutaka Tomita, Haruki Toriumi, Koichi Miyaki, and Norihiro Suzuki. RBC velocities in single capillaries of mouse and rat brains are the same, despite 10-fold difference in body size. *BRAIN RESEARCH*, 1320:6 9 – 7 3, 2010. doi: 10.1016/j.brainres.2010.01.032.

[105] Shigeta Arichika, Akihito Uji, Sotaro Ooto, Kazuaki Miyamoto, and Nagahisa Yoshimura. Adaptive optics-assisted identification of preferential erythrocyte aggregate pathways in the human retinal microvasculature. *PLOS ONE*, 9(2), 2014. doi: 10.1371/journal.pone.0089679.

[106] Stefan Zotter, Michael Pircher, Teresa Torzicky, Marco Bonesi, Erich Götzinger, Rainer A. Leitgeb, and Christoph K. Hitzenberger. Visualization of microvasculature by dual-beam phase-resolved Doppler optical coherence tomography. *Optics Express*, 19(2):1217–1227, 2011. doi: 10.1364/OE.19.001217.

[107] Ruikang K. Wang, Lin An, Peter Francis, and David J. Wilson. Depth-resolved imaging of capillary networks in retina and choroid using ultrahigh sensitive optical microangiography. *Optics Letters*, 35(9):1467–1469, 2010. doi: 10.1364/OL.35.001467.

[108] Shuichi Makita, Masahiro Yamanari, and Yoshiaki Yasuno. High-speed and high-sensitive optical coherence angiography. *Proceedings of SPIE*, 7372: 73721M–73721M–6, 2009. doi: 10.1117/12.831867.

[109] Shuichi Makita, Franck Jaillon, Masahiro Yamanari, Masahiro Miura, and Yoshiaki Yasuno. Comprehensive in vivo micro-vascular imaging of the human eye by dual-beam-scan Doppler optical coherence angiography. *Optics Express*, 19(2):1271–1283, 2011. doi: 10.1364/OE.19.001271.

[110] Erich Götzinger, Michael Pircher, and Christoph K. Hitzenberger. High speed spectral domain polarization sensitive optical coherence tomography of the human retina. *Optics Express*, 13(25):10217–10229, 2005. doi: 10.1364/OPEX.13.010217.

[111] Ireneusz Grulkowski, Iwona Gorczynska, Maciej Szkulmowski, Daniel Szlag, Anna Szkulmowska, Rainer A. Leitgeb, Andrzej Kowalczyk, and Maciej Wojtkowski. Scanning protocols dedicated to smart velocity ranging in spectral OCT. *Optics Express*, 17(26):23736–23754, 2009. doi: 10.1364/OE.17.023736.

[112] Tongcang Li, Simon Kheifets, David Medellin, and Mark G. Raizen. Measurement of the instantaneous velocity of a Brownian particle. *Science*, 328(5986): 1673–1675, 2010. doi: 10.1126/science.1189403.

[113] Simon Kheifets, Akarsh Simha, Kevin Melin, Tongcang Li, and Mark G. Raizen. Observation of Brownian motion in liquids at short times: Instantaneous velocity and memory loss. *Science*, 343(6178):1493–1496, 2014. doi: 10.1126/science.1248091.

[114] Haiying Cheng, Yumei Yan, and Timothy Q. Duong. Laser speckle imaging of rat retinal blood flow with hybrid temporal and spatial analysis method. *Proceedings of SPIE*, 7163:716304, 2009. doi: 10.1117/12.809906.

[115] Zhongwei Zhi, William Cepurna, Elaine Johnson, Hari Jayaram, John Morrison, and Ruikang K. Wang. Evaluation of the effect of elevated intraocular pressure and reduced ocular perfusion pressure on retinal capillary bed filling and total retinal blood flow in rats by OMAG/OCT. *Microvascular Research*, 101:86–95, 2015. doi: 10.1016/j.mvr.2015.07.001.

[116] Vivek J. Srinivasan, Harsha Radhakrishnan, Eng H. Lo, Emiri T. Mandeville, James Y. Jiang, Scott Barry, and Alex E. Cable. OCT methods for capillary velocimetry. *Biomedical Optics Express*, 3(3):612–629, 2012. doi: 10.1364/BOE.3.000612.

[117] Jonghwan Lee, Weicheng Wu, Frederic Lesage, and David A. Boas. Multiple-capillary measurement of RBC speed, flux, and density with optical coherence tomography. *Journal of Cerebral Blood Flow and Metabolism*, 33(11):1707–1710, 2013. doi: 10.1038/jcbfm.2013.158.

[118] Bernhard Baumann. *Spektrale Optische Kohärenztomographie bei 1310 nm*. Master thesis, 2006.

[119] Christophe Dorrer, Nadia Belabas, Jean-Pierre Likforman, and Manuel Joffre. Spectral resolution and sampling issues in Fourier-transform spectral interferometry. *Journal of the Optical Society of America B*, 17(10):1795–1802, 2000. doi: 10.1364/JOSAB.17.001795.

Martin Vietauer

Curriculum vitae

Beckmanngasse 32-34/2/13, 1140 Vienna, Austria
martin.vietauer@gmail.com
+43 (0)699 818 60 262

Personal data

Date of birth	**20 September, 1984**.
Place of birth	**Vienna, Austria**.
Citizenship	**Austrian**.

Education

09/2011 to date	**Doctoral Programme in Technical Sciences**, *Vienna University of Technology, Vienna, Austria*. Topic: Assessment of retinal perfusion in the rat via Fourier-domain optical coherence tomography and fundus imaging.
09/2004 – 06/2011	**Master Programme Technical Physics**, *Vienna University of Technology, Vienna, Austria*. Diploma thesis: Pour point measurements an thermal history of crude oils.
06/2003	**General qualification for university entrance, A-level equivalent**, *Realgymnasium Sacré Coeur Pressbaum, Pressbaum, Austria*.

Professional experience

09/2011 – 06/2015	**Scientific assistant**, *Medical University of Vienna, Vienna, Austria*. Development of a measurement method to assess large retinal vessels as well as the retinal microcirculation in the rat using Fourier-domain optical coherence tomography.
09/2010 – 02/2011	**Scientific assistant**, *OMV, Gänserndorf, Austria*. Investigation of the influence of thermal history on the pour point and the crystal structure of crude oils.
07/2008	**Intern**, *Stefan Meyer Institute for Subatomic Physics*.
09/2007	**Intern**, *Stefan Meyer Institute for Subatomic Physics*.

Publications and Conference Contributions

Papers in peer-reviewed journals

René M. Werkmeister, Aneesh Alex, Semira Kaya, Angelika Unterhuber, Bernd Hofer, Jasmin Riedl, Michael Bronhagl, Martin Vietauer, Doreen Schmidl, Tilman Schmoll, Gerhard Garhöfer, Wolfgang Drexler, Rainer A. Leitgeb, Martin Groeschl, and Leopold Schmetterer. Measurement of tear film thickness using ultrahigh-resolution optical coherence tomography. *Investigative Ophthalmology and Visual Science*, 54 (8):5578–5583, 2013. doi: doi:10.1167/iovs.13-11920.

René M. Werkmeister, Martin Vietauer, Corinna Knopf, Clemens Fürnsinn, Rainer A. Leitgeb, Herbert Reitsamer, Martin Gröschl, Gerhard Garhöfer, Walthard Vilser, and Leopold Schmetterer. Measurement of retinal blood flow in the rat by combining Doppler Fourier-domain optical coherence tomography with fundus imaging. *Journal of Biomedical Optics*, 19(10):106008, 2014. doi: 10.1117/1.JBO.19.10.106008.

Martin Vietauer, Corinna Knopf, Gerhard Garhöfer, Leopold Schmetterer, Martin Gröschl, and René M. Werkmeister. Measurement of the retinal microcirculation via single beam Doppler Fourier-domain optical coherence tomography using segmented B-scans. Manuscript in preparation, 2016.

Conference contributions

M. Vietauer, C. Knopf, L. Schmetterer, W. Vilser, and R. M. Werkmeister. Measurement of relative blood flow changes in retinal vessels of rodents using a Doppler FD-OCT system with integrated dynamic vessel analyzer, 2014. Poster at the ARVO 2014 Annual meeting.

M. Vietauer, C. Knopf, L. Schmetterer, W. Vilser, and R. M. Werkmeister. Measurement of relative blood flow changes in retinal vessels of rodents using a Doppler FD-OCT system with integrated dynamic vessel analyzer, 2014. Poster at the 10th YSA PhD Symposium.

Proceedings

Martin Vietauer, René M. Werkmeister, Corinna Knopf, Walthard Vilser, and Leopold Schmetterer. Measurement of relative blood flow changes in retinal vessels of rodents by a Doppler FD-OCT system with integrated dynamic vessel analyzer. *ARVO 2014 Annual Meeting Abstracts*, Session 420 (blood flow):4326, 2014. URL `http://www.arvo.org/webs/am2014/abstract/sessions/420.pdf`.